University of Cyprus

DEPARTMENT OF MECHANICAL AND MANUFACTURING ENGINEERING

Methods and algorithms for the quantification of blood flow in the microcirculation with contrast enhanced ultrasound

DOCTOR OF PHILOSOPHY DISSERTATION

DAMIANOS CHRISTOPHIDES

2015

University of Cyprus

DEPARTMENT OF MECHANICAL AND MANUFACTURING ENGINEERING

Methods and algorithms for the quantification of blood flow in the microcirculation with contrast enhanced ultrasound

DAMIANOS CHRISTOPHIDES

A Dissertation Submitted to the University of Cyprus in Partial Fulfillment of the Requirements for the Degree of Doctor of Philosophy

AUGUST 2015

VALIDATION PAGE

Doctoral Candidate: Damianos Christophides

Doctoral Thesis Title: Methods and algorithms for the quantification of blood flow in the microcirculation with contrast enhanced ultrasound

The present Doctoral Dissertation was submitted in partial fulfillment of the requirements for the Degree of Doctor of Philosophy at the ***Department of Mechanical and Manufacturing Engineering*** *and was approved on the 4th August 2015 by the members of the* ***Examination Committee.***

Examination Committee:

Research Supervisor:

Michalakis A. Averkiou, Associate Professor,
University of Cyprus, MME Department ----------

Committee Members:

Dan Adam, Professor,
Technion, Israel Institute of Technology ----------

Andreas Kyprianou, Assistant Professor,
University of Cyprus, MME Department ----------

Constantinos Pattichis, Professor,
University of Cyprus, CS Department ----------

Stavros Kassinos, Associate Professor,
University of Cyprus, MME Department ----------

DECLARATION OF DOCTORAL CANDIDATE

The present doctoral dissertation was submitted in partial fulfillment of the requirements for the degree of Doctor of Philosophy of the University of Cyprus. It is a product of original work of my own, unless otherwise mentioned through references, notes, or any other statements.

Damianos Christophides

……

Περίληψη

Η υπερηχογραφία με σκιαγραφικές ουσίες [Dynamic Contrast-Enhanced Ultrasound (DCEUS)] παρέχει σημαντικές δυνατότητες σαν κλινικό εργαλείο για την ανάλυση και ποσοτικοποίηση της αιμάτωσης των ιστών καθώς και για την κατανόηση της αγγειογέννεσης παθήσεων. Συγκεγκριμένα η πρόοδος νοσημάτων όπως κακοήθης ηπατικοί όγκοι, καρκινώματα στους νεφρούς και αθηρωματικές πλάκες στην καρωτίδα μπορεί να παρακολουθείται με την ποσοτικοποίηση του DCEUS. Ωστόσο η αξιόπιστη ποσοτικοποίηση με DCEUS έχει περιορισμούς όπως η εξάρτηση από τις ικανότητες του χειριστή, κορεσμό σήματος, φυσιολογική κίνηση και θόρυβο στίγματος. Σε αυτη την διδακτορική διατριβή παρουσιάζεται ένας καινότομος αλγόριθμος για την αυτόματη διόρθωση της αναπνευστικής κίνησης [Automatic Respiratory Gating (ARG)] ο οποίος ανταποκρίνεται στις δυσκολίες στην χρήση μοντέλων indicator dilution για την ποσοτικοποίησης της αιμάτωσης σε ιστούς με σημαντική ροή αίματος όπως ηπατικοί όγκοι. Σε αντίθεση οι αθηρωματικές πλάκες στην καρωτίδα έχουν ελάχιστη ροή αίματος κατά συνέπεια σχεδιάστηκε μέθοδος για την ποσοτικοποίηση του ποσοστού έκτασης της αιμάτωσης της πλάκας δεδομένου ότι τα μοντέλα indicator dilution δεν ισχύουν.

Ο καινοτόμος αλγόριθμός ARG ξεπερνά αρκετά μειονεκτήματα αλγόριθμων διόρθωσης αναπνευστικής κίνησης που υπάρχουν στην βιβλιογραφία επιδεικνύοντας την ικανότητα να αφαιρεί την κίνηση εντός και εκτός του απεικονιστικού επιπέδου, υψηλή υπολογιστική απόδοση διορθώνοντας μία 2 λεπτών διάρκειας απεικόνιση σε λιγότερο από 10 δευτερόλεπτα και ευκολία στην χρήση. Η αύξηση στην αξιοπιστία με την χρήση του ARG σε όγκους του ήπατος αποδεικνύεται με την χρήση κλινικών δεδομένων με μία σημαντική αύξηση στην ποιότητα προσαρμογής του μοντέλου στα δεδομένα ($p<0.05$).

Ένα μοντέλο εξομοίωσης της αναπνευστικής κίνησης αναπτύσσεται για την διερεύνηση της ικανότητας του αλγόριθμου ARG στην μείωση του ποσοστιαίου σφάλματος των παραμέτρων ποσοτικοποίησης από τις πραγματικές τους τιμές. Το μοντέλο αποδεικνύει ότι η χρήση του ARG μπορεί να μειώσει το μέγιστο σφάλμα στις παραμέτρους από 32.3% σε 6.2%. Επίσης διερευνώνται οι επιπτώσεις στην ποσοτικοποίηση με την παρουσία πολλαπλασιαστικού θορύβου.

Ένας αλγόριθμός αναπτύσσεται για τον υπολογισμό του ποσοστού έκτασης της αιμάτωσης των αθηρωματικών πλακών στην καρωτίδα με την χρήση DCEUS. Η ποιοτική βαθμονόμηση της αιμάτωσης των αθηρωματικών πλακών χρησιμοποιείτε για την επικύρωση της ποσοτικοποίησης. Η ποιοτική όπως και η ποσοτική βαθμονόμηση της αιμάτωσης των αθηρωματικών πλακών αποδεικνύουν ότι η έκταση της αιμάτωσης στις πλάκες σε συμπτωματικούς ασθενείς είναι σημαντικά μειωμένη σε σχέση με τους ασυμπτωματικούς ($p<0.05$). Το ποσοστό έκτασης της αιμάτωσης της πλάκας παρέχει την δυνατότητα της ταυτοποίησης των χαρακτηριστικών ευάλωτων πλακών όπως επίσης και αλλαγές στην μικροροή με την χρήση αντιαθηρωματικών θεραπειών.

Abstract

Dynamic contrast enhanced ultrasound (DCEUS) holds great promise as a clinical tool for the analysis and quantification of tissue perfusion and it can provide valuable insight into the development of disease neovascularization. Specifically the progress of diseases such as malignant liver lesions, renal carcinomas and carotid atherosclerotic plaques can be monitored using quantitative DCEUS. However the reliable implementation of quantitative DCEUS has several limitations like operator dependence, signal saturation, physiological motion and speckle noise. In this thesis a novel automatic respiratory gating (ARG) algorithm is developed to address challenges in the use of indicator dilution models for the quantification of tissue perfusion that exhibits a high amount of blood flow such as liver lesions. Contrary carotid plaques exhibit very low blood flows and a method is formulated to calculate the percent perfusion coverage of the plaque's area given than indicator dilution models are not applicable.

The novel ARG developed overcomes many of the limitations of respiratory compensation methods published in the literature demonstrating efficiency in removing in-plane as well as out-of-plane motion, high computational speed by processing a 2 minute DCEUS acquisition in less than 10 seconds and ease of implementation. The increase in the reliability of liver lesion DCEUS quantification with the use of ARG is demonstrated using clinical data with a significant increase in the quality-of-fit of perfusion modeling ($p<0.05$).

A respiratory motion simulation model (RMSM) is constructed to investigate the efficiency of ARG in reducing the percentage error of DCEUS quantification parameters from their true values. The RMSM demonstrates a decrease in the maximum percentage error of DCEUS quantification parameters from 32.3% to 6.2% with the use of ARG. The implications of the presence of multiplicative noise in liver lesion DCEUS acquisitions are also studied and quantified using the RMSM.

An algorithm is developed for the calculation of the percent perfusion coverage of carotid atherosclerotic plaques from DCEUS acquisitions. Visual scores of carotid plaque perfusion are used to validate the results from the DCEUS quantification analysis. Both the percent perfused area with DCEUS quantification analysis and the qualitative scores demonstrate that the extent of carotid plaque perfusion for symptomatic patients is significantly less than asymptomatic ($p<0.05$). Percent perfusion coverage has the potential to identify the perfusion characteristics of vulnerable carotid plaques and to also assess changes in the microflow caused by anti-atherosclerotic therapies.

Acknowledgements

I would like to thank my PhD supervisor Prof. Mike Averkiou for inspiring me to pursuit a career in research. After 4 years of working close to him I am now certain of the direction that I want to take, following many years of uncertainty. In many cases he believed more in my work than I did. It was amazing to experience his unrelenting excitement in research even after all these years in the field; I would like to think that some of his persistence has rubbed onto me.

Many special thanks to Dr. Christina Keravnou for all her support in the everyday challenges that came up along the years. I was always amazed by Christina's tenacity, abilities, maturity and scientific versatility. I find it impossible to imagine something coming between Christina and her goals. I will always have happy memories from the time we worked together.

Dr. Maria-Louisa Izamis is an extraordinary person and scientist that we were fortunate enough to have in our laboratory. I have never met a person like her before; she was always calm and able to find rational arguments to dismiss irrational fears and doubts that can come in the mind of any PhD student. I will always be grateful for her help.

Dr. Christophoros Mannaris was finishing his PhD when I joined the research team and he was always there to encourage me on the road ahead in my PhD while at the same time making sure I don't forget all the things that I had already accomplished. Mr. Kypros Stylianou was a great help for all of us and was able to make every newcomer to the laboratory feel welcome. His abilities as a laboratory instructor are phenomenal since he was able to even teach me to acquire some decent water tank beam patterns.

Contents

List of Figures

List of Tables

1
Introduction

Medical imaging harnesses the knowledge of physical phenomena like ultrasound, X-rays, radioactivity and magnetic resonance to provide clinicians with effective diagnostic tools. Information can be provided into the function, pathology and structure of the human body helping with the timely diagnosis of disease. The data provided by any medical imaging modality needs to be readily accessible and accurate to maximize its diagnostic potential. Algorithms and tools have been developed to quantify, enhance, segment and visualize medical imaging data to facilitate reliable, reproducible and accurate diagnosis. This thesis focuses on providing such algorithms and methods in order to maximize the diagnostic potential of quantitative functional contrast-enhanced ultrasound.

1.1 Dynamic contrast enhanced ultrasound (DCEUS)

Ultrasound is a non-invasive, relatively inexpensive, portable imaging modality with no adverse ionizing radiation effects. The publication of The Theory of Sound by Lord Rayleigh in 1877[1] and the discovery of piezoelectric materials by Pierre Curie in 1880[2] were crucial in the development of medical and industrial ultrasound. Developments in methods and materials resulted in the first use of medical diagnostic ultrasound in 1942 by Karl and Friedrich Dussik in Austria[3] for the detection of brain tumor location.

The use of ultrasound imaging in medicine for the study of anatomical features is based on the pulse-echo principle. Ultrasound pulses are transmitted using the piezoelectric elements of an ultrasound probe and the echoes reflected from tissue are detected. The time delay between transmission-reception of the echoes and the speed of sound in tissue is used to determine the location from which a specific echo has originated. In addition the amplitude of the detected echo will determine the grey-scale level of the resulting ultrasound image. By transmitting multiple pulses along different piezoelectric elements of the ultrasound probe a B- mode or tissue ultrasound image of the patient's anatomy can be constructed (Figure 1-1).

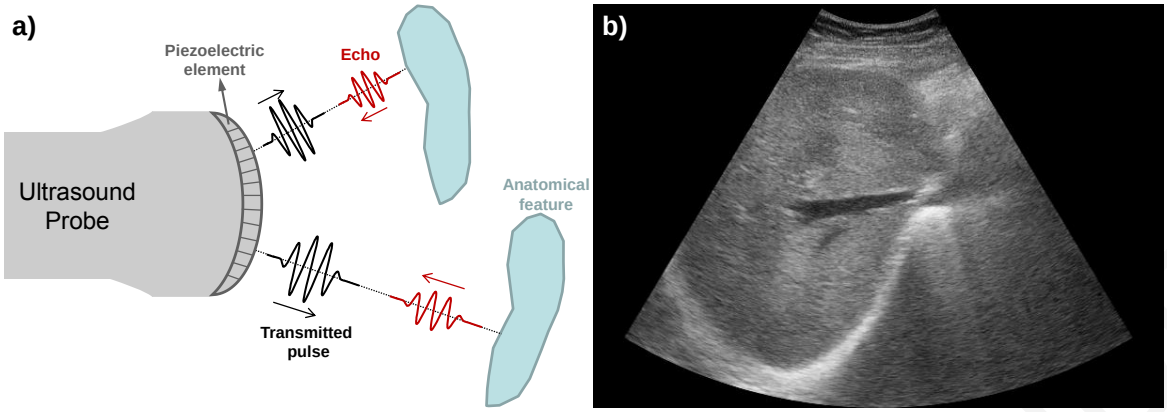

Figure 1-1: a) Demonstration of the pulse-echo principle used in ultrasound imaging. Pulses are transmitted from the ultrasound probe and echoes are reflected from the patient's anatomical features. The time delay between the echoes along with their amplitudes is used to construct an image of the patient's anatomy. b) Example of an ultrasound tissue image of the liver.

The medical use of diagnostic ultrasound has been enhanced with the development of contrast agents that allow for the visualization of tissue perfusion[4]. Ultrasound contrast agents are microbubbles usually consisting of a phospholipid shell encompassing an inert gas like sulfur hexafluoride (SF_6). Microbubbles have the similar size as red blood cells (1-10μm) and do not leak into the interstitial space making them a pure blood-pool contrast agent and thus suitable for the study of tissue perfusion. The microbubbles are introduced into the blood stream intravenously either as a bolus or a constant infusion[5], [6].

Microbubbles produce non-linear echoes when they interact with ultrasound pulses. These non-linear echoes contain harmonic components of the pulse's fundamental frequency (f_o). With the use of pulsing schemes like pulse inversion (PI), power modulation (PM) or their combinations[7], [8] the echoes originating from microbubbles can be differentiated from the echoes received from tissue (Figure 1-2). The correct implementation of these pulsing schemes is crucial in ensuring that image intensity corresponds to the quantity of microbubbles present in the vasculature.

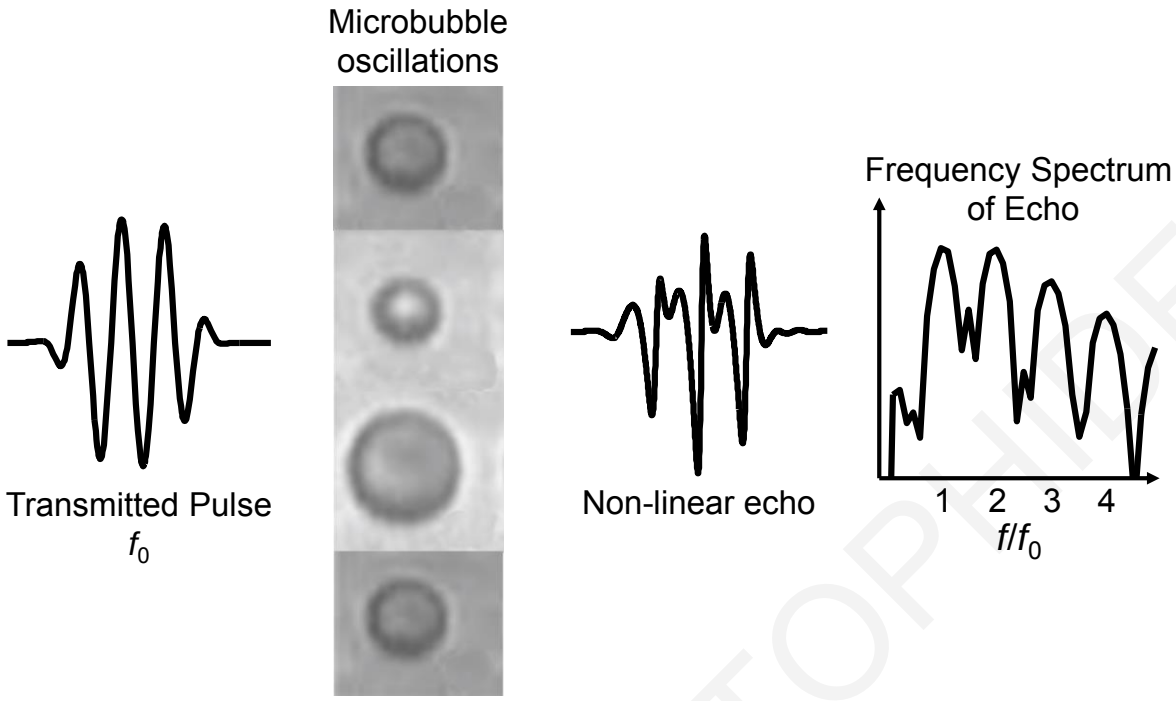

Figure 1-2: Illustration of non-linear echoes produced by a microbubble oscillating[9] under the pressure induced by a transmitted ultrasound pulse[10]. The harmonic components of the resulting non-linear echo ($2f_o$, $3f_o$, …) can be differentiated from echoes originating from tissue using PI or PM pulsing schemes.

The clinical use of microbubbles as an ultrasound contrast agent allows for real-time imaging of tissue perfusion. Dynamic contrast enhanced ultrasound (DCEUS) has been used widely in radiology for the study of the response to treatment of liver metastases[11], the evaluation of focal nodular hyperplasia in the liver[12], the visualization of atherosclerotic plaque neovascularization[13] and the evaluation of response to treatment of metastatic renal cell carcinoma[14].

DCEUS enables a clinician to diagnose a medical condition by visual evaluation of a frame (image) or a loop (series of images) of the flow of microbubbles in tissue and vessels. Such a diagnosis can be performed by injecting the microbubbles as a single bolus intravenously and then observe the perfusion patterns in the large vessels and the microcirculation. The DCEUS images are often displayed side-by-side with tissue ultrasound images in dual-contrast imaging mode in order to provide for simultaneous anatomical and functional imaging.

Specifically DCEUS can be used to visualize the different phases of liver perfusion. Using a bolus injection the microbubbles can be seen entering the liver parenchyma through the hepatic artery in the first 15-30 seconds (arterial phase) followed by microbubbles flowing into the liver from the hepatic portal vein in the subsequent 30-120 seconds (portal venous phase). The ultrasound contrast agent is then washed-out from the normal liver parenchyma via the hepatic vein. Lesions can be differentiated as malignant or

benign by comparing their wash-in and wash-out times compared to the normal liver parenchyma. For example benign focal nodular hyperplasia (FNH) lesions exhibit early enhancement during the arterial phase that is sustained through the portal venous phase in contrast with some malignant lesions that appear as hypoechoic during the portal venous phase[15] (Figure 1-3) .

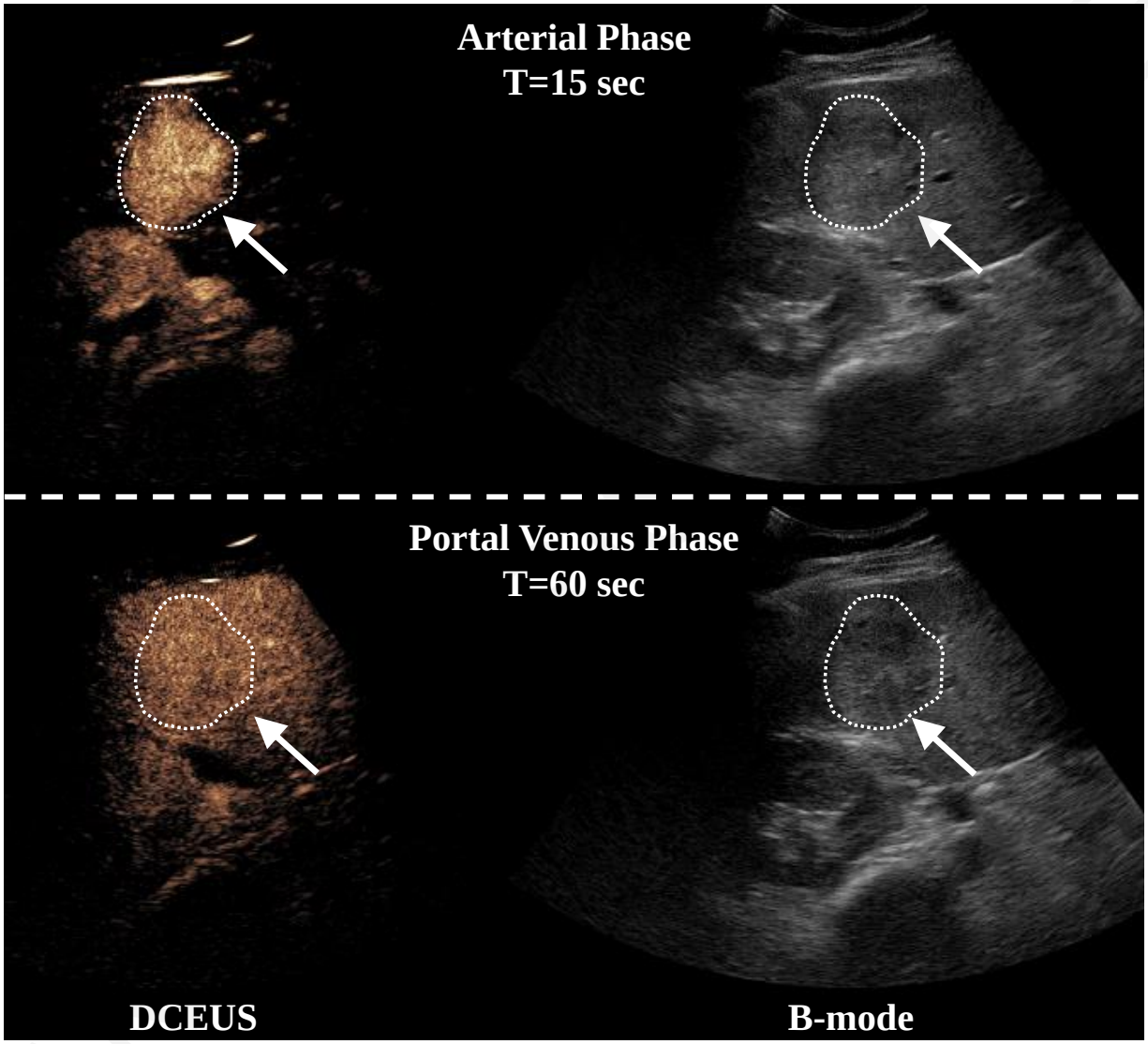

Figure 1-3: A liver lesion is shown both in contrast mode (left) and B-mode (right) at different times (T) from the arrival time of the microbubbles in the liver. In the early arterial phase (T=15 sec) the lesion (dotted white line) can be clearly seen in DCEUS mode (white arrow) whereas in the portal venous phase (T=60 sec) the lesion cannot be seen since it exhibits identical wash-out kinetics as the surrounding normal liver tissue. Thus, by detecting perfusion in the microcirculation and the overall vascular patterns a suspected lesion can be diagnosed as a benign FNH.

Qualitative evaluation of DCEUS can be a valuable clinical tool in the hands of a trained clinician. Nevertheless a quantitative approach to DCEUS can have a number of advantages. It provides the operator with metrics that can aid with the diagnosis and offers functional information that would otherwise not be accessible via visual examination.

Subtle changes in the microvasculature that would be difficult to detect using qualitative DCEUS can be identified as relative or absolute changes in quantitative DCEUS metrics. This can be particularly useful in monitoring changes in the perfusion of disease at different stages of treatment. Mathematical methods and algorithms can be used in quantitative DCEUS that give metrics relating to physical quantities like blood flow rate[16] or extend of neovascularization[17].

A widely used method of DCEUS quantification is the segmentation of a structure using a region of interest (ROI) and extraction of the mean linear DCEUS intensity within the ROI as a function of time to form a time-intensity curve (TIC) [5], [6], [11], [18]. A mathematical model can be fitted on the TIC and useful information can be extracted regarding the hemodynamics within the ROI.

Indicator dilution models in quantitative DCEUS are used in order to extract quantification parameters that can be a relative measure of flow rate like the rise time (RT), mean transit time (MTT) and area under the curve (AUC)[16], [19]. The vascular volume contained in the ROI can also be related to the peak intensity (PI) derived for the mathematical model (Figure 1-4). Empirical quantification parameters like the wash-in time (WIT) (time it takes for the intensity to go from 5% of the PI to 95%) have also been used in the literature[11]. In addition to the physical assumptions[16] made in the clinical use of indicator dilution models it is also crucial that the time intensity curve is representative of the hemodynamics of the tissue under investigation. Therefore it is imperative to remove any artefacts or sources of uncertainty from the time intensity curve before the indicator dilution model is fitted on the data.

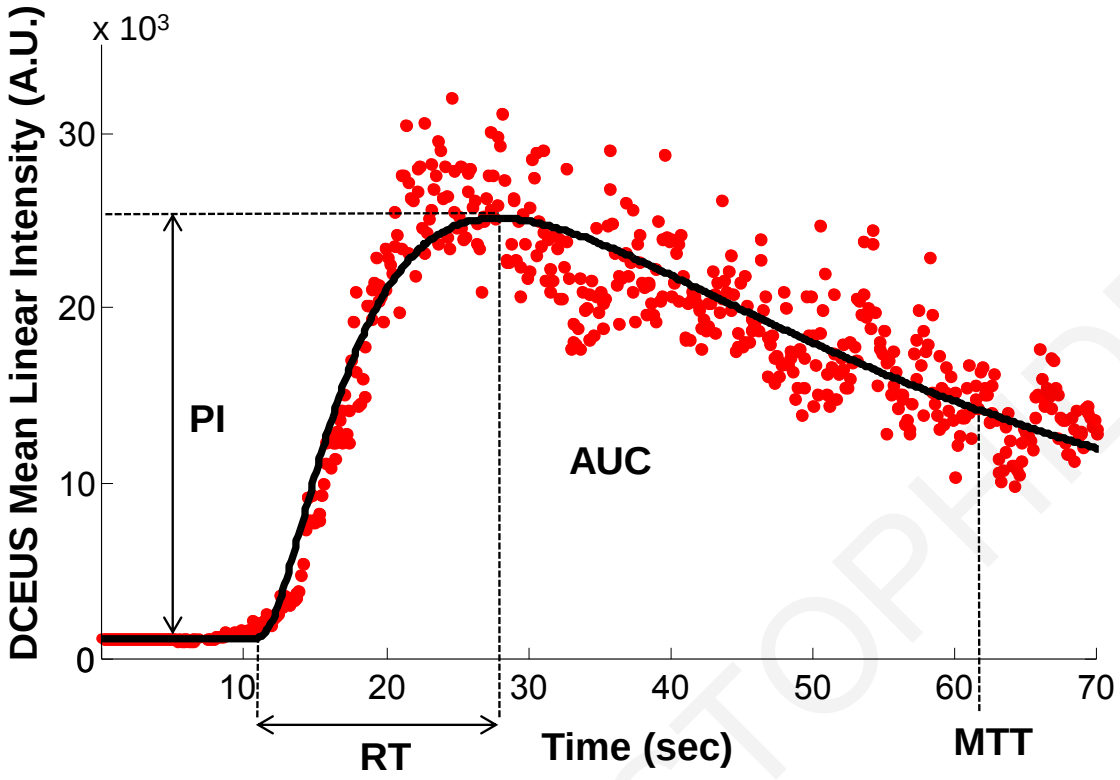

Figure 1-4: Bolus kinetics curve showing wash-in and washout of the contrast microbubbles. The lognormal indicator dilution model[16] (solid line) is fitted on DCEUS mean linear intensity data (dots). The DCEUS quantification parameters of RT, MTT, PI and AUC are indicated on the curve and can be extracted from the lognormal model.

1.2 Quantitative DCEUS of liver lesions and respiratory motion

Numerous studies have used quantitative DCEUS in order to assess the response of malignant liver lesions to treatment[11], [20], [21]. In a study by Averkiou et al.[11] quantitative DCEUS was used to predict the response of patients undergoing a combination of antiangiogenic and cytotoxic treatments. By taking the ratio of the WIT of the liver lesions to the WIT of the normal liver parenchyma four out of five patients that had a response were identified during the first week of treatment. A 2011 study[21] of 42 patients treated with Bevacizumab (Avastin; F. Hoffmann-La Roche, Basel, Switzerland) for hepatocellular carcinoma (HCC) found that the lesion's AUC and WIT correlated with response to treatment. Zocco et al.[20] also found that AUC and RT to be significantly associated with longer survival of HCC patients taking Sorafenib (Nexavar; Bayer Pharma AG, Berlin, Germany).

Even though these studies have shown promise in monitoring treatment response there are limitations that compromise the sensitivity, reliability and reproducibility of liver lesion DCEUS. One of the most important limitations is operator dependence. Sufficient resources must be invested in training competent ultrasound operators so that they can

acquire consistent and reliable DCEUS loops. Other common issues encountered in liver lesion DCEUS are acoustic shadowing, signal saturation[22] and stability of ultrasound probe placement. Tools like surgical-type articulated arms can be used to avoid operator hand motion during acquisitions[11]. Although care can be taken by a trained operator to limit factors of uncertainty other problems like non-linear propagation of ultrasound[23] and beam non-uniformity are inherent to DCEUS acquisitions.

Respiratory motion is another important limitation of liver lesion DCEUS quantification. As the patient breaths the diaphragm pushes against the liver causing the anatomy being imaged to change in relation to the fixed imaging plane. The patient's respiratory motion can potentially introduce artefacts of a lesion's time intensity curve and affect the results of quantitative DCEUS. Various solutions have been proposed in the literature for correcting the effects of respiratory motion in liver lesion DCEUS.

A method used mainly for qualitative studies is for the patients to hold their breath but this technique has very limited application to quantitative DCEUS acquisitions that can last up to three minutes[6]. Liver lesion DCEUS quantification can also be performed by instructing the patients to breath slowly in order to minimize respiratory motion artefacts[24]. Although these methods can potentially reduce the effects of respiration on liver lesion DCEUS acquisitions they rely on the patient's collaboration and cannot be used reliably across multiple monitoring sessions. In addition, breath holding may influence the hemodynamics and alter the physical parameter being measured[25], i.e., blood flow in the microcirculation.

Post-processing techniques have also been used on free-breathing liver lesion DCEUS acquisitions. In a study of dual-contrast acquisitions by Averkiou et al.[11] a reference position of the diaphragm was identified on the tissue images and frames of the DCEUS loop in which the diaphragm deviated from the reference position were manually rejected. Despite this method being able to remove respiratory motion without relying on the patient's cooperation it is time consuming and it relies on the operator in identifying the diaphragm. Grouls et al.[26] implemented a semi-automated approach of the method introduced by Averkiou et al. and showed that it can improve accuracy of functional and molecular liver imaging.

Automated respiratory correction techniques have also been published in the literature[27]–[30]. Renault et al.[28] used independent component analysis (ICA) to extract the respiratory kinetics curve from liver lesion DCEUS acquisitions. The ICA method proposed relied on the user to manually select the respiratory kinetics curve from

the first three principal components derived. A threshold would then been applied on the peaks and troughs of the respiratory kinetics curve to extract the end phases of the respiratory cycle. The method suffered from the varying amplitude of the respiratory kinetics curve due to the wash-in and wash-out affecting the intensity of the DCEUS signal during the acquisition. Mulé et al.[27] expanded on the ICA method proposed by Renault et al. using principal component analysis (PCA) to automatically select the respiratory kinetics curve based on the prior knowledge that the respiratory frequency range is between 0.1 and 0.5Hz. In addition to the automatic selection of the respiratory kinetics curve the tissue imaging mode was used in order to avoid changes in the intensity signal of the respiratory kinetics curve due to the uptake of contrast agent. The method proposed by Mulé et al. would allow for 100 frames to be processed between 6-8 seconds on a PC with a 3GHz CPU and 2GB of RAM. The major drawback of the proposed method is that it allows for the extraction of only the end phases of the breathing cycle and since the acquisition is two dimensional there is no certainty what part, if any, of the lesion will be present on the imaging plane (Figure 1-5).

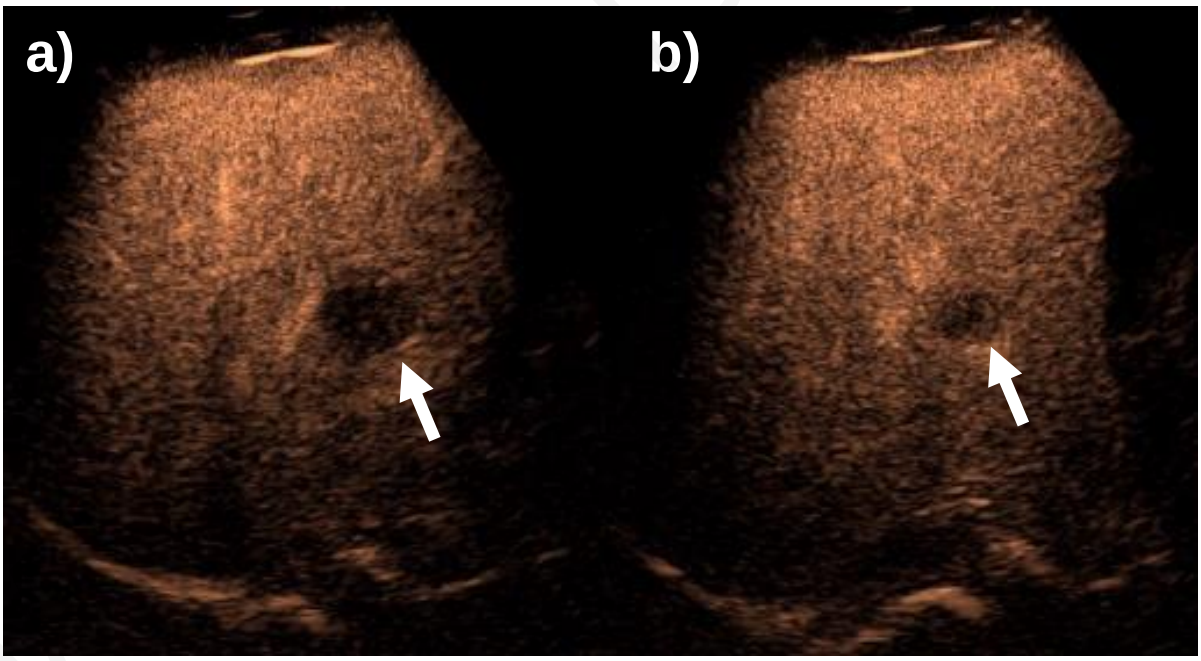

Figure 1-5: Examples of liver DCEUS images showing a metastatic lesion (white arrow) at two different breathing cycle phases with a) maximum and b) minimum presence of the lesion on the imaging plane.

Image registration techniques have also been utilized to enable respiratory motion compensation in quantitative liver lesion DCEUS[29]–[31]. Rognin et al.[29], [31] used the mutual information criterion to align frames onto a reference frame for parametric imaging of liver lesion DCEUS acquisitions. The registration process allowed for 2D translation and rotation in order to maximize the mutual information criterion and align the

frames. Zhang et al.[30] used the sum of absolute differences criterion to perform rigid registration with only 2D translation to correct for respiratory motion in liver lesion DCEUS. Both studies reported a significant mean increase in the quality of fit of parametric imaging perfusion modeling of 11%[29] and 15%[30]. The image registration techniques proposed require user intervention in order to delineate one or more ROI on the image to define the search space for the image registration. Furthermore the image registration technique proposed by Rognin et al. does not offer a scheme for rejecting frames with significant out-of-plane motion in contrast with the algorithm proposed by Zhang et al. However the method proposed by Zhang et al. is time consuming as it can take up to 30 minutes to process a 2 minute liver lesion DCEUS acquisition at a frame rate of 8 Hz; a computational time that is unacceptable for routine clinical use.

1.3 DCEUS of carotid atherosclerotic plaques

The role of carotid arteries is to supply the head and neck with oxygenated blood. The carotid arteries themselves get oxygenated through a network of smaller blood vessels known as the vasa vasorum. Pathological development of the vasa vasorum from the outer layers into the inner layers of the vessel wall has been a consistent feature of carotid atherosclerotic plaques[32]. Histological studies have been conducted that showed a correlation between increased presence of neovascularization within plaques and risk of rupture. Moreno et al.[33] analyzed 269 plaques and demonstrated a higher density of microvessels in ruptured plaques compared to non-ruptured. In a comparative study[34] between plaques from symptomatic patients and asymptomatic patients a significantly higher number of microvessels were found in the symptomatic group.

B-mode ultrasound is a long established imaging modality in the classification of carotid plaque vulnerability. The most widely accepted categories are presented in increasing order of plaque instability: i) uniformly echolucent, ii) predominantly echolucent, iii) predominantly echogenic and iv) uniformly echogenic[35], [10]. While the information provided from B-mode is restricted to anatomical features with the use of DCEUS it is possible to provide real-time functional imaging of the perfusion of the microvasculature of carotid plaques by detecting blood flow even at very low velocities (< 1cm/sec). Therefore DCEUS has the potential to be used as a tool to quantify the extent of perfusion in the plaques and consequently evaluate the risk of carotid plaque patients in presenting with symptoms. In a qualitative study of 293 atherosclerotic plaques by Staub et al.[36] significant correlation was found between DCEUS signal enhancement and plaque

echolucency in tissue imaging mode. Coli et al.[37] showed that a qualitative increase in DCEUS signal intensity is correlated both with histological density of microvessels and B-mode plaque echolucency.

The change in the intensity values due to the uptake of microbubbles can be an additional challenge in the qualitative assessment of DCEUS loops compared to B-mode imaging. Thus a quantitative approach would be of significant benefit to carotid plaque DCEUS as it would allow for the extraction of easily accessible and useful clinical information. In addition the low signal intensity within the plaque compared with the high signal from the arterial lumen can be difficult to visualize (Figure 1-6). Other sources of uncertainty like motion artefacts from probe movement, plaque movement due to the pulsating blood pressure and pseudo-enhancement in the far wall of the carotid artery[23] need to be taken into account in any reliable qualitative DCEUS analysis.

A limited number of studies[17], [38], [39] have proposed quantitative DCEUS methods in an attempt to address the limitations of qualitative DCEUS evaluation of carotid atherosclerotic plaques. In a study by Xiong et al.[39] the gamma variate indicator dilution model was fitted onto time intensity curves extracted from carotid plaques and the arterial lumen. The PI of the plaque, and the ratio of the PI between the plaque and the lumen were shown to be significantly higher in symptomatic patients than in asymptomatic patients. Hoogi et al.[17] used image segmentation to detect the percentage of neovascularization within the carotid plaque. The study found significant correlation between the percentage area of neovascularization of carotid plaques measured with histology and DCEUS. Adaptive image thresholding was used by Akkus et al.[38] to detect neovascularization within carotid atherosclerotic plaques and compared the results of the quantitative analysis with qualitative visual scores. Significant correlation was demonstrated between the absolute and percentage areas of plaque perfusion with visual scores of DCEUS signal enhancement.

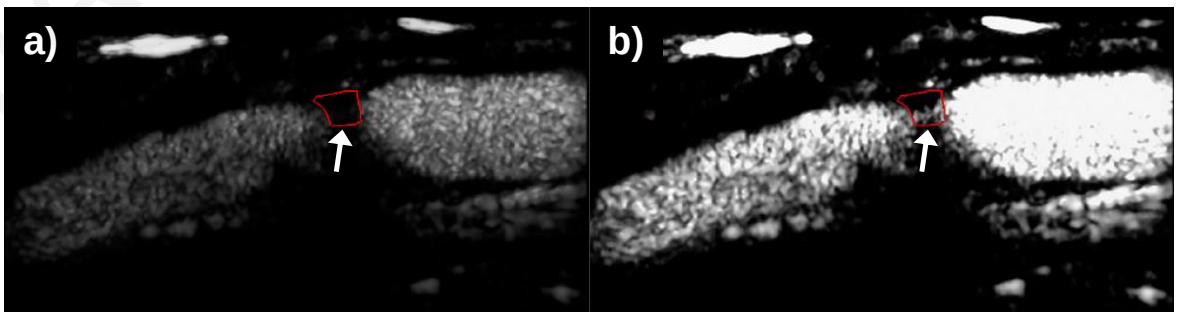

Figure 1-6: Example of an image from a DCEUS loop of a carotid atherosclerotic plaque (red line). With a) using the default image contrast and brightness the plaque appears to contain no microbubbles while with b) the upper level of the image contrast is reduced to enhance the visualization of low intensity values showing the plaque to be perfused proximal to the lumen (white arrow).

Even though the quantitative DCEUS studies of carotid plaque neovascularization have demonstrated potential by showing a significant correlation with either symptoms[39], histology[17] or visual scores[38] there are limitations to the methods proposed. Although indicator dilution models like the gamma variate model used by Xiong et al. have been applied effectively in the assessment of myocardial blood flow[40] they may not be applicable to the slower flow rates within the microvasculature of carotid plaques. In addition Akkus et al. applied the method proposed by Xiong et al. and found that the gamma variate model failed to produce a valid fit for 20% of the plaque time intensity curves examined. Despite that both of the methods proposed by Akkus et al. and Hoogi et al. quantify the area of neovascularization within the carotid plaque the two studies report notably different results. Hoogi et al. analyzed plaques from 22 patients and found the percentage of plaque neovascularization to vary approximately between 0 and 20% whereas Akkus et al. reported significantly higher percentages with a mean of 32.69%. However there are differences in the characteristics of the patient populations examined by the two studies with 68% of the patients studied by Hoogi et al. being asymptomatic while Akkus et al. considered only patients with symptomatic stenosis.

1.4 Scope of this thesis

The scope of this thesis is to develop, test and clinically validate methods and algorithms for the quantification of perfusion in the microcirculation. In particular the thesis aims in significantly reducing the detrimental effect of respiratory motion on the accuracy and reliability of liver lesion DCEUS quantification. A novel algorithm for automatic respiratory gating (ARG) is developed that aims to address the limitations of other algorithms presented in the literature. The efficiency of the ARG algorithm in significantly removing respiratory motion artefacts and increasing the accuracy of liver lesion DCEUS is validated using clinical data and a simulation model. In addition the differences in the perfusion characteristics of carotid plaques between symptomatic and asymptomatic patients are investigated. A new method for quantifying the percentage perfusion coverage of carotid plaques is developed and verified against qualitative visual scores of clinical acquisitions.

In Chapter 2 a novel ARG algorithm is developed that aims to overcome the limitations of the methods presented in the literature in terms of computational speed, efficiency and ease of use. The ARG algorithm is implemented on the tissue side of dual contrast imaging acquisitions. Moving structures in the loops are detected using frame

subtraction from the average of all the frames in the loop. Furthermore the nature of the detected motion is characterized according to its respiratory contents using frequency domain analysis. The respiratory kinetics curve of the dual contrast imaging acquisition is extracted by calculating the time intensity curve of the moving structure with the highest content of respiratory motion. The technical characteristics of the ARG algorithm are compared with other respiratory motion compensation methods found in the literature. Also the efficiency of the ARG algorithm in removing respiratory motion is evaluated by considering the improvement in the quality of fit of the lognormal indicator dilution model[16] onto liver lesion time intensity curves.

Chapter 3 which presents a clinical validation of the developed ARG algorithm, explores in depth the clinical impact of the ARG algorithm on the accuracy of liver lesion DCEUS quantification. The effect of respiration on the time intensity curve of each liver lesion examined is quantified using the respiration amplitude (*RA*) metric. The influence of the ARG algorithm on the quantification parameters of RT, MTT, PI and AUC is analyzed for different ranges of *RA*. Furthermore the correlation between the quality of fit of the lognormal model on liver lesion time intensity curves (R^2_{LN}) and the *RA* is investigated with and without the use of ARG.

In Chapter 4 a respiratory motion simulation model (RMSM) is developed to address the intrinsic limitation of assessing the absolute accuracy of liver lesion DCEUS. The RMSM is constructed using perfusion models and respiratory kinetics derived from clinical acquisitions. Specifically the liver lesion is modeled as a sphere moving under the effect of respiration inside of a cubic liver parenchyma. Using the RMSM the true liver lesion quantification parameters can be compared with those calculated under the influence of respiratory motion. The decrease of the percentage error with the use of ARG is assessed for the RT, MTT, PI and AUC. In addition the clinical relevance of the RMSM is verified by comparing the relationship of the R^2_{LN} and *RA* extracted from the RMSM and clinical data.

A method for quantifying the percentage area of perfusion in carotid atherosclerotic plaques is presented in Chapter 5. Statistics, image and signal processing are used to design an algorithm for the detection of the low intensity DCEUS signal within the plaques. The ratio of the perfused area within the carotid plaque and the total area of the carotid plaque is calculated as the percent perfusion coverage of the plaque. The use of the plaque percent perfusion coverage as a biomarker of atherosclerosis and plaque vulnerability is investigated by comparing the differences in the perfusion of plaques between

symptomatic and asymptomatic patients. In addition to the quantitative analysis the perfusion of the carotid plaques is graded based on a qualitative scale. The results will be compared with other studies in the literature. The work presented in Chapter 5 contributes to the limited number of studies on carotid plaque DCEUS quantification.

Chapter 6 presents a conclusive discussion on the overall impact of this thesis in the development of quantification methods, algorithms and tools for the improvement of liver lesion and carotid plaque DCEUS quantification.

References

[1] L. Rayleigh, *Theory of Sound.* London: Macmillan, 1877.

[2] J. Curie and P. Curie, "Development, via compression, of electric polarization in hemihedral crystals with inclined faces," *Bull. la Soc. Minerol. Fr.*, vol. 3, pp. 90–93, 1880.

[3] P. Suetens, *Fundamentals of medical imaging*, Second. Cambridge, UK; New York: Cambridge University Press, 2009.

[4] P. N. Burns, "Harmonic imaging with ultrasound contrast agents.," *Clin. Radiol.*, vol. 51 Suppl 1, pp. 50–55, 1996.

[5] E. Leen, M. Averkiou, M. Arditi, P. Burns, D. Bokor, T. Gauthier, Y. Kono, and O. Lucidarme, "Dynamic contrast enhanced ultrasound assessment of the vascular effects of novel therapeutics in early stage trials," *Eur. Radiol.*, vol. 22, no. 7, pp. 1442–1450, 2012.

[6] C. F. Dietrich, M. A. Averkiou, J. M. Correas, N. Lassau, E. Leen, and F. Piscaglia, "An EFSUMB introduction into dynamic contrast-enhanced ultrasound (DCE-US) for quantification of tumour perfusion," *Ultraschall der Medizin*, vol. 33, no. 4, pp. 344–351, 2012.

[7] M. Averkiou, M. Bruce, S. Jensen, P. Rafter, T. Brock-Fishe, and J. Powers, "Pulsing schemes for the detection of nonlinear echoes from contrast microbubbles," in *9th European Symposium on Ultrasound Contrast Imaging*, 2004, pp. 17–24.

[8] M. Averkiou, M. Bruce, and J. E. Powers, "Ultrasonic diagnostic imaging with contrast agents," US5833613 A, 1998.

[9] N. de Jong, M. Emmer, A. van Wamel, and M. Versluis, "Ultrasonic characterization of ultrasound contrast agents," *Med. Biol. Eng. Comput.*, vol. 47, no. 8, pp. 861–873, 2009.

[10] A. N. Nicolaides, *Ultrasound and carotid bifurcation atherosclerosis*. London; New York: Springer-Verlag London Ltd., 2012.

[11] M. Averkiou, M. Lampaskis, K. Kyriakopoulou, D. Skarlos, G. Klouvas, C. Strouthos, and E. Leen, "Quantification of Tumor Microvascularity with Respiratory Gated Contrast Enhanced Ultrasound for Monitoring Therapy," *Ultrasound Med. Biol.*, vol. 36, no. 1, pp. 68–77, 2010.

[12] C. Huang-Wei, A. Bleuzen, P. Bourlier, J. Roumy, A. Bouakaz, L. Pourcelot, and F. Tranquart, "Differential diagnosis of focal nodular hyperplasia with quantitative parametric analysis in contrast-enhanced sonography.," *Invest. Radiol.*, vol. 41, no. 3, pp. 363–368, 2006.

[13] S. B. Feinstein, "Contrast Ultrasound Imaging of the Carotid Artery Vasa Vasorum and Atherosclerotic Plaque Neovascularization," *Journal of the American College of Cardiology*, vol. 48, no. 2. pp. 236–243, 2006.

[14] N. Lassau, S. Koscielny, L. Albiges, L. Chami, B. Benatsou, M. Chebil, A. Roche, and B. J. Escudier, "Metastatic renal cell carcinoma treated with sunitinib: Early evaluation of treatment response using dynamic contrast-enhanced ultrasonography," *Clin. Cancer Res.*, vol. 16, no. 4, pp. 1216–1225, 2010.

[15] S. R. Wilson and P. N. Burns, "Microbubble-enhanced US in body imaging: what role?," *Radiology*, vol. 257, no. 1, pp. 24–39, 2010.

[16] C. Strouthos, M. Lampaskis, V. Sboros, A. Mcneilly, and M. Averkiou, "Indicator dilution models for the quantification of microvascular blood flow with bolus administration of ultrasound contrast agents," *IEEE Trans. Ultrason. Ferroelectr. Freq. Control*, vol. 57, no. 6, pp. 1296–1310, 2010.

[17] A. Hoogi, D. Adam, A. Hoffman, H. Kerner, S. Reisner, and D. Gaitini, "Carotid plaque vulnerability: Quantification of neovascularization on contrast-enhanced ultrasound with histopathologic correlation," *Am. J. Roentgenol.*, vol. 196, no. 2, pp. 431–436, 2011.

[18] T. P. Gauthier, H. S. Wasan, A. Muhammad, D. R. Owen, and E. L. S. Leen, "Assessment of global liver blood flow with quantitative dynamic contrast-enhanced ultrasound.," *J. Ultrasound Med.*, vol. 30, no. 3, pp. 379–385, 2011.

[19] V. Harabis, R. Kolar, M. Mezl, and R. Jirik, "Comparison and evaluation of indicator dilution models for bolus of ultrasound contrast agents.," *Physiol. Meas.*, vol. 34, no. 2, pp. 151–62, 2013.

[20] M. A. Zocco, M. Garcovich, A. Lupascu, E. Di Stasio, D. Roccarina, B. E. Annicchiarico, L. Riccardi, M. E. Ainora, F. Ponziani, G. Caracciolo, G. L. Rapaccini, R. Landolfi, M. Siciliano, M. Pompili, and A. Gasbarrini, "Early prediction of response to sorafenib in patients with advanced hepatocellular carcinoma: The role of dynamic contrast enhanced ultrasound," *J. Hepatol.*, vol. 59, no. 5, pp. 1014–1021, 2013.

[21] N. Lassau, S. Koscielny, L. Chami, M. Chebil, B. Benatsou, A. Roche, M. Ducreux, D. Malka, and V. Boige, "Advanced hepatocellular carcinoma: early evaluation of response to bevacizumab therapy at dynamic contrast-enhanced US with quantification--preliminary results.," 2011.

[22] M. Lampaskis and M. Averkiou, "Investigation of the Relationship of Nonlinear Backscattered Ultrasound Intensity with Microbubble Concentration at Low MI," *Ultrasound Med. Biol.*, vol. 36, no. 2, pp. 306–312, 2010.

[23] A. Thapar, J. Shalhoub, M. Averkiou, C. Mannaris, A. H. Davies, and E. L. S. Leen, "Dose-Dependent Artifact in the Far Wall of the Carotid Artery at Dynamic Contrast-enhanced US," *Radiology*, vol. 262, no. 2. pp. 672–679, 2012.

[24] S. Cocciolillo, “CEUS and Fibroscan in non-alcoholic fatty liver disease and non-alcoholic steatohepatitis,” *World J. Hepatol.*, vol. 6, no. 7, p. 496, 2014.

[25] H. S. Markus and M. J. Harrison, “Estimation of cerebrovascular reactivity using transcranial Doppler, including the use of breath-holding as the vasodilatory stimulus.,” *Stroke.*, vol. 23, no. 5, pp. 668–673, 1992.

[26] C. Grouls, M. Hatting, I. Tardy, J. Bzyl, G. Mühlenbruch, F. F. Behrendt, T. Penzkofer, C. Trautwein, C. Kuhl, F. Kiessling, and M. Palmowski, “Development and validation of an intrinsic landmark-based gating protocol applicable for functional and molecular ultrasound imaging,” *Eur. Radiol.*, vol. 22, no. 8, pp. 1789–1796, 2012.

[27] S. Mulé, N. Kachenoura, O. Lucidarme, A. De Oliveira, C. Pellot-Barakat, A. Herment, and F. Frouin, “An automatic respiratory gating method for the improvement of microcirculation evaluation: application to contrast-enhanced ultrasound studies of focal liver lesions.,” *Phys. Med. Biol.*, vol. 56, no. 16, pp. 5153–5165, 2011.

[28] G. Renault, F. Tranquart, V. Perlbarg, A. Bleuzen, A. Herment, and F. Frouin, “A posteriori respiratory gating in contrast ultrasound for assessment of hepatic perfusion.,” *Phys. Med. Biol.*, vol. 50, no. 19, pp. 4465–4480, 2005.

[29] N. Rognin, R. Campos, J. Thiran, T. Messager, P. Broillet, P. Frinking, M. Mercier, and M. Arditi, “A new approach for automatic motion compensation for improved estimation of perfusion quantification parameters in ultrasound imaging,” in *Proceedings of the 8th French Conference on Acoustics*, 2006, pp. 61–65.

[30] J. Zhang, M. Ding, F. Meng, M. Yuchi, and X. Zhang, “Respiratory motion correction in free-breathing ultrasound image sequence for quantification of hepatic perfusion,” *Medical Physics*, vol. 38, no. 8. p. 4737, 2011.

[31] N. G. Rognin, M. Arditi, L. Mercier, P. J. A. Peter, M. Schneider, G. Perrenoud, A. Anaye, J. Y. Meuwly, and F. Tranquart, “Parametric imaging for characterizing focal liver lesions in contrast-enhanced ultrasound,” *IEEE Trans. Ultrason. Ferroelectr. Freq. Control*, vol. 57, no. 11, pp. 2503–2511, 2010.

[32] M. Jeziorska and D. E. Woolley, “Neovascularization in early atherosclerotic lesions of human carotid arteries: Its potential contribution to plaque development,” *Hum. Pathol.*, vol. 30, no. 8, pp. 919–925, 1999.

[33] P. R. Moreno, K. R. Purushothaman, V. Fuster, D. Echeverri, H. Truszczynska, S. K. Sharma, J. J. Badimon, and W. N. O’Connor, “Plaque neovascularization is increased in ruptured atherosclerotic lesions of human aorta: Implications for plaque vulnerability,” *Circulation*, vol. 110, no. 14, pp. 2032–2038, 2004.

[34] M. J. McCarthy, I. M. Loftus, M. M. Thompson, L. Jones, N. J. M. London, P. R. F. Bell, A. R. Naylor, and N. P. J. Brindle, “Angiogenesis and the atherosclerotic carotid plaque: An association between symptomatology and plaque morphology,” *J. Vasc. Surg.*, vol. 30, no. 2, pp. 261–268, 1999.

[35] G. Geroulakos, G. Ramaswami, A. Nicolaides, K. James, N. Labropoulos, G. Belcaro, and M. Holloway, "Characterization of symptomatic and asymptomatic carotid plaques using high-resolution real-time ultrasonography," *Br. J. Surg.*, vol. 80, no. 10, pp. 1274–1277, 1993.

[36] D. Staub, S. Partovi, A. F. L. Schinkel, B. Coll, H. Uthoff, M. Aschwanden, K. A. Jaeger, and S. B. Feinstein, "Correlation of carotid artery atherosclerotic lesion echogenicity and severity at standard US with intraplaque neovascularization detected at contrast-enhanced US.," *Radiology*, vol. 258, no. 2, pp. 618–626, 2011.

[37] S. Coli, M. Magnoni, G. Sangiorgi, M. M. Marrocco-Trischitta, G. Melisurgo, A. Mauriello, L. Spagnoli, R. Chiesa, D. Cianflone, and A. Maseri, "Contrast-Enhanced Ultrasound Imaging of Intraplaque Neovascularization in Carotid Arteries. Correlation With Histology and Plaque Echogenicity," *J. Am. Coll. Cardiol.*, vol. 52, no. 3, pp. 223–230, 2008.

[38] Z. Akkus, A. Hoogi, G. Renaud, S. C. H. van den Oord, G. L. ten Kate, A. F. L. Schinkel, D. Adam, N. de Jong, A. F. W. van der Steen, and J. G. Bosch, "New Quantification Methods for Carotid Intra-plaque Neovascularization Using Contrast-Enhanced Ultrasound," *Ultrasound Med. Biol.*, vol. 40, no. 1, pp. 25–36, 2014.

[39] L. Xiong, Y.-B. Deng, Y. Zhu, Y.-N. Liu, and X.-J. Bi, "Correlation of carotid plaque neovascularization detected by using contrast-enhanced US with clinical symptoms.," *Radiology*, vol. 251, no. 2, pp. 583–589, 2009.

[40] S. Kaul, P. Kelly, J. D. Oliner, W. P. Glasheen, M. W. Keller, and D. D. Watson, "Assessment of regional myocardial blood flow with myocardial contrast two-dimensional echocardiography.," *J. Am. Coll. Cardiol.*, vol. 13, no. 2, pp. 468–482, 1989.

2

Automatic respiratory gating for contrast ultrasound evaluation of liver lesions

Published as: Damianos Christofides, Edward Leen and Michalakis A. Averkiou, "Automatic respiratory gating for contrast ultrasound evaluation of liver lesions", IEEE Transactions in Ultrasonics and Ferroelectric Frequency Control. 2014 Jan;60(1):25-32. doi: 10.1109/TUFFC.2014.6689773

Patent Application: Michalakis A Averkiou and Damianos Christofides, "Eliminating motion effects in medical images caused by physiological function," World Intellectual Property Organization Patent Application #WO2014111860 A2. Publication Date: July 24, 2014. (Appendix 1)

Abstract

Dynamic contrast-enhanced ultrasound (DCEUS) has been used in radiology for many years for lesion detection and characterization. In the recent years, more emphasis has been placed on tumor perfusion quantification with DCEUS. To ensure accuracy in both quantitative and qualitative evaluation of liver tumors with DCEUS, sources of noise in clinical data must be identified and, if possible, removed. One of the major sources of such noise is respiratory motion. A new automatic respiratory gating (ARG) algorithm is presented and evaluated with clinical data. The results of the evaluation demonstrate the potential of the ARG algorithm for clinical use as a fast and easy to implement method in removing respiratory motion from DCEUS loops.

2.1 Introduction

Microbubbles have been used in medical ultrasound imaging since the mid-1990s [1]. Microbubbles have the advantage of being a pure blood-pool contrast agent because they are similar in size with red blood cells [2], [3], allowing for the imaging of perfusion in real time. Ultrasound imaging with microbubbles or dynamic contrast-enhanced ultrasound (DCEUS) has found uses in the evaluation of response to treatment of liver metastases [4], the analysis of focal nodular hyperplasia in the liver [5], the detection of coronary disease [6], and the assessment of microvascular damage after a myocardial infarction [7].

Quantification of DCEUS image loops provides important blood flow information on tumor microcirculation [8]. One of the biggest challenges in quantitative DCEUS for liver lesions is motion caused by respiration. Respiratory motion can cause the lesion, as it appears in the imaging plane, to change in size, shape and location (Figure 2-1). This causes problems in the qualitative evaluation of the lesion, because the clinician needs to take into account the movement of the lesion to evaluate its size and perfusion patterns. This type of motion might also cause significant problems in the quantitative evaluation of the lesion's perfusion, because the lesion will be moving in and out of a region-of-interest (ROI) that samples the DCEUS mean linear intensity and thus introducing noise artifacts.

Various approaches have been used clinically to compensate for the effects of respiratory motion. One such approach is directing the patient to hold his or her breath at a specific breathing cycle phase desired by the clinician or sonographer, but this technique applies only to patients that have the ability to perform a breath hold that can last more than 40 s; another disadvantage of this technique is that hemodynamics are affected during

breath holds [9], [10]. Another technique for respiratory motion compensation found in the literature [4] is to identify the position of the diaphragm at a reference position and reject frames in which the diaphragm deviates from the reference position. This is also a post-processing technique (it is implemented after the acquisition of the ultrasound loop) and it relies on the operator expertise to identify the brightest moving reflector.

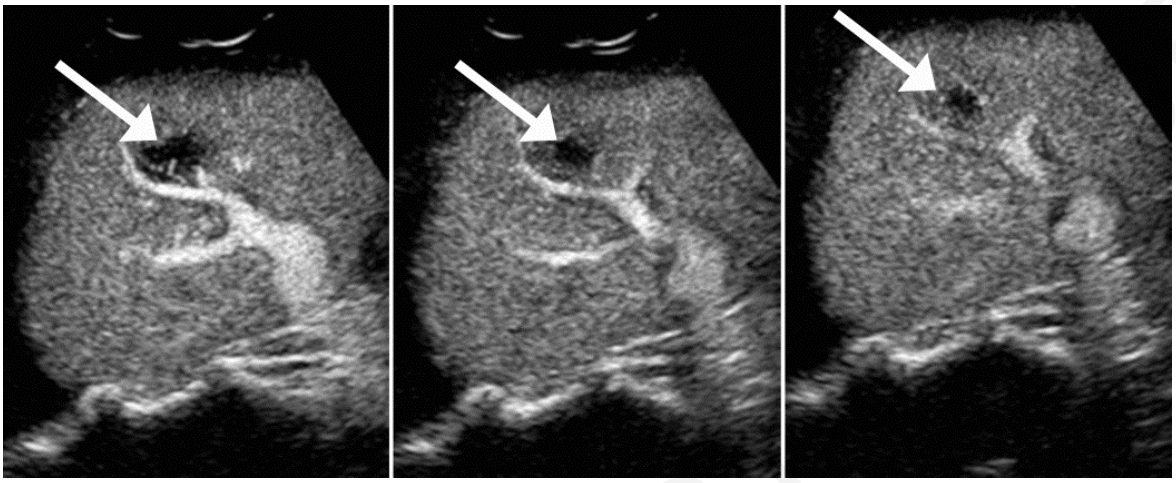

Figure 2-1: Example of the changes of the size, location, and shape of a liver lesion, in a dynamic contrast-enhanced ultrasound (DCEUS) loop, at three different time instances. These changes are mainly attributed to respiratory motion.

Several computational techniques have been proposed in the literature that would allow for fully or semi-automated compensation of respiratory motion. Renault et al. [11] introduced a technique based on independent component analysis (ICA) with which the respiratory cycle could be extracted manually from the ICA-derived components that represent motion; a threshold can be used on the final respiratory kinetics curve to derive the frames that belong to the end phases of the respiratory cycle. Mulé et al. [12] used principal component analysis (PCA) to extract the respiratory kinetics to perform fully automatic gating. A drawback of both these techniques is that, because the ultrasound acquisition is two-dimensional, there is uncertainty on the portion of the lesion, if any, that will be present at the extreme phases of the respiratory cycle, because of out-of-plane motion.

Rigid registration is another technique used to compensate for respiratory motion. Rognin et al. [13], [14] used a rigid registration technique, with 2-D translation and rotation, to realign frames to a reference frame; a disadvantage of this approach is that out-of-plane frames might be difficult, if not impossible, to re-align. Zhang et al. [15] also used rigid registration, with 2-D translation only, and frame selection to perform automatic gating; the algorithm rejected out-of-plane frames but it required a long computation time that would not be realistic in a clinical context. Both of these techniques require the user to

manually draw ROI(s) on frames to denote the search space for the registration to take place.

In the present work, a new post-processing method is proposed for automatic respiratory gating (ARG) of dual-contrast imaging (an anatomical B-mode image and a contrast-specific image displayed side-by-side in the same frame) loops. The only input needed by the user is to select a trigger frame in which the lesion is clearly seen and can be delineated. The new ARG algorithm is easy to implement and use, fast, and leads to a simple workflow for the clinical operator.

2.2 Materials and methods

2.2.1 ARG algorithm

The ARG algorithm applies to the B-mode loop of the dual-contrast imaging loop acquisition because the anatomical information in the B-mode loop is less sensitive to intensity variation than the contrast loop. The algorithm is presented as implemented in this study but modifications can be made to the algorithm to change its speed and/or performance. The software package Matlab (v. 2007b, The MathWorks Inc., Natick, MA) was used to implement the ARG algorithm.

2.2.1.1 Quantify amount of motion

Consider a B-mode loop consisting of N frames, $\{I_i\}_{i=1}^{N}$. First, the B-mode loop was downsampled by a factor of 2 (i.e., every other frame is kept) and resized using nearest-neighbor interpolation by a factor of 0.3. The resulting sequence of frames was stored as a new loop, $\{\hat{I}_i\}_{i=1}^{\hat{N}}$. To detect the motion present, each resulting frame was subtracted from the average of all the frames [16] (Figure 2-2). The sequence of frames resulting from the subtraction is defined by

$$\{M_i\}_{i=1}^{\hat{N}} = \left\{ \hat{I}_i - \left(\frac{1}{\hat{N}} \sum \{\hat{I}_i\}_{i=1}^{\hat{N}} \right) \right\}_{i=1}^{\hat{N}} . \quad (1)$$

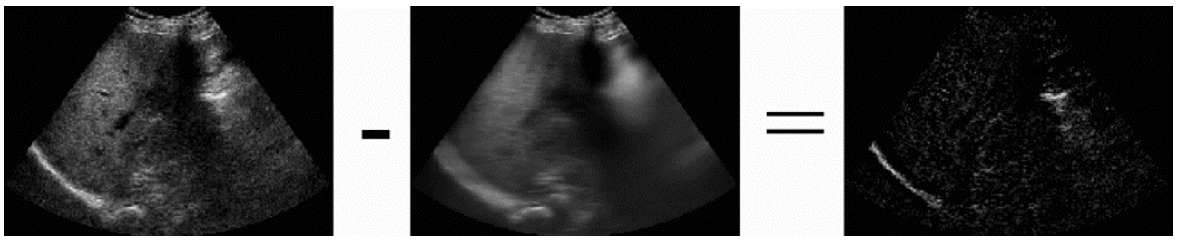

Figure 2-2: Subtraction of a frame from the average of the $\left\{\hat{I}_i\right\}_{i=1}^{\hat{N}}$ sequence. Note the relative increase of brightness of the diaphragm in the resulting frame with the original frame of the $\left\{\hat{I}_i\right\}_{i=1}^{\hat{N}}$ sequence.

Next, the frames from $\left\{M_i\right\}_{i=1}^{\hat{N}}$ were threshold to binary by the 30% of the maximum value of each frame. The resulting frames suffered from the presence of noise from single and small clusters of bright pixels present in the $\left\{M_i\right\}_{i=1}^{\hat{N}}$ sequence. This problem was addressed by first removing single pixels from the thresholded binary images and then keeping only the n largest groups of clusters of connected pixels, called structures hereafter. The removal of single pixels was implemented using the morphological operation *clean* of the *bwmorph* function and the extraction of the largest structure using the *Area* operation of the *regionprops* function both, part of Matlab's Image Processing Toolbox. The sequential procedures of applying a threshold on the frames and the retention of the *n* largest structures will be referred to hereafter as image operator $\Im$. The $\Im$ operator takes two arguments: X that can be a frame or sequence of frames, and *n*, which is the number of largest structures that will be extracted by the operator. The $\Im$ operator was applied on the $\left\{M_i\right\}_{i=1}^{\hat{N}}$ sequence and the resulting binary frames were stored in the sequence $\left\{P_i\right\}_{i=1}^{\hat{N}}$ (Figure 2-3), according to

$$\left\{P_i\right\}_{i=1}^{\hat{N}} = \Im\left\langle \left\{M_i\right\}_{i=1}^{\hat{N}}, \mathrm{n} \right\rangle, \text{ with } \mathrm{n} = 1 \ . \tag{2}$$

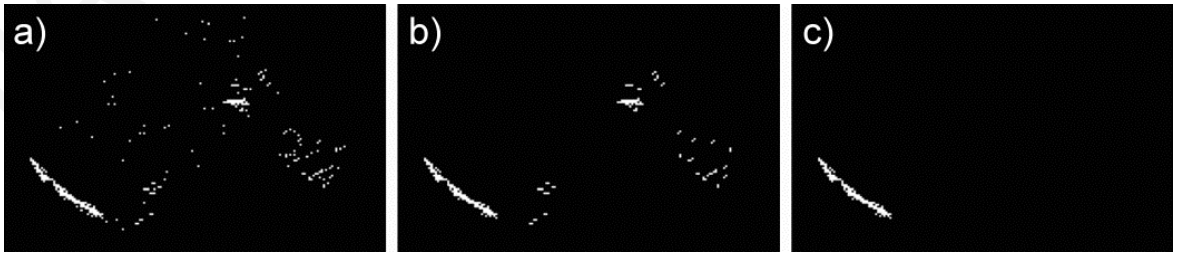

Figure 2-3: Extraction of the largest moving structure from the $\left\{M_i\right\}_{i=1}^{\hat{N}}$ sequence: a) threshold image to binary by the 30% of the maximum pixel value, b) remove single pixels, and c) keep only the first largest structure.

Each frame from the $\{P_i\}_{i=1}^{\hat{N}}$ sequence holds a moving structure extracted from the corresponding B-mode frame; thus, if all the frames from the $\{P_i\}_{i=1}^{\hat{N}}$ sequence are added together, a map of the motion present in the whole B-mode loop can be produced. The result was a matrix made up of integer-value elements; each element in this matrix was associated with the amount of motion present at the corresponding pixel coordinate in the whole of the B-mode loop. This matrix was called the motion information matrix (MIM) (Figure 2-4) and was calculated using

$$MIM = \sum \{P_i\}_{i=1}^{\hat{N}} \ . \tag{3}$$

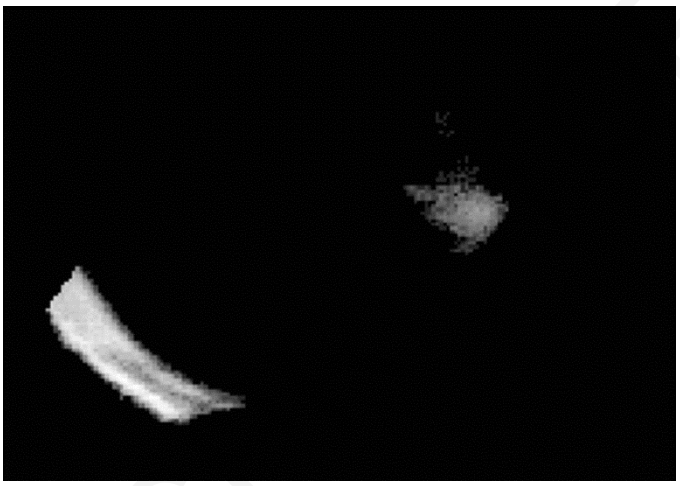

Figure 2-4: Example motion information matrix (MIM). Observe the two main areas in which motion occurs. The dominant structure producing motion is the diaphragm. Note that the values shown have been log-compressed to make the data easier to visualize.

2.2.1.2 Establish breathing cycle to be extracted

As previously mentioned, the user must define the trigger frame before the ARG procedure begins. This frame defines the breathing cycle phase that was extracted by the ARG algorithm. First, the trigger frame was subtracted from the average of the uncompressed (without the reduction in the resolution)/undownsampled B-mode loop:

$$M_{trigger} = I_{trigger} - \frac{1}{N} \sum \{I_i\}_{i=1}^{N} \ . \tag{4}$$

The $\Im$ image processing operator was then applied on the $M_{trigger}$ frame according to

$$P_{trigger} = \Im\langle M_{trigger}, 5 \rangle \ . \tag{5}$$

The MIM was resized to the original B-mode loop frame size using bicubic interpolation. The $P_{trigger}$ frame's structures were overlaid over the MIM, and the mean

intensity MIM value was calculated within each structure (Figure 2-5). These values were stored in the $\{S_M\}_{i=1}^{5}$ sequence, where the index *i* corresponds to each extracted structure.

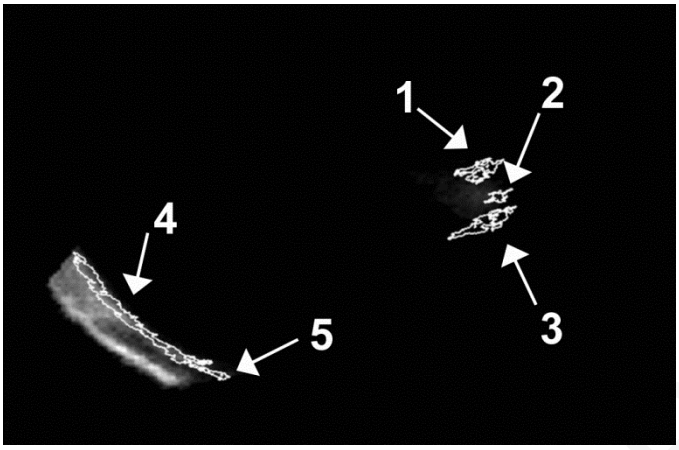

Figure 2-5: Moving structures extracted from the trigger frame overlaid over the motion information matrix (MIM). The structures are labeled for reference purposes.

The $\{S_M\}_{i=1}^{5}$ sequence holds values of the amount of motion associated with each structure. This motion or change in the grayscale values of the B-mode loop frames could be due to respiration, cardiac motion, contrast agent presence, or any other change in the gray scale values of the B-mode loop through time.

In the interest of establishing whether the motion associated with each structure can be attributed to respiration, the mean grayscale intensity values for each frame of the B-mode loop within a square measuring 30 x 30 pixels was calculated. The size of the square was selected by considering two competing factors: 1) the standard error of the mean of the grayscale intensity values decreases with the size of the square; and 2) a very large square would fail to detect motion from small moving structures. Based on these two factors, a 30x30 square is optimal. The center of the square was placed at the center of mass of each structure of the $P_{trigger}$ frame. Each structure on the $P_{trigger}$ frame was identified by a specific index number assigned using the *bwlabel* function and the center of mass of each structure was calculated using the *Centroid* operation of the *regionprops* function, both part of Matlab's Image Processing Toolbox. This operation returned the time-intensity curve (TIC) associated with each extracted structure from the trigger frame. A square was used to extract the TIC, rather than using each structure as a binary mask, to reduce calculation time by approximately a factor of three. The next step was to calculate the Fourier Transform (FT) of each TIC so its frequency contents could be analyzed (Figure 2-6).

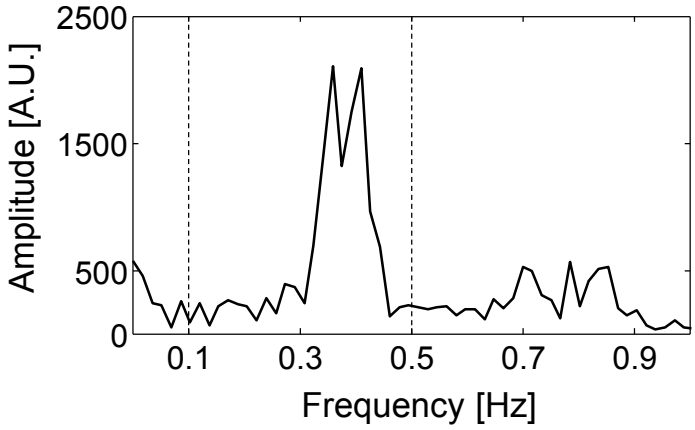

Figure 2-6: The Fourier Transform of the time-intensity curve (TIC) extracted from structure labeled 4 in Figure 2-5. The respiration cycle bandwidth is denoted with the dashed vertical lines.

A metric was needed to quantify the presence the respiratory motion associated with each structure extracted from the trigger frame; these metric values were stored in the $\{S_F\}_{i=1}^{5}$ sequence. $\{S_F\}_{i=1}^{5}$ values were calculated as the area of the frequency spectrum between 0.1 and 0.5 Hz divided by the sum of the area from 0 to 0.1 Hz and the area between 0.5 to 1 Hz:

$$\{S_F\}_{i=1}^{5} = \frac{\int_{0.1}^{0.5} F_i(f)\,df}{\int_{0}^{0.1} F_i(f)\,df + \int_{0.5}^{1} F_i(f)\,df} \tag{6}$$

The rationale for (6) is that the area between 0.1 and 0.5Hz represents contributions to the frequency spectrum by respiration. The 0 to 0.1 Hz range represents contributions from slow changing events, such as the change of grayscale values caused by the flow of microbubbles, and the 0.5 to 1 Hz frequency range represents sources of noise or physiological motion other than respiration present in the TIC curve. Thus, from (6), it can be observed that the values stored in $\{S_F\}_{i=1}^{5}$ increase as respiratory motion presence increases and undesired change in grayscale values in the B-mode loop decreases.

Another metric that was recorded was whether the maximum value of the amplitude of the frequency spectrum lay within the respiration frequency range or not. This is a binary metric, stored in the $\{S_B\}_{i=1}^{5}$ sequence, and it takes the values of either 0 or 1.

The combined metric, stored in the $\{S\}_{i=1}^{5}$ sequence, is defined as

$$\{S\}_{i=1}^{5} = \left(0.6 \times \frac{\{S_M\}_{i=1}^{5}}{\max\{S_M\}_{i=1}^{5}}\right) + \left(0.4 \times \frac{\{S_F\}_{i=1}^{5}}{\max\{S_F\}_{i=1}^{5}}\right). \tag{7}$$

Eq. (7) holds unless a structure receives an S_B of 0, then the corresponding s metric also receives a value of 0. If all the values $\{S\}_{i=1}^{5}$ were given a zero value, then the $\{S\}_{i=1}^{5}$ sequence reverted back to its original values before the consideration of S_B. In Table 2-1, example $\{S_M\}_{i=1}^{5}, \{S_F\}_{i=1}^{5}, \{S_B\}_{i=1}^{5}$, and $\{S\}_{i=1}^{5}$ values are shown for the structures in Figure 2-5.

Table 2-1: Example of scores received by various structures shown in Figure 2-5.

Structure Index	S_M	S_F	S_B	s
1	2.27	0.89	0	0.00
2	5.68	0.85	0	0.00
3	1.40	1.04	0	0.00
4	24.25	1.65	1	0.90
5	8.61	2.21	1	0.61

The TIC corresponding to the structure that receives the highest $\{S\}_{i=1}^{5}$ score value was extracted again, this time using the structure as a binary mask applied on the B-mode loop. This was done in order to ensure maximum quality for the next step of the ARG procedure.

2.2.1.3 Final step of ARG procedure

The final step of the ARG procedure involves finding the location of the peaks and troughs of the TIC of the structure that receives the highest s score. Peaks are indicative of the presence of a structure on the position it occupied on the trigger frame, whereas troughs indicate the absence of the structure from its position on the trigger frame. To locate the peaks of the TIC, the approximate time between the peaks of the TIC was calculated using the frequency spectrum. By locating the frequency at which the maximum amplitude occurs within the respiratory range (0.1 to 0.5 Hz), $f_{\max}$, the time between the peaks was approximated as $T_{\max} = \left(f_{\max}\right)^{-1}$. The peaks were then located based on their separation being no less than $\frac{T_{\max}}{2}$; this allows for flexibility because patient respiration frequency can fluctuate during examination. The location of the peaks was implemented by setting the parameter *MINPEAKDISTANCE* of Matlab's Signal Processing Toolbox *findpeaks* function to $\frac{T_{\max}}{2}$.

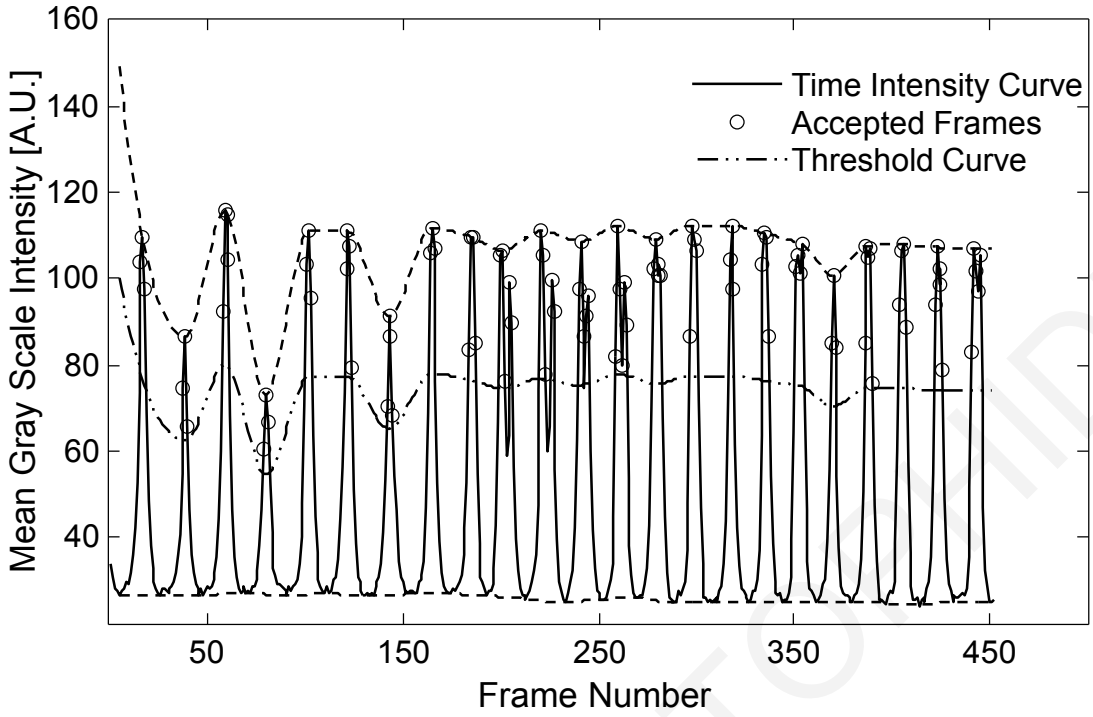

Figure 2-7: Gated time-intensity curve (TIC) extracted from structure 4, shown in Figure 2-5.

Once the peaks of the TIC were located, a piecewise cubic Hermite interpolating polynomial (pchip) was fitted on the peaks. The TIC was inverted and the same procedure was repeated to locate the troughs and fit a pchip on the troughs; thus, the envelope of the TIC was calculated. A threshold of 40% was then applied on the envelope of the signal and only frames that were above this threshold were accepted, the rest were rejected. The 40% value was established after considering the robustness of the fit of the lognormal model onto the data and at the same time optimizing the goodness of fit of the model. The frames that were accepted made up the ARG loop and were, within a threshold, at the same breathing cycle phase as the trigger frame (Figure 2-7).The whole ARG algorithm is laid out in a flowchart shown in Figure 2-8.

2.2.2 Imaging protocol

Eighteen (18) patients (7 female, 11 male) with liver metastasis were imaged. Approval for the scanning was obtained by the ethics review board of our hospital. The procedure was fully explained to all participating patients and informed consent was obtained.

All imaging was performed with a Philips iU22 scanner (Philips Medical Systems, Bothell, WA) using the C5-1 imaging probe. The imaging frequency was 1.7MHz, the pulsing imaging sequence used was power modulation (PM) with a mechanical index (MI) of less than 0.06, and the frame rate varied between 7 and 10 Hz. The acquisition mode

was dual-contrast imaging and 2-min loops were acquired. During the acquisition, the focus was set well below the depth of the lesion to ensure uniform pressure field. The time gain compensation (TGC) gain was adjusted in such a way that it was uniform across depth and avoided signal saturation. Before the arrival of the contrast agent, there was a hint of uniform noise in the image as an assurance that the TGC gain was at the threshold of detection.

A 2.4mL bolus of Sonovue (Bracco s.p.a., Milan, Italy) was injected. The radiologis, acquiring the loops maintained a constant imaging plane by observing the tissue side of the acquisition.

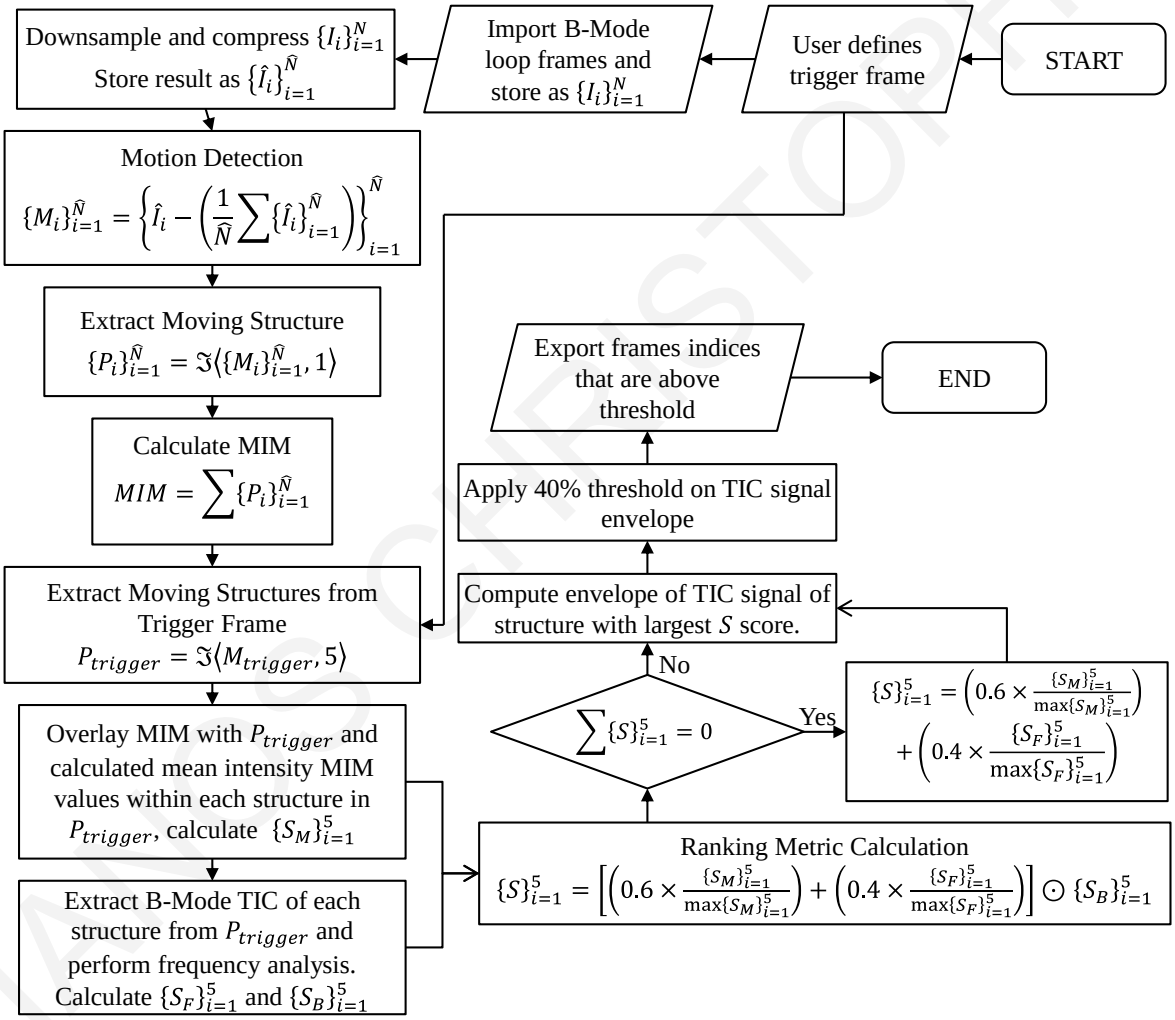

Figure 2-8: Flowchart of the automatic respiratory gating (ARG) algorithm.

2.2.3 Quantification approach

The patient DICOM loops acquired with the Philips iU22 scanner were transferred to a workstation running the commercial quantification software QLAB (v. 8.1, Philips Medical Systems, Bothell, WA). An ROI was manually drawn on the trigger frame of the

DCEUS loop encompassing the lesion (Figure 2-9). Both the arterial and late portal phases of the DCEUS loop were used for the accurate drawing of the ROI [4].

Time-intensity curves from linearized image data were extracted using the QLAB software and saved to a text file. The B-mode loop image data, the trigger frame index, and the frame rate of the acquisition were also saved. This information was passed on to the Matlab implementation of the ARG algorithm. After processing by the ARG algorithm, a new lesion TIC was produced.

Figure 2-9: Region of interest (ROI) drawn encompassing lesion on trigger frame of dynamic contrast-enhanced ultrasound (DCEUS) loop, shown here in late portal phase. The mean linear intensity DCEUS values are extracted from within this ROI.

2.2.4 Data analysis

To assess the effectiveness of the ARG algorithm, both the TICs extracted with and without ARG processing were fitted on a lognormal indicator dilution model [8]. The goodness of fit of the data to the model was established using the coefficient of determination (R^2) and the root mean square error (*RMSE*), shown in (8) and (9), respectively,

$$R^2 = 1 - \frac{\sum_i \left(y_i - f_i\right)^2}{\sum_i \left(y_i - \bar{y}_i\right)^2} \tag{8}$$

$$RMSE = \sqrt{\frac{\sum_{i=1}^{n} \left(y_i - f_i\right)^2}{n}}\ , \tag{9}$$

where y_i are the linear intensity data points, f_i are the corresponding points from the lognormal model fit, $\bar{y}$ is the mean value of the y_i points and n is the number of data points. An example of such an analysis is shown in Figure 2-10.

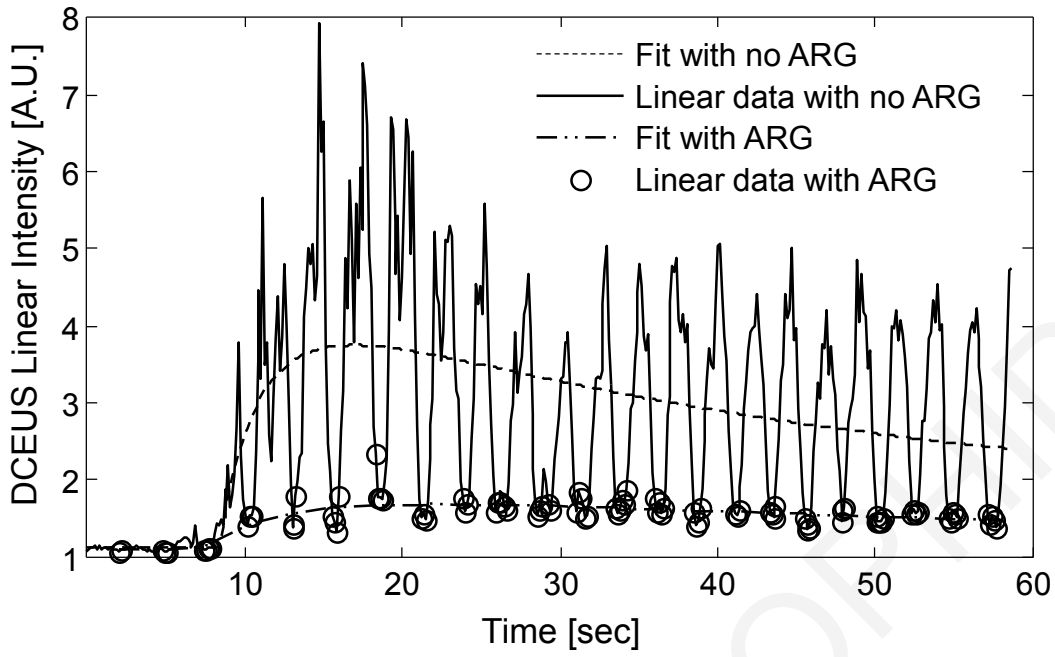

Figure 2-10: Mean linear intensity data from a region of interest (ROI) around a lesion with and without automatic respiratory gating (ARG), including the fits on the lognormal indicator dilution model. In this example, the R^2 of the fit with and without ARG are 0.89 and 0.37, respectively.

To arrive at useful conclusions, the data were visualized as boxplots. The limits of the boxes are the 25% (Q_1) and 75% (Q_3) quartiles and the middle of the box indicates the median of the data. The lower limit of the whiskers is F_L=Q_1-[1.5x(Q_3-Q_1)] and the upper limit of the whiskers is F_U=Q_3+[1.5x(Q_3-Q_1)]. All data that are outside F_L and F_U are considered outliers. The boxplots have notches indicating 95% confidence intervals for the median, the limits of which are calculated as $median \pm 1.57 \times \frac{(Q_3 - Q_1)}{\sqrt{N}}$, where N is the number of samples.

Further to the boxplots of the data, one-tail paired *t*-tests with unequal variances were performed using the R programming language [17] and the pwr package [18] was used to calculate the power of the *t*-tests performed.

2.3 Results

The results of the *t*-test performed on the R^2 with and without ARG processing show a p-value less than 0.05 with a *t*-test power of 1.00. A p-value of less than 0.05 is also calculated for the *RMSE* data with a *t*-test power of greater than 0.93. The p-values calculated and the powers of the tests allow for confident conclusions to be drawn from the analysis.

In Figure 2-11 boxplots of the R^2 and *RMSE* values of the lognormal model fits are plotted with and without ARG. From Figure 2-11a) it can be seen that the R^2 95%

confidence interval notches on the boxplots of with and without ARG processing are not overlapping. This is not the case, however ,with the *RMSE* boxplot 95% confidence interval notches.

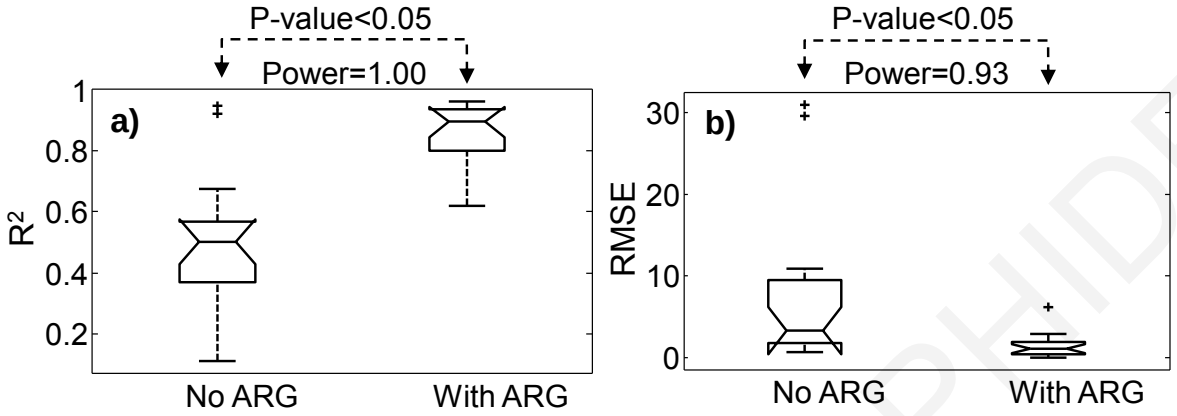

Figure 2-11: a) Boxplots of the R^2 values and b) boxplots of the root mean square error (RMSE) for the model fit of the clinical cases analyzed with and without automatic respiratory gating (ARG). The notches on the boxplots are the 95% confidence levels of the median. The p-values and the power at 95% confidence level of *t*-tests performed are also included.

It should also be noted that the ARG algorithm, as implemented in Matlab 2007b, had a mean run time of 0.87±0.10 (standard deviation) seconds per 100 frames on an Intel E8400 (Intel Corp., Santa Clara, CA) at 3GHz with 2GB RAM. These run times are faster than those previously published in the literature [11], [12], [15].

2.4 Discussion

From Figure 2-11, it is evident both from the notches on the boxplots and the *t*-test results that the R^2 is indeed improved with the use of ARG, within a 95% confidence interval. However regarding the *RMSE*, although the *t*-test arrives at the conclusion that by using ARG the *RMSE* is significantly lower than without using ARG, there is an overlap of 1.2 *RMSE* units in the 95% confidence interval notches of the boxplots.

This mismatch is believed to be caused by the two outlier points seen clearly in Figure 2-11a) that have an R^2 value, without the use ARG, of more than 0.8. In Figure 2-12, the boxplots are re-drawn, this time omitting the two outlier cases; note that the statistical power of the *t*-test on the *RMSE* data has increased, although marginally. Also note that the notches of the boxplots, in this case, do not overlap either for the R^2 or *RMSE* boxplots. It is believed that certain patient's data do not suffer from respiratory motion as much as others even though, of course, there is respiratory motion present.

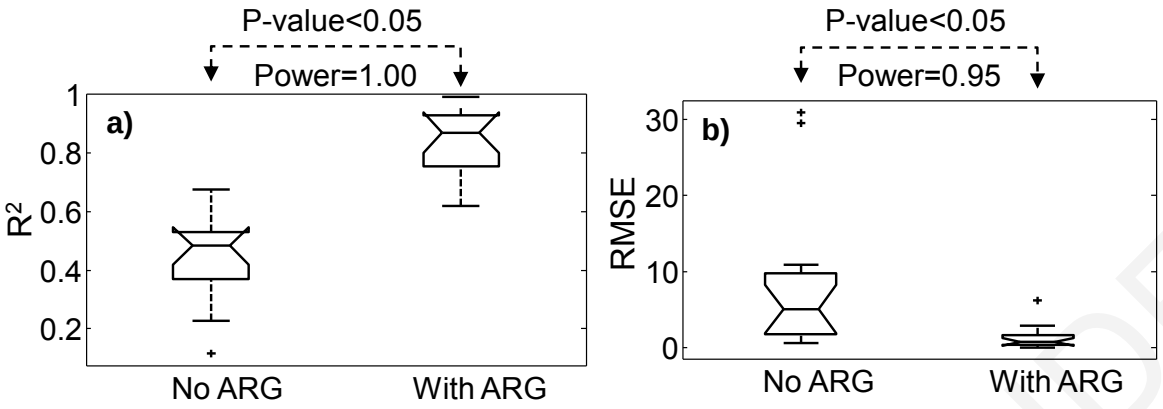

Figure 2-12: a) Boxplots of the R^2 values and b) boxplots of the root mean square error (RMSE) for the model fit of the clinical cases analyzed with and without ARG, not including the outlier cases. The notches on the boxplots are 95% confidence levels around the median. The p-values and the power at 95% confidence level of *t*-tests performed are also included.

Another important assumption underlying this work is that a better fit of the data to the model suggests more accurate results on the hemodynamics of the lesion. This assumption considers respiratory motion as noise added to the data which, if removed, will provide more accurate results. However, it is very difficult to refer to "more accurate results" when the real perfusion of the lesion is unknown.

In addition to significantly increasing the goodness of fit of the lesion linear intensity data to the lognormal indicator dilution model, ARG results in effective frame downsampling by eliminating frames that are not useful for quantitative or qualitative evaluation. This frame downsampling makes the evaluation of the image loop faster by reducing the time required to calculate the fit of an indicator dilution model to the data, in the qualitative evaluation of the loop, and in parametric imaging approaches. The rejection of frames that are out of phase with the presence of the lesion on the imaging plane can reduce the processing time for motion-compensation algorithms that use computing-intensive image processing techniques such as image registration [13]–[15].

For the goals of the current study, only a single phase of the breathing cycle was extracted by the ARG algorithm. However, there are clinical situations in which multiple breathing cycle phases must be extracted. An example of such a clinical situation is the presence of multiple lesions that cannot be captured on a single imaging plane. This multiphase extraction can be achieved using the ARG algorithm and modifying the gating of the lesion's TIC (Figure 2-7) so that the signal envelope of the TIC is segmented into several parts, each representing a different breathing cycle phase.

This work concentrated on DCEUS of liver lesions but it should be noted that the ARG algorithm can be implemented in other DCEUS studies, such as the evaluation of

blood flow in the hepatic artery and portal vein [19], [20]. Moreover, the ARG algorithm can also be used in conventional B-mode imaging to help with qualitative evaluation of video loops.

The novel algorithm presented addresses limitations of computational methods for compensation of respiratory motion found in the literature, such as the ability to select any breathing cycle phase desired by the clinician instead of extracting the end phases of the breathing cycle [11], [12]. The only user input required by the ARG algorithm is the trigger frame, whereas other methods in the literature require the user to draw ROIs on frames to perform rigid registration [13-15], a requirement that has the potential to introduce time delays in the clinical workflow.

Finally, it should be noted that the ARG algorithm cannot be applied in cases where there was an accidental move (by either the operator or the patient) that changed the image plane, unless the original image plane is recovered later in the loop. In such a case, the ARG algorithm will eliminate all motion frames acquired after the change of the imaging plane. Empirically, the minimum number of frames needed to perform a robust fit on the model lies between 100-150 frames for a 2-min acquisition.

2.5 Conclusion

This study presents an ARG algorithm that can improve both the qualitative and quantitative analysis of DCEUS loops. The ARG algorithm requires only the selection of the trigger frame that defines the breathing cycle phase to be extracted and performs all other tasks automatically. The implementation of such algorithm is possible on any diagnostic ultrasound system that has a dual-contrast imaging mode. Furthermore, the patient is not required to alter his/her breathing, allowing for a comfortable examination. The effectiveness of the ARG algorithm in removing respiratory motion in a clinical setting has been demonstrated by the results of this study. Finally, this algorithm is very fast; it may remove respiratory motion from a 1000 frames loop in 8 seconds.

References

[1] P. N. Burns, "Harmonic imaging with ultrasound contrast agents.," *Clin Radiol*, vol. 51 Suppl 1, pp. 50–5, Feb. 1996.

[2] M. Averkiou, M. Bruce, S. Jensen, P. Rafter, T. Brock-Fishe, and J. Powers, "Pulsing schemes for the detection of nonlinear echoes from contrast microbubbles," in *9th European Symposium on Ultrasound Contrast Imaging*, 2004, pp. 17–24.

[3] K. Wei, A. R. Jayaweera, S. Firoozan, A. Linka, D. M. Skyba, and S. Kaul, "Basis for detection of stenosis using venous administration of microbubbles during myocardial contrast echocardiography: bolus or continuous infusion?," *J Am Coll Cardiol*, vol. 32, no. 1, pp. 252–260, Jul. 1998.

[4] M. Averkiou, M. Lampaskis, K. Kyriakopoulou, D. Skarlos, G. Klouvas, C. Strouthos, and E. Leen, "Quantification of tumor microvascularity with respiratory gated contrast enhanced ultrasound for monitoring therapy.," *Ultrasound Med Biol*, vol. 36, no. 1, pp. 68–77, Jan. 2010.

[5] C. Huang-Wei, A. Bleuzen, P. Bourlier, J. Roumy, A. Bouakaz, L. Pourcelot, and F. Tranquart, "Differential diagnosis of focal nodular hyperplasia with quantitative parametric analysis in contrast-enhanced sonography.," *Invest Radiol*, vol. 41, no. 3, pp. 363–8, Mar. 2006.

[6] R. Senior, M. Monaghan, M. L. Main, J. L. Zamorano, K. Tiemann, L. Agati, N. J. Weissman, A. L. Klein, T. H. Marwick, M. Ahmad, A. N. DeMaria, M. Zabalgoitia, H. Becher, S. Kaul, J. E. Udelson, F. J. Wackers, R. C. Walovitch, and M. H. Picard, "Detection of coronary artery disease with perfusion stress echocardiography using a novel ultrasound imaging agent: two Phase 3 international trials in comparison with radionuclide perfusion imaging.," *Eur J Echocardiogr*, vol. 10, no. 1, pp. 26–35, Jan. 2009.

[7] L. Galiuto, B. Garramone, A. Scarà, A. G. Rebuzzi, F. Crea, G. La Torre, S. Funaro, M. Madonna, F. Fedele, and L. Agati, "The Extent of Microvascular Damage During Myocardial Contrast Echocardiography Is Superior to Other Known Indexes of Post-Infarct Reperfusion in Predicting Left Ventricular Remodeling," *J Am Coll Cardiol*, vol. 51, no. 5, pp. 552–9, Feb. 2008.

[8] C. Strouthos, M. Lampaskis, V. Sboros, A. McNeilly, and M. Averkiou, "Indicator dilution models for the quantification of microvascular blood flow with bolus administration of ultrasound contrast agents.," *IEEE Trans Ultrason Ferroelectr Freq Control*, vol. 57, no. 6, pp. 1296–310, Jun. 2010.

[9] H. S. Markus and M. J. Harrison, "Estimation of cerebrovascular reactivity using transcranial Doppler, including the use of breath-holding as the vasodilatory stimulus.," *Stroke*, vol. 23, no. 5, pp. 668–73, May 1992.

[10] M. Müller, M. Voges, U. Piepgras, and K. Schimrigk, "Assessment of cerebral vasomotor reactivity by transcranial Doppler ultrasound and breath-holding. A

comparison with acetazolamide as vasodilatory stimulus.," *Stroke*, vol. 26, no. 1, pp. 96–100, Jan. 1995.

[11] G. Renault, F. Tranquart, V. Perlbarg, A. Bleuzen, A. Herment, and F. Frouin, "A posteriori respiratory gating in contrast ultrasound for assessment of hepatic perfusion.," *Phys Med Biol*, vol. 50, no. 19, pp. 4465–80, Oct. 2005.

[12] S. Mulé, N. Kachenoura, O. Lucidarme, A. De Oliveira, C. Pellot-Barakat, A. Herment, and F. Frouin, "An automatic respiratory gating method for the improvement of microcirculation evaluation: application to contrast-enhanced ultrasound studies of focal liver lesions.," *Phys Med Biol*, vol. 56, no. 16, pp. 5153–65, Aug. 2011.

[13] N. G. Rognin, M. Arditi, L. Mercier, P. J. A. Frinking, M. Schneider, G. Perrenoud, A. Anaye, J.-Y. Meuwly, and F. Tranquart, "Parametric imaging for characterizing focal liver lesions in contrast-enhanced ultrasound.," *IEEE Trans Ultrason Ferroelectr Freq Control*, vol. 57, no. 11, pp. 2503–11, Nov. 2010.

[14] N. Rognin, R. Campos, J. Thiran, T. Messager, P. Broillet, P. Frinking, M. Mercier, and M. Arditi, "A new approach for automatic motion compensation for improved estimation of perfusion quantification parameters in ultrasound imaging," in *Proceedings of the 8th French Conference on Acoustics*, 2006, pp. 61–65.

[15] J. Zhang, M. Ding, F. Meng, M. Yuchi, and X. Zhang, "Respiratory motion correction in free-breathing ultrasound image sequence for quantification of hepatic perfusion," *Med Phys*, vol. 38, no. 8, pp. 4737–4748, Aug. 2011.

[16] A. Jain, *Fundamentals of Digital Image Processing*. Englewood Cliffs, NJ: Prentice-Hall, 1989.

[17] R Core Team. (2013, Oct.). R: A Language and Environment for Statistical Computing. [Online]. Available: http://www.r-project.org

[18] S. Champely. (2013, Oct.). pwr: Basic functions for power analysis. [Online]. Available: http://cran.r-project.org/web/packages/pwr/index.html

[19] T. P. Gauthier, A. Muhammad, H. S. Wasan, P. D. Abel, and E. L. S. Leen, "Reproducibility of quantitative assessment of altered hepatic hemodynamics with dynamic contrast-enhanced ultrasound.," *J Ultrasound Med*, vol. 31, no. 9, pp. 1413–20, Sep. 2012.

[20] T. P. Gauthier, H. S. Wasan, A. Muhammad, D. R. Owen, and E. L. S. Leen, "Assessment of global liver blood flow with quantitative dynamic contrast-enhanced ultrasound.," *J Ultrasound Med*, vol. 30, no. 3, pp. 379–85, Mar. 2011.

3

Improvement of the accuracy of liver lesion DCEUS quantification with the use of automatic respiratory gating

Published as: Damianos Christofides, Edward Leen and Michalakis A. Averkiou, "Improvement of the accuracy of liver lesion DCEUS quantification with the use of automatic respiratory gating", European Radiology. 2015 Apr;[Epub ahead of print]. doi: 10.1007/s00330-015-3797-x

Abstract

Objectives: To evaluate the efficiency of automatic respiratory gating (ARG) in reducing respiratory motion-induced artefacts from dynamic contrast-enhanced ultrasound (DCEUS) acquisitions and to assess the impact of ARG on DCEUS quantification parameters in patients with liver malignancies.

Methods: Twenty-five patients with liver metastasis were imaged with DCEUS. The lognormal indicator dilution model was fitted on time-intensity curves extracted from hepatic lesions with and without the use of ARG and DCEUS quantification parameters were extracted. The goodness of fit was assessed using the coefficient of determination (R^2_{LN}).

The effect respiration had on the data was assessed using the respiration amplitude (*RA*) metric. Pearson's correlation coefficient (*r*) was used to assess the correlation between R^2_{LN} and *RA* with and without the use of ARG.

Results: The *RA* parameter was strongly correlated with R^2_{LN} (r =-0.96, P=7.412x10^{-15}) and this correlation became weaker with ARG (r =-0.64, P=5.449x10^{-4}). ARG significantly influenced the values of the quantification parameters extracted (P≤0.05). The *RA* was significantly decreased when ARG was used (P=1.172x10^{-6}).

Conclusions: ARG has a significant impact on the quantification parameters extracted and it has been shown to improve the accuracy of liver lesion DCEUS.

Keywords: Contrast Agents; Respiration; Liver Metastases; Ultrasound Imaging; Microbubbles

Key Points:

• ARG has a significant impact on DCEUS quantification parameters

• ARG can improve the modelling of liver lesion hemodynamics using DCEUS quantification

• ARG significantly reduces the respiration amplitude of DCEUS lesion time-intensity curves

3.1 Introduction

Studies have shown that dynamic contrast-enhanced ultrasound (DCEUS) can be used for early evaluation of response to anti-angiogenic treatment of patient with liver and renal cancers [1]–[4]. Indicator dilution theory can be used to model lesion hemodynamics and extract blood flow parameters [5]. The DCEUS quantification parameters relating to lesion perfusion may provide for an early detection of patient response to treatment [6],

[7]. Various factors can affect the image intensity in DCEUS loops such as signal saturation , acoustic shadowing, nonlinear propagation of ultrasound , beam non-uniformity, ultrasound probe motion and system settings [8]–[10].

Respiratory motion is a major limitation in the accurate measurement of the time-intensity curve parameters, especially in liver imaging by it introducing noise in the curves. Typically, a region-of-interest (ROI) is drawn around the lesion and the average pixel intensity is measured as a function of time forming the time-intensity curve of the lesion. Respiration causes the lesion to move in and out of the ROI, thus the image intensity within the ROI may also have components arising from sampling of normal tissue and/or vessels (Figure 3-1) that shows as added noise in the data (Figure 3-3a).

Respiratory gating algorithms have been suggested in literature as a possible solution to limiting the effect of breathing motion [11]–[14]. Here we evaluated an algorithm for automatic respiratory gating (ARG) in a clinical study for efficiency in reducing the effect of respiratory motion from DCEUS loops [15]. The impact ARG has on the various DCEUS quantification parameters that relate to blood flow is also assessed.

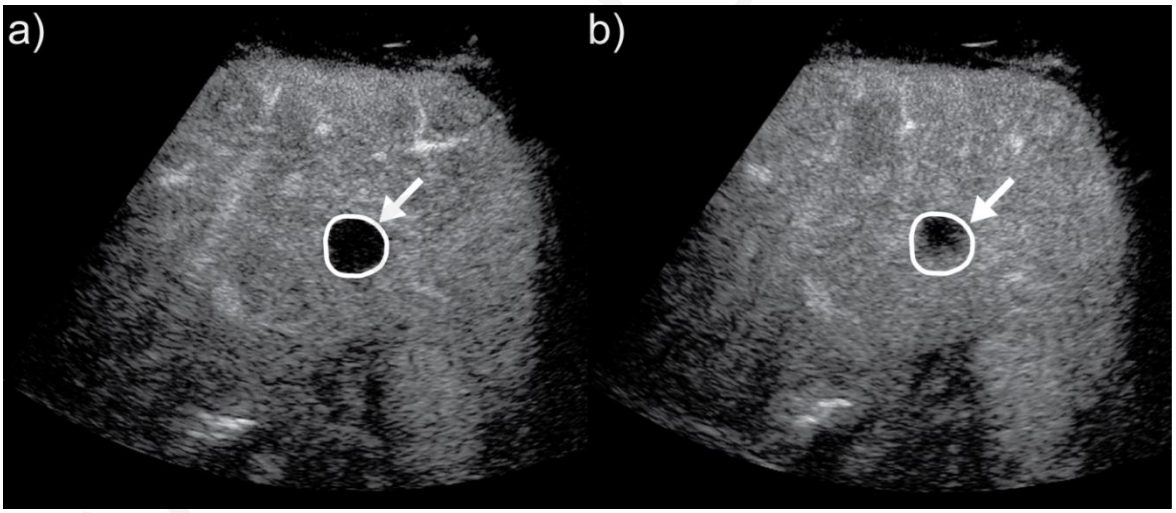

Figure 3-1: Demonstration of a lesion moving a) inside and b) outside a region-of-interest (ROI) (indicated by the arrow) at two different time points of the DCEUS acquisition. In a) the mean intensity value within the ROI is representative of the lesion perfusion whereas in b) the ROI also includes part of the liver parenchyma, and thus the mean linear intensity value extracted is not representative of lesion perfusion.

3.2 Materials and methods

3.2.1 Patients

Twenty five patients (11 females, 14 males) presenting with colorectal liver metastases were imaged. The overall mean age of the patients was 69 years (range, 47-77), with a male population age mean of 71 (range, 59-77) and a female population mean age of 67 (range, 47-72). The patients imaged received a bi-weekly dose of bevacizumab

(Avastin; Hoffmann-La Roche, Basel, Switzerland) along with a chemotherapeutic regiment of oxaliplatin (Eloxatin; Sanofi-Aventis, Paris, France) or irinotecan (Camptosar; Pfizer, New York, NY, USA) combined with capecitabine (XELODA; Hoffmann-La Roche, Basel, Switzerland). DCEUS image loops were obtained from each patient for further analysis.

Ethical approval for this study was provided from the institutional review board of our hospital. The nature of the procedure was fully explained to all patients and informed consent was obtained.

3.2.2 Clinical dynamic contrast-enhanced ultrasound (DCEUS) acquisitions

The Philips iU22 scanner (Philips Medical Systems, Bothell, WA, USA) along with the C5-1 curved array probe was utilized for all imaging. System settings were: imaging frequency of 1.7 MHz, power modulation pulsing scheme with a mechanical index (MI) of 0.06, and frame rate between 7 and 10 Hz, depending on the image depth. One-minute loops of lesions were acquired in dual-contrast imaging acquisition mode. A very low-level uniform noise in the image before the arrival of the microbubbles was allowed to ensure that the time-gain-compensation (TGC) was exactly at the threshold of detection. The focus was set a little below the depth of the lesion for a uniform pressure field. A 2.4-mL bolus of microbubble contrast agent Sonovue (Bracco s.p.a., Milan, Italy) was injected via a three-way valve. A constant imaging plane was maintained by the clinician by monitoring the "tissue" side of the acquisition.

The lesions presented in this study varied in their size, depth, initial vascularity and location. The diameter of the lesions varied between 7.7 and 62.6 mm with a median diameter of 16.8mm whilst the median depth of the lesions was 5.1 cm with a minimum of 2.55 cm and a maximum of 8.56 cm. Eleven lesions had a hypervascular perfusion pattern, 13 exhibited hypervascular perfusion with hypovascular cores and one lesion displayed hypovascular perfusion with hypervascular ring enhancement on its periphery. One-third of the lesions presented where located in the right lobe of the liver. In addition, seven patients had more than one lesion present in their acquisitions. In these cases the largest lesion was chosen for analysis except for one patient in which the largest lesion was confounded by shadowing artefacts, and so the second largest lesion was chosen.

The patients received no breathing instructions during the DCEUS acquisitions. This was done in order to evaluate the ARG algorithm under various magnitudes of in-plane and out-of-plane respiratory motion induced naturally by the variability in the breathing patterns of the patient population.

3.2.3 Image data analysis

The commercial quantification software QLAB version 8.1 (Philips Medical Systems) was used to analyze the image loops. A radiologist with over 20 years of experience used both the arterial and late portal phases of the DCEUS loop to accurately draw a ROI around the liver lesion. The specific frame on which the ROI was drawn will be referred to as the "trigger" frame. Time-intensity curves from linearized [16] image data were extracted from QLAB without the use of ARG.

Subsequently, the tissue side loop of each acquisition was imported into MATLAB (2012b, The MathWorks Inc., Natick, MA, USA) in order to implement the ARG algorithm (Figure 3-2). Analysis of the image data was performed by a Biomedical Engineering PhD candidate supervised by a professor of bioengineering with more than 20 years of experience in clinical ultrasound research. The frame subtraction technique [17] was utilized to detect the location and intensity of motion throughout the acquisition. Bright moving structures were identified on the trigger frame and the motion intensity corresponding to the position of each structure was recorded. In addition, the content of respiration for the motion associated with each structure was quantified using frequency domain analysis. The structure with the highest degree of respiratory motion was used to construct a ROI on the tissue loop and extract the time-intensity curve. The peaks of the time-intensity curve correspond to the time instances at which the bright moving structure is at the same position as on the trigger frame. Frames that were below 40% from the peak intensity were rejected as being out of phase with the trigger frame. The threshold value of 40% was chosen as a good default value preserving enough data points to perform a reliable fit of the lognormal model onto the lesion time-intensity curve and reducing respiratory motion in the DCEUS acquisitions. The intensity data on the lesion time-intensity curve matching the rejected frames were removed. Thus after the implementation of the ARG algorithm the lesion time-intensity curve data were in phase with the trigger frame (Figure 3-3a). Details regarding the implementation of the ARG algorithm can be found in the literature [15].

The lognormal indicator dilution model [5] was fitted on to time-intensity curves extracted from lesions with and without the use of ARG. The most common DCEUS quantification parameters [1], [3], [4], [6] are the area under the curve (AUC), the peak intensity (PI), the rise time (RT) and the mean transit time (MTT). The coefficient of determination of the fit of the lognormal model to the data (R^2_{LN}) was calculated. The R^2_{LN} was used in order to assess whether the ARG procedure improves the quality of the

lognormal model fit on to the time-intensity curves, thus improving the reliability of the quantification parameters extracted. The assumption that the quality of the fit of the model to the data improves reliability of DCEUS quantification was suggested in the literature [13], [14].

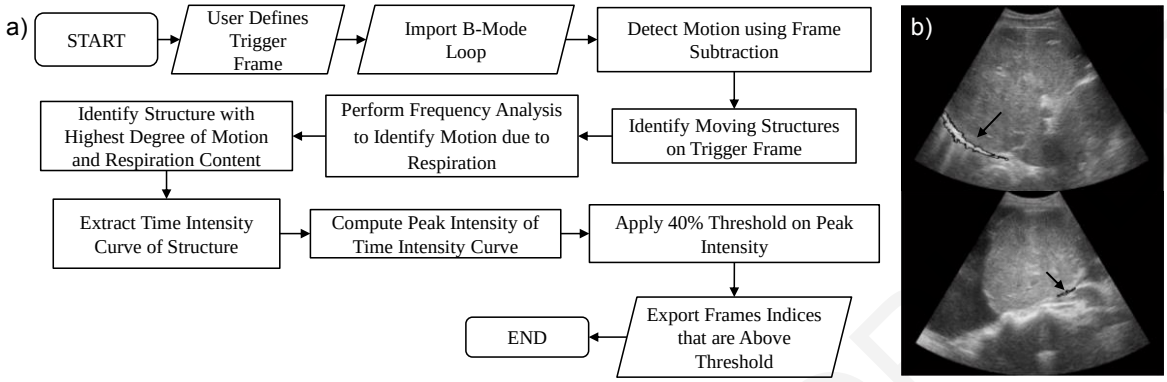

Figure 3-2: a) Flowchart of the procedures used for the implementation of the automatic respiratory gating (ARG) algorithm. b) Examples of moving structures identified by the ARG algorithm on the trigger frame of the "tissue" side of the dual contrast imaging acquisition (indicated by the arrows).

Another useful parameter that was extracted from the time-intensity curves was the respiration amplitude (*RA*). *RA* quantifies how much respiration affects a time-intensity curve and it was calculated using the frequency spectrum of the time-intensity curves extracted with and without the use of ARG. Any significant reduction in the *RA* with the use of ARG would demonstrate that there is a decrease on the effect of respiration on the lesion time-intensity curve. The *RA* was calculated based on the fact that the perfusion pattern of the liver lesion changes more slowly compared to components from respiration that vary within a frequency range between 0.1 and 0.5 Hz [18]. The *RA* was calculated by calculating the area under the frequency spectrum between 0.1 and 0.5 Hz and dividing by the area between 0 to 0.1 Hz (Figure 3-3b).

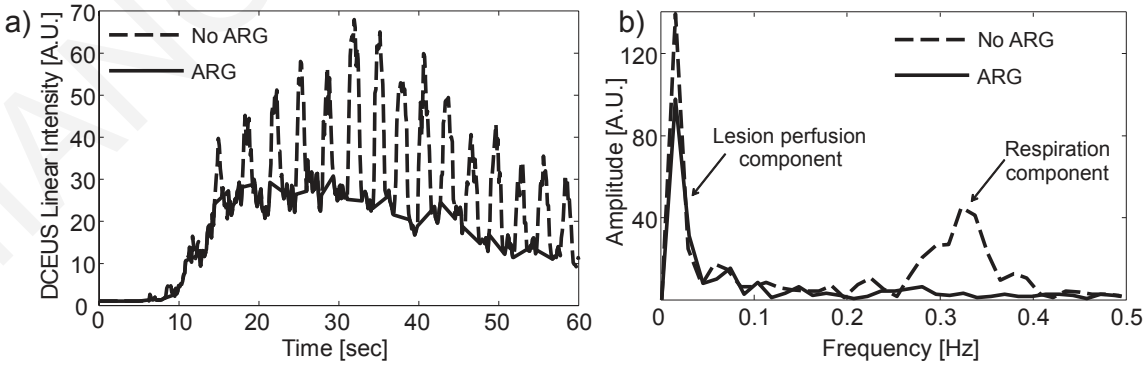

Figure 3-3: a) Example of DCEUS time-intensity curve extracted from a region-of-interest (ROI) encompassing a lesion with and without the use of automatic respiratory gating (ARG). b) Frequency spectrum of a lesion's time-intensity curve with and without the use of ARG. The slow changing intensity signal originates from the perfusion of the lesion and it lies below 0.1 Hz. The respiratory component lies at 0.1-0.5 Hz. By dividing the area under the curve between the respiration range of 0.1-0.5 Hz over the lesion perfusion range of 0-0.1 Hz the respiration amplitude (RA) was calculated.

3.2.4 Statistical analysis

For each quantification parameter examined in this study, the distribution before and after ARG was summarized in boxplots indicating the median, first and third quartiles. An outlier was considered as a value that was greater than the third quartile plus 1.5 times the interquartile range (IQR, first – third quartiles) or less than the first quartile minus 1.5 times the IQR. The boxplot bottom whisker was calculated as the minimum value that was not an outlier and the top whisker as the maximum value not considered an outlier.

In order to assess whether ARG has any effect on DCEUS quantification, Wilcoxon signed rank tests were performed between quantification parameters extracted with and without ARG for all the patients participating in the study(N=25). Additionally the Wilcoxon signed rank tests were repeated on quantification parameters extracted from lesion time-intensity curves that had an RA of less than 1.5(N=12). This was done in order to establish the impact of ARG in cases where there was not too much respiration motion present. P-values calculated from the Wilcoxon signed rank test that were less than 0.05 were considered to indicate a significant difference. Statistical analyses were performed using MATLAB's Statistical Toolbox. The power of the Wilcoxon signed rank test performed was assessed using Monte Carlo simulation. The Monte Carlo simulation was performed in MATLAB and a description of the procedure can be found in the Appendix.

The reduction in the *RA* calculated from lesion time-intensity curves extracted without and with the use of ARG was assessed using a paired t-test. The t-test was chosen because the difference in the distribution of the *RA* data with and without ARG allows for the calculation of power analytically. The significance level for the t-test was set at a p-value of 0.05. The correlation between the quality-of-fit (R^2_{LN}) and the *RA* was assessed using the Pearson's *r*.

3.3 Results

3.3.1 Relationship between quality of fit and respiration amplitude

Pearson's *r* between the effect of respiration (*RA*) and the quality-of-fit (R^2_{LN}) when ARG was not used had a value of -0.96 ($P=7.412\text{x}10^{-15}$). This strong linear correlation between the *RA* and the quality of fit demonstrated the decline of the accuracy in the modelling of lesion perfusion as the magnitude of respiration increases. When the ARG algorithm was used Pearson's *r* was calculated to be -0.64 ($P=5.449\text{x}10^{-4}$). The 33% decrease in the correlation between *RA* and R^2_{LN} shows the improvement that ARG can have in the modelling of the haemodynamics of liver lesions using DCEUS quantification

across the whole range of *RA*. Furthermore with the use of ARG the R^2_{LN} (the quality of fit of the lognormal model onto the lesion time-intensity curves) was almost constant as *RA* increased. The slope of the linear regression line had a value of -0.11 with the use of ARG compared to -0.31 without ARG. More specifically without the use of ARG 17/25 patients exhibited an R^2_{LN} of less than 0.8; this number decreased to 3/25 patients with the use of ARG (Figure 3-4).

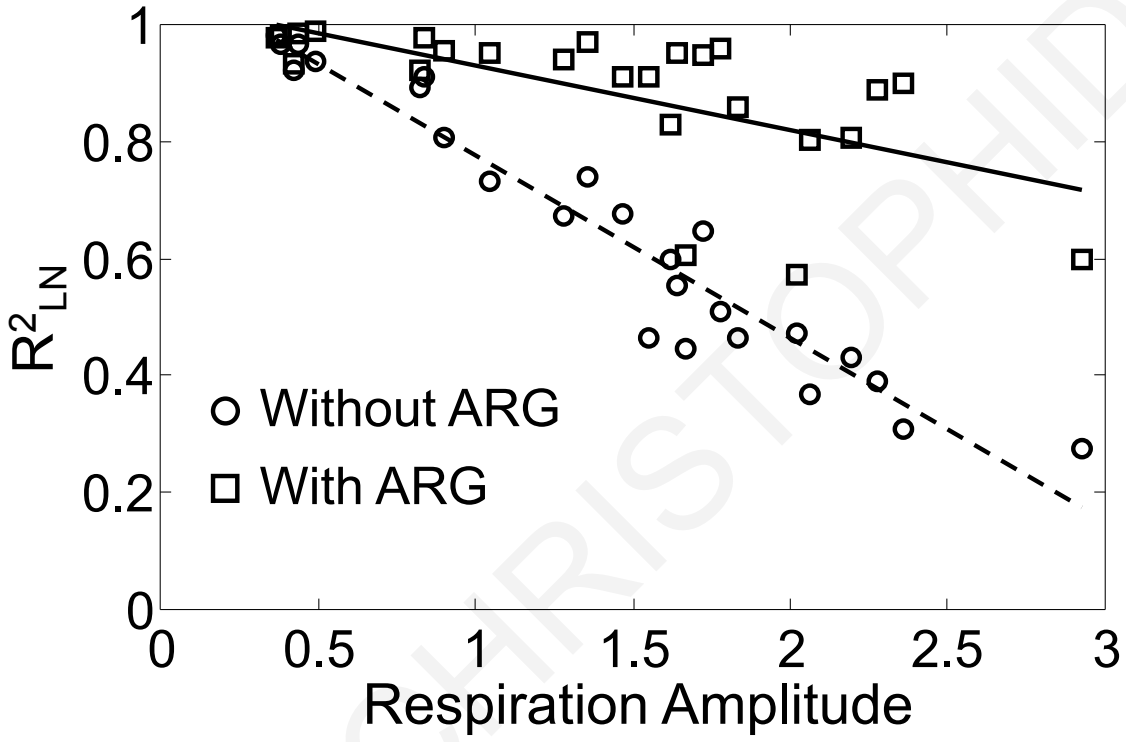

Figure 3-4: R^2_{LN} of DCEUS time-intensity curve data fit on lognormal model vs. respiration amplitude with and without the use of automatic respiratory gating (ARG). The linear regression lines of the displayed data are also shown without (dotted) and with (solid) ARG.

3.3.2 Impact of ARG on quantification parameters

Boxplots of the distribution of DCEUS quantification parameters with and without the use of ARG for the group of all patients (N=25) are presented in Figure 3-5. Significant differences between RT, AUC and PI with and without the use of ARG were found ($P<0.05$). No significant difference was found between using ARG and not using it for the MTT ($P=0.904$). The power of the Wilcoxon singed rank tests was assessed for each parameter and for a sample size of 25 it was calculated to be 0.75 for the RT (standard deviation, 0.03), 0.07 for the MTT (standard deviation, 0.01), 0.95 for the AUC (standard deviation, 0.01) and 0.87 for the PI (standard deviation, 0.02).

Distribution of the values of the quantification parameters with and without the use of ARG was similar, with the IQR of the boxplots overlapping extensively (Figure 3-5). For patients with $RA < 1.5$ ARG did not have a significant impact on any quantification

parameter (P>0.077). This suggests that the use of ARG in cases where there is not too much respiration motion does not affect the quantification data in any way.

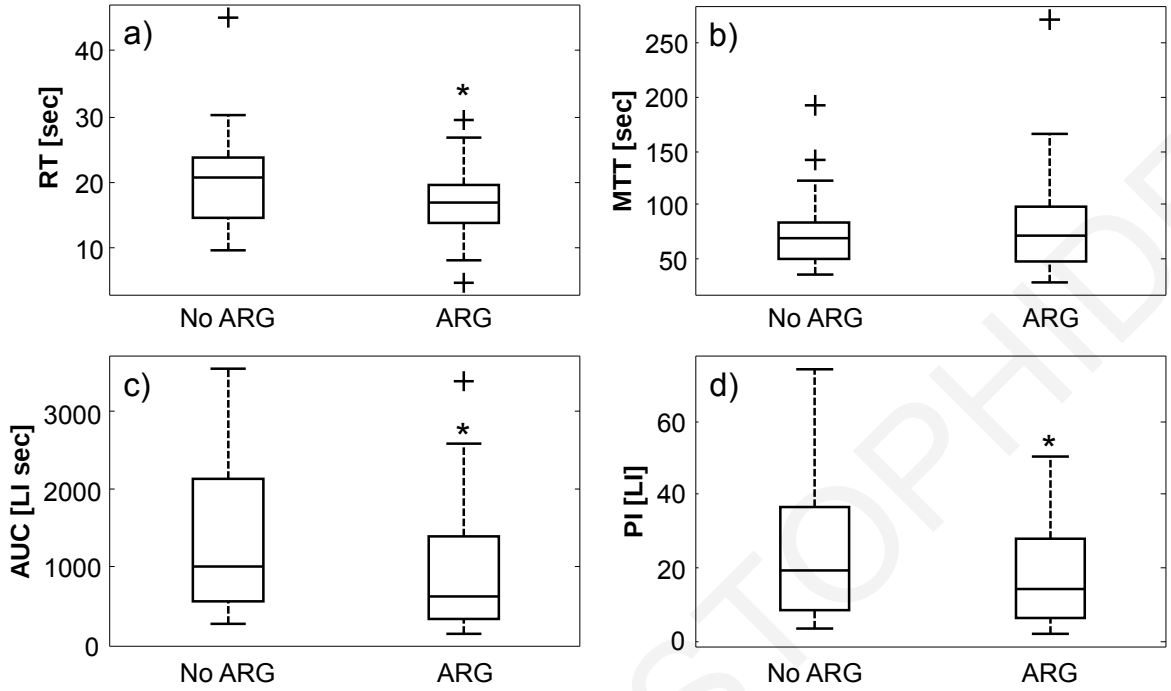

Figure 3-5: Boxplots of distributions of a) rise time (RT), b) mean transit time (MTT), c) area under the curve (AUC) and d) peak intensity (PI) quantification parameters with and without the use of automatic respiratory gating (ARG) for all the patients (N=25) participating in the study. *LI* linear intensity. $^{+}$outliers, *P≤0.05.

3.3.3 Reduction of *RA* with the use of ARG

The *RA* calculated from lesion time-intensity curves extracted without the use of ARG was compared to the *RA* calculated with the use of ARG (Figure 3-6). The *RA* was reduced significantly when ARG was used (P≤0.05).

3.4 Discussion

From the results of the statistical analysis on the whole patient population it has been demonstrated that ARG can have a significant impact on the RT, AUC and PI. No statistically significant impact on MTT could be shown. In patients that have an *RA* of less than 1.5 ARG has no impact on any quantification parameters. Grouls et al. [19] also investigated the effect of respiratory gating on DCEUS quantification parameters using a semi-automatic gating implementation of the manual technique introduced by Averkiou et al. [1]. Grouls et al. [19] showed that gating can have a significant effect on the AUC of bolus injection DCEUS and on the calculation of the retention of targeted microbubbles for molecular ultrasound imaging.

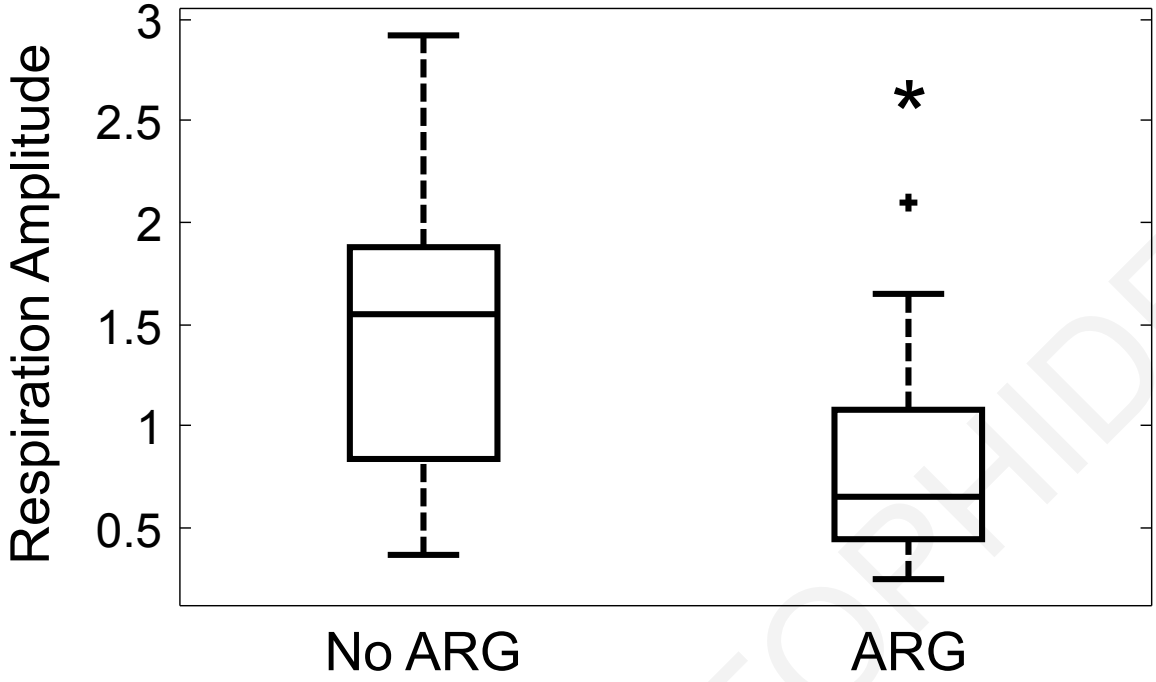

Figure 3-6: Boxplots of the distribution of respiration amplitude (RA) with and without the use of automatic respiratory gating (ARG). $^{+}$outliers, *P≤0.05, Power>0.9.

A strong correlation has been demonstrated between R^2_{LN} and *RA*, with the increase in *RA* explaining to a large extent the decline in R^2_{LN} of non-ARG processed clinical DCEUS lesion time-intensity curves. This demonstrates that respiration can have a large impact on DCEUS quantification parameters. ARG increases the quality of fit of the time-intensity curve data on to the lognormal model examined in this study across the range of *RA* values, and thus increases the accuracy of the extracted quantification parameters.

The mean increase in R^2_{LN} across the patient population expressed as a percentage is 37. In the literature 15% and 11% increases in the quality of fit were reported by Rognin et al. [13] in the application of motion correction on the parametric imaging of DCEUS of the kidney and liver, respectively. A mean increase between the quality of fit factor before and after motion correction of 15% was reported by Zhang et al. [14] for the parametric imaging of ten liver DCEUS loops. The above two studies [13], [14] involve the technique of parametric imaging and report the quality of fit on a pixel-to-pixel basis. The presence of noise on data sampled from single pixels or groups of pixels is expected to be greater than those of the present work. Thus any comparison of the results of the mentioned studies with the current study needs to take into account the detrimental effect that the increased noise will have on the quality of fit reported. Furthermore, these studies did not quantify the presence of respiration in their data thus making any comparisons with the current study even more complicated.

In addition to the increase in the R^2_{LN} with the use of ARG, the *RA* was also decreased significantly in time-intensity curves of lesions. This reduction in the RA with the use of ARG further demonstrates the effectiveness of the ARG algorithm in removing respiratory motion from lesion time-intensity curves and increasing the accuracy of DCEUS quantification. By increasing the accuracy of in-vivo DCEUS quantification parameters the clinician can perform a more accurate diagnosis, e.g. on the response of the patient to treatment. Accurate tumour microflow measurements may lead to a decision to be made in regards to continuing with the current treatment or altering the treatment, which can result in a better clinical outcome or a reduction in expenditure on ineffective treatments.

Although this study evaluates the use of ARG on DCEUS quantification, qualitative evaluation of image loops [20] may also benefit from such a motion-correction technique. By applying ARG on image loops during review, the removal of out-of-plane motion results in a more accurate depiction of the area. For example, small lesion vessels stay in-plane and show their feeding patterns.

Other post-processing procedures for treating respiratory motion on DCEUS loops of liver lesions can be found in the literature. One technique proposed by Averkiou et al. [1] is for the clinician to manually reject frames in which the diaphragm position deviates from a reference location. This technique does not require any special precautions to be taken during the DCEUS acquisition but it is time consuming and operator dependent. The present ARG algorithm works by detecting bright structures moving with a frequency within the range of respiration (0.1-0.5Hz). Often such a bright structure is the diaphragm but others may be encountered also. In 17/25 cases analyzed the diaphragm was automatically detected. In the rest other bright image structures were detected (Figure 3-2b).

Studies on methods for automatic respiratory motion correction have been published in the literature [11]–[14], [21]. A technique based on independent component analysis (ICA) was introduced by Renault et al. [12] where the respiratory kinetics curve could be manually extracted from the components derived from the ICA. Frames of the loop that were part of the end phases of the respiratory cycle could be isolated by using a threshold on the respiratory kinetics curve. Furthermore, Mule et al. [11] developed a fully automatic algorithm that utilizes principal component analysis (PCA) to perform respiratory gating and extract frames that belong to the end phases of the respiratory cycle. Although the ICA and PCA algorithms proposed can correct for both in-plane and out-of-plane respiratory

motion, they are limited in extracting only the end phases of the respiratory cycle. It is possible that part of the lesion, or even the whole lesion, could be absent on the imaging plane during the end-respiratory phases.

Image registration has also been used in the literature to correct for respiratory motion. Zhang et al. [14] used a 2D image registration technique with frame selection in order to remove both in-plane and out-of-plane motion but a computational time of 3 min per 100 frames could limit the use of the algorithm in the clinic. Rognin et al. [13], [21] used a 2D rigid registration technique with translation and rotation to register frames with a reference frame; however, this technique lacked a scheme for removing out-of-plane respiratory motion. Both the image registration algorithms discussed required the user to draw ROI(s) on frames to define the area on the image into which the registration process would take place.

The ARG algorithm clinically evaluated in the present study is fully automated requiring the user to only provide a reference frame; it is fast since it can process 100 frames in less than a second, it allows for the extraction of any breathing cycle phase required by the operator, and it removes both in-plane and out-of-plane respiratory motion [15], [22].

A limitation of the present work is the use of a fixed gating threshold for all of the patients. The gating threshold regulates what percentage of frames that are out of synchronization with the trigger frame are allowed to be part of the ARG processed loop. By setting the gating threshold too high a large number of frames that are out of phase with the trigger are quantified leading to uncertainty in the results. If the gating threshold is low it includes a very small number of frames to be quantified and possibly too few to be able to perform a robust fit of the model. Since the breathing patterns of patients can differ significantly, the clinician performing the quantification analysis can easily adjust the threshold for each patient during quantification of the loops. A 40% threshold was used on all patients to standardize the procedure as was previously reported in the literature [15].

Moreover it is possible to manually reject frames of the ARG processed loop to further improve the quantification analysis. This option was not used in this study in order to ensure reproducibility and objectivity. Some quantification software offer the ability to perform motion compensation based on image registration algorithms. Since this work focused on evaluating a specific ARG technique, no further motion compensation was performed on the extracted data. In clinical practice, conventional motion compensation

algorithms may be applied to ARG processed loops and further improve the quantification accuracy.

In conclusion, the ARG algorithm examined had a strong impact on clinical DCEUS quantification parameters. Furthermore, the use of ARG resulted in an overall increase in the quality of fit of the lognormal model and a significant decrease in the respiration amplitude. This study demonstrates the implications that respiration can have on liver DCEUS; the same technique may also be applied to study the impact of respiration on DCEUS when studying the perfusion of other organs, but further validation studies are necessary.

Acknowledgements The scientific guarantor of this publication Prof. Michalakis Averkiou, University of Cyprus. The authors of this manuscript declare no relationships with any companies whose products or services may be related to the subject matter of the article. The authors state that this work has not received any funding. No complex statistical methods were necessary for this paper. Institutional Review Board approval was obtained. Written informed consent was obtained from all subjects (patients) in this study. Methodology: retrospective, experimental, performed at one institution.

Appendix: Calculation of the power of the Wilcoxon signed rank tests

Some assumptions must be made in order to calculate the power of the Wilcoxon signed rank tests performed in this study. The first assumption was that the parameters from before and after the application of ARG were part of the same distribution. Two-sample Kolmogorov-Smirnov tests were performed on the quantification parameters before and after the application of ARG demonstrating that the parameters were part of the same distribution ($P>0.05$). The Monte Carlo simulation made use of this by concatenating the before and after ARG parameters into one population from which the mean and standard deviation were calculated.

Another assumption made in order to calculate the power was that the concatenated distributions of the quantification parameters along with the differences between the parameters before and after the application of ARG were normal. This was demonstrated using one-sample Kolmogorov-Smirnov tests at a significance level of 0.05. This assumption was used in the Monte Carlo simulation in order to simulate random samples from normal distributions.

The Monte Carlo simulation for a particular pair of quantification parameters extracted without ARG (A) and with ARG (B) is described in the following steps:

Step 1: Calculate mean (μ_{noARG}) and standard deviation (σ_{noARG}) of the concatenated vector of A and B.

Step 2: Calculate mean (μ_{diff}) and standard deviation (σ_{diff}) of the differences (A minus B).

Step 3: Set the sample size equal to 25 (n=25).

Step 4: Simulate quantification parameters extracted without ARG by randomly sampling 25 data points (n=25) from a normal distribution with a mean equal to μ_{noARG} and a standard deviation equal to σ_{noARG}.

Step 5: Simulate differences between quantification parameters extracted with and without ARG by randomly sampling (n=25) from a normal distribution with a mean equal to μ_{diff} and a standard deviation equal to σ_{diff}.

Step 6: Simulate quantification parameters extracted with ARG by subtracting the random sample of step 4 from that of step 5.

Step 7: Perform a Wilcoxon signed rank test between the simulated parameters extracted with and without the use of ARG at a significance level of 0.05.

Step 8: Increment counter variable (CV) by one if the test returns a significant difference between the simulated parameters extracted with and without the use of ARG.

Step 9: Repeat steps 4-8 200 times.

Step 10: Calculate power by dividing CV over 200.

Step 11: Repeat steps 4-10 20 times to calculate the uncertainty of the power calculation.

References

[1] M. Averkiou, M. Lampaskis, K. Kyriakopoulou, D. Skarlos, G. Klouvas, C. Strouthos, and E. Leen, "Quantification of tumor microvascularity with respiratory gated contrast enhanced ultrasound for monitoring therapy.," *Ultrasound Med Biol*, vol. 36, no. 1, pp. 68–77, Jan. 2010.

[2] M. Bertolotto, G. Pozzato, L. S. Crocè, F. Nascimben, C. Gasparini, M. A. Cova, and C. Tiribelli, "Blood flow changes in hepatocellular carcinoma after the administration of thalidomide assessed by reperfusion kinetics during microbubble infusion: preliminary results.," *Invest Radiol*, vol. 41, no. 1, pp. 15–21, Jan. 2006.

[3] N. Lassau, S. Koscielny, L. Chami, M. Chebil, B. Benatsou, A. Roche, M. Ducreux, D. Malka, and V. Boige, "Advanced hepatocellular carcinoma: early evaluation of response to bevacizumab therapy at dynamic contrast-enhanced US with quantification--preliminary results.," *Radiology*, vol. 258, no. 1, pp. 291–300, Jan. 2011.

[4] N. Lassau, S. Koscielny, L. Albiges, L. Chami, B. Benatsou, M. Chebil, A. Roche, and B. J. Escudier, "Metastatic renal cell carcinoma treated with sunitinib: early evaluation of treatment response using dynamic contrast-enhanced ultrasonography.," *Clin Cancer Res*, vol. 16, no. 4, pp. 1216–25, Feb. 2010.

[5] C. Strouthos, M. Lampaskis, V. Sboros, A. McNeilly, and M. Averkiou, "Indicator dilution models for the quantification of microvascular blood flow with bolus administration of ultrasound contrast agents.," *IEEE Trans Ultrason Ferroelectr Freq Control*, vol. 57, no. 6, pp. 1296–310, Jun. 2010.

[6] C. F. Dietrich, M. A. Averkiou, J.-M. Correas, N. Lassau, E. Leen, and F. Piscaglia, "An EFSUMB introduction into Dynamic Contrast-Enhanced Ultrasound (DCE-US) for quantification of tumour perfusion.," *Ultraschall Med*, vol. 33, no. 4, pp. 344–51, Aug. 2012.

[7] E. Leen, M. Averkiou, M. Arditi, P. Burns, D. Bokor, T. Gauthier, Y. Kono, and O. Lucidarme, "Dynamic contrast enhanced ultrasound assessment of the vascular effects of novel therapeutics in early stage trials.," *Eur Radiol*, vol. 22, no. 7, pp. 1442–50, Jul. 2012.

[8] M.-X. Tang, H. Mulvana, T. Gauthier, A. K. P. Lim, D. O. Cosgrove, R. J. Eckersley, and E. Stride, "Quantitative contrast-enhanced ultrasound imaging: a review of sources of variability.," *Interface Focus*, vol. 1, no. 4, pp. 520–39, Aug. 2011.

[9] M. Lampaskis and M. Averkiou, "Investigation of the relationship of nonlinear backscattered ultrasound intensity with microbubble concentration at low MI.," *Ultrasound Med Biol*, vol. 36, no. 2, pp. 306–12, Mar. 2010.

[10] A. Thapar, J. Shalhoub, M. Averkiou, C. Mannaris, A. H. Davies, and E. L. S. Leen, "Dose-dependent artifact in the far wall of the carotid artery at dynamic contrast-enhanced US.," *Radiology*, vol. 262, no. 2, pp. 672–9, Feb. 2012.

[11] S. Mulé, N. Kachenoura, O. Lucidarme, A. De Oliveira, C. Pellot-Barakat, A. Herment, and F. Frouin, "An automatic respiratory gating method for the improvement of microcirculation evaluation: application to contrast-enhanced ultrasound studies of focal liver lesions.," *Phys Med Biol*, vol. 56, no. 16, pp. 5153–65, Aug. 2011.

[12] G. Renault, F. Tranquart, V. Perlbarg, A. Bleuzen, A. Herment, and F. Frouin, "A posteriori respiratory gating in contrast ultrasound for assessment of hepatic perfusion.," *Phys Med Biol*, vol. 50, no. 19, pp. 4465–80, Oct. 2005.

[13] N. Rognin, R. Campos, J. Thiran, T. Messager, P. Broillet, P. Frinking, M. Mercier, and M. Arditi, "A new approach for automatic motion compensation for improved estimation of perfusion quantification parameters in ultrasound imaging," in *Proceedings of the 8th French Conference on Acoustics*, 2006, pp. 61–65.

[14] J. Zhang, M. Ding, F. Meng, M. Yuchi, and X. Zhang, "Respiratory motion correction in free-breathing ultrasound image sequence for quantification of hepatic perfusion," *Med Phys*, vol. 38, no. 8, pp. 4737–4748, Aug. 2011.

[15] D. Christofides, E. Leen, and M. Averkiou, "Automatic respiratory gating for contrast ultrasound evaluation of liver lesions.," *IEEE Trans. Ultrason. Ferroelectr. Freq. Control*, vol. 61, no. 1, pp. 25–32, Jan. 2014.

[16] T. P. Gauthier, M. A. Averkiou, and E. L. S. Leen, "Perfusion quantification using dynamic contrast-enhanced ultrasound: the impact of dynamic range and gain on time-intensity curves.," *Ultrasonics*, vol. 51, no. 1, pp. 102–6, Jan. 2011.

[17] A. Jain, *Fundamentals of Digital Image Processing*. Englewood Cliffs, NJ: Prentice-Hall, 1989.

[18] S. Fleming, M. Thompson, R. Stevens, C. Heneghan, A. Plüddemann, I. Maconochie, L. Tarassenko, and D. Mant, "Normal ranges of heart rate and respiratory rate in children from birth to 18 years of age: a systematic review of observational studies.," *Lancet*, vol. 377, no. 9770, pp. 1011–8, Mar. 2011.

[19] C. Grouls, M. Hatting, I. Tardy, J. Bzyl, G. Mühlenbruch, F. F. Behrendt, T. Penzkofer, C. Trautwein, C. Kuhl, F. Kiessling, and M. Palmowski, "Development and validation of an intrinsic landmark-based gating protocol applicable for functional and molecular ultrasound imaging.," *Eur. Radiol.*, vol. 22, no. 8, pp. 1789–96, Aug. 2012.

[20] V. Roche, F. Pigneur, L. Tselikas, M. Roux, L. Baranes, M. Djabbari, C. Costentin, J. Calderaro, A. Laurent, A. Rahmouni, and A. Luciani, "Differentiation of focal nodular hyperplasia from hepatocellular adenomas with low-mechanical-index contrast-enhanced sonography (CEUS): effect of size on diagnostic confidence.," *Eur. Radiol.*, vol. 25, no. 1, pp. 186–95, Jan. 2015.

[21] N. G. Rognin, M. Arditi, L. Mercier, P. J. A. Frinking, M. Schneider, G. Perrenoud, A. Anaye, J.-Y. Meuwly, and F. Tranquart, "Parametric imaging for characterizing focal liver lesions in contrast-enhanced ultrasound.," *IEEE Trans Ultrason Ferroelectr Freq Control*, vol. 57, no. 11, pp. 2503–11, Nov. 2010.

[22] D. Christofides, E. Leen, and M. Averkiou, “Improvement of accuracy of liver lesion DCEUS quantification using automatic respiratory gating,” in *19th European Symposium on Ultrasound Contrast Imaging*, 2014, pp. 69–73.

4

Evaluation of ARG using a respiratory motion simulation model

Submitted for review; by Damianos Christofides, Edward Leen and Michalakis Averkiou, "Evaluation of the accuracy of liver lesion DCEUS quantification with respiratory gating", IEEE Transactions on Medical Imaging. 2015 Sep

Abstract

Confidence in the accuracy of dynamic contrast enhanced ultrasound (DCEUS) quantification parameters is imperative for the correct diagnosis of liver lesion perfusion characteristics. An important source of uncertainty in liver DCEUS acquisitions is artifacts introduced by respiratory motion. The objective of this study is to construct a respiratory motion simulation model (RMSM) of dual contrast imaging mode acquisitions of liver lesions in order to evaluate an algorithm for automatic respiratory gating (ARG). The respiratory kinetics as well as the perfusion models of the liver lesion and parenchyma used by the RMSM were solely derived from clinical data. The quality of fit (of the DCEUS data onto the bolus kinetics model) depends on the respiration amplitude. Similar trends in terms of quality of fit as a function of respiration amplitude were observed from RMSM and clinical data. The errors introduced on the DCEUS quantification under the influence of respiration were evaluated. The RMSM revealed that the error in the liver lesion DCEUS quantification parameters significantly decreased($p<0.001$) from a maximum of 32.3% to 6.2% when ARG was used. The use of RMSM clearly demonstrates the capability of the ARG algorithm in significantly reducing errors introduced from both in-plane and out-of-plane respiratory motion.

Index Terms - Medical simulation, Ultrasonic imaging, Contrast agents, Liver metastases, Respiratory gating

4.1 Introduction

In their more than fifteen years of use [1] microbubble contrast agents have been used in many clinical applications. These include the diagnosis of liver lesions [2], the assessment of microvascular damage after a myocardial infarction [3] and the detection of coronary disease [4]. Microbubbles are a pure blood pool contrast agent, because their size is of the same order as red blood cells and thus cannot leave the vascular bed and escape in the interstitium [5], [6]. Their size along with their unique acoustic properties allow for the imaging of perfusion in real time using diagnostic ultrasound.

Microbubbles can be used to perform dynamic contrast enhanced ultrasound (DCEUS) for the characterization of liver lesions[7]. Muhi et al[8] compared the sensitivity of DCEUS, contrast enhanced computed tomography (CECT) and contrast enhanced magnetic resonance imaging (CEMRI) in detecting metastatic liver lesions from patients with primary colorectal cancer. The sensitivity of DCEUS was found to be 73% which compared favorably with the 63% sensitivity of CECT although it was significantly

lower than the 95% sensitivity exhibited by CEMRI. Tranquart et al[9] demonstrated a similar sensitivity of 79.4% for DCEUS in the characterization of 1034 liver lesions as malignant or benign. Furthermore DCEUS is a safe imaging modality since it does not make use of ionizing radiation like CECT and it can be used on patients with pacemakers and ferromagnetic metal implants unlike CEMRI. In addition to its safety and clinical efficiency liver lesion DCEUS is cost effective and it can provide savings of 19% and 52% compared with CECT and CEMRI respectively[9].

Studies have been published in the literature [10]–[12] that use microbubbles to quantify liver lesion perfusion for early evaluation of patient response to treatment. These studies use modeling of the tumor perfusion to extract quantification parameters in order to make the evaluation of the response to treatment more objective than visual assessment and provide an early detection of response [13], [14]. Ideally these quantification parameters would be affected only by the blood flow and volume which in turn are related to the concentration of the microbubbles in the lesion under investigation. This is almost impossible to achieve due to factors that can affect the signal intensity detected by the imaging system like nonlinear propagation of ultrasound [15], signal saturation [16], and stability of ultrasound probe placement.

Further to the DCEUS acquisition problems mentioned there is the problem of physiological motion which can also have a negative impact on the quantification of blood flow and volume. Respiratory motion has the potential to move and deform the anatomy being imaged in relation to the imaging plane being acquired. In quantitative DCEUS for liver lesions the clinician needs to delineate the tumor using a region-of-interest (ROI) in order to extract the signal from within the lesion. However due to respiratory motion, the lesion moves in and out of the ROI. Thus the DCEUS linear intensity signal extracted from within the ROI can also have a component derived from sampling of normal liver parenchyma and/or vessels. Respiration can also obscure visual details in the qualitative assessment of liver lesion DCEUS such as the lesion's feeding vessels since different cross sections of the lesion appear on the imaging plane due to out-of-plane respiratory motion.

A clinically used approach to compensate for the effects of respiratory motion is to direct patients to perform breath-holds [17]. However this approach can only by applied to patients that are able to hold their breath for a substantial period of time. Further to the practical problems breath-holds can also affect hemodynamics [18].

Post-processing procedures can also be implemented to negate the effect of respiratory motion for DCEUS quantification of liver lesions. One technique proposed by

Averkiou et al [10] is for the clinician to manually reject frames in which the diaphragm position deviates from a reference location. This technique does not require any special precautions to be taken during the DCEUS acquisition and although it is implemented after the acquisition it can be very time consuming since all the steps of the procedure are manual.

Automation of correcting for respiratory motion can also be achieved using computational methods [19]–[23]. Disadvantages of these methods include the need for user intervention [20], [21], [23], extraction of only the end-phases of the respiration cycle [19], [20], and speed of execution [23].

A fully automatic respiratory gating (ARG) algorithm has been presented in the literature that is capable of significantly increasing the reliability of DCEUS quantification[24], [25]. The ARG algorithm can typically process 1000 frames in 8 seconds and it can extract any breathing cycle phase required by the user. The only manual intervention needed by the ARG algorithm is that the user chooses a "trigger" frame thus selecting the image (tumor) plane to be analyzed. Even though the ARG algorithm has been shown to increase the quality of fit of the lognormal indicator dilution model[26] onto liver lesion time intensity curves[24] it is impossible to determine the absolute gain in accuracy since it is impossible to know the true lesion perfusion in-vivo. The solution to this obstacle is the use of a simulation of a liver DCEUS acquisition in which the perfusion of the lesion is calculated using an indicator dilution model.

The objective of this work is to evaluate the efficiency of the ARG algorithm[25] in increasing the absolute accuracy of liver lesion DCEUS quantification using the controlled environment of a respiratory motion simulation model (RMSM) of dual contrast imaging mode liver lesion acquisitions.

4.2 Materials and methods

4.2.1 Respiratory Motion Simulation Model

The RMSM was constructed in order to simulate a dual contrast imaging mode acquisition of liver lesions. During clinical acquisitions of liver DCEUS both in-plane and out-of-plane respiratory motion can affect the lesion's shape, size, and location in the image. Furthermore the appearance of structures like the diaphragm is also influenced by respiratory motion and is easily observed on the tissue side of the acquisition (Figure 4-1). These changes in the appearance of the lesion and bright structures (e.g. the diaphragm) induced by respiratory motion were incorporated into the RMSM.

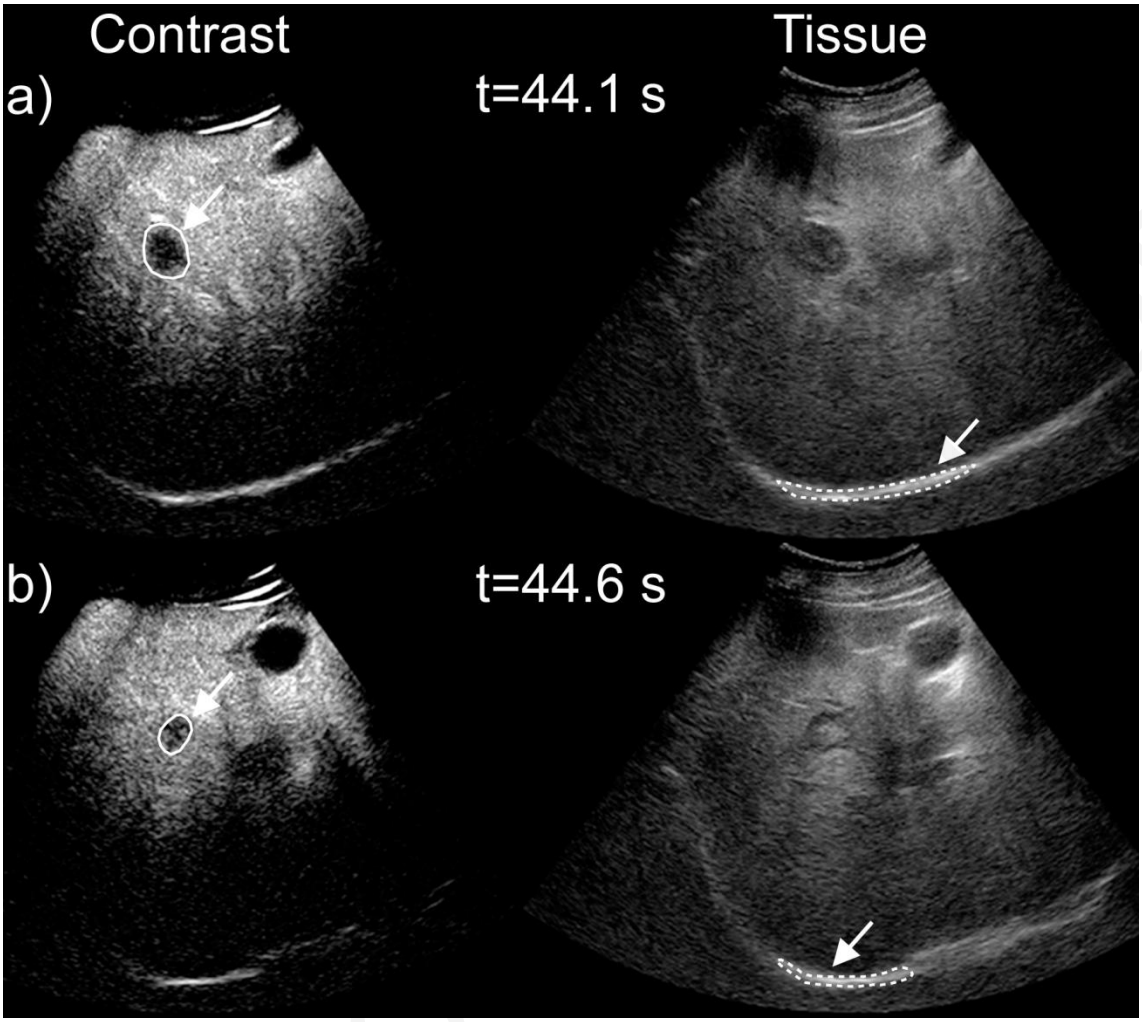

Figure 4-1: Example of a clinical dual contrast imaging mode acquisition showing the contrast side (left) and the tissue side (right) at two time instances from the time of microbubble injection. At 44.1 s from the microbubble bolus injection a) the lesion (solid outline) can be clearly seen on the imaging plane whereas 0.5 s after b) the lesion appears altered in shape, size, and location. The diaphragm (dashed outline) has changed in position and dimensions due to both in-plane and out-of-plane motion.

The RMSM was constructed in MATLAB® (2012b, The MathWorks Inc., Natick, MA) by generating image loops of a spherical lesion imbedded in a liver-like structure in the presence of cyclic respiratory motion. A dual contrast imaging mode was simulated, where the left side displayed the contrast image and the left side the tissue. The brightness of the contrast enhanced signal of the lesion and liver was programmed according to lognormal indicator dilution models derived from mean values of quantification parameters extracted from clinical DCEUS acquisitions (see section 4.2.2). Specifically the lognormal indicator dilution model was fitted onto the clinical lesion time intensity curves and the mean values of the extracted quantification parameters of RT, MTT and PI were calculated.

The lesion was perfused according to the lognormal model[26] with a rise time (RT) of 17 seconds, a mean transit time (MTT) of 80 seconds and a peak intensity (PI) of 17 AIU (arbitrary intensity units). The parenchyma was perfused with a RT of 30 seconds, a MTT of 62 seconds and a PI of 33 AIU (Figure 4-2). On the tissue side of the acquisition constant intensity levels were kept between a low intensity background and a 50% higher intensity moving structure. The total simulation time was 74 seconds, the frame rate was set to 8Hz and the imaging plane consisted of 300 by 300 pixels (px).

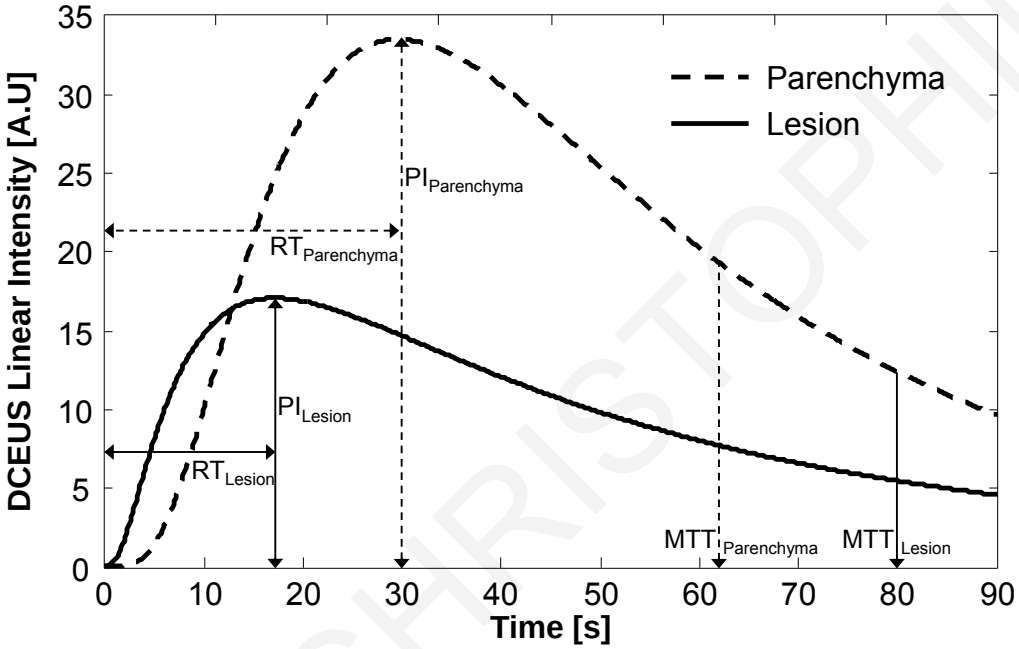

Figure 4-2: Lognormal indicator dilution model time intensity curves used to calculate the linear DCEUS intensity on the contrast side of the RMSM. The lognormal models were constructed using clinically derived (see section 4.2.2) quantification parameters (normal liver and liver lesions) for the RT, MTT, and PI.

The lesion was modeled as a sphere approximating the ellipsoid appearance of lesions seen in clinical acquisitions (Figure 4-1). The radius of the lesion was set at 20px (R_L) corresponding to the median liver lesion size from the clinical study and the parenchyma as a cube containing the lesion. In-plane and out-of-plane respiratory motion was produced by varying the position and radius of the lesion respectively according to a normalized respiratory kinetics curve ($G(t)$) that was extracted from patient data (Figure 4-3). A set of liver lesion radii [$r(t)$] corresponding to each time instance in the acquisition were calculated using (1) and the values of the in-plane translation [$\Delta r(t)$] of the liver lesion were determined using (2),

$$r(t) = \sqrt{R_L^{\,2} - \left(OPA \times G(t)\right)^2}\,, \tag{1}$$

$$\overrightarrow{\Delta r}(t) = IPA \times G(t)\left(\vec{i} + \vec{j}\right), \tag{2}$$

where *G(t)* was the patient derived normalized respiratory kinetics curve, R_L=20px, *t* was the time instance during the acquisition, *OPA* was a scalar defining the out-of-plane amplitude attributed to out-of-plane respiratory motion and *IPA* was a scalar defining the in-plane amplitude attributed to in-plane respiratory motion (Figure 4-4a). On the tissue side of the acquisition the bright moving structure was modeled as a triangular prism captured as a rectangle on the imaging plane as a representation of the oblong appearance of the diaphragm in clinical studies (Figure 4-1). The width of the rectangle was set to a constant value of 50 px and the values of the height of the triangle captured on the imaging plane were calculated using

$$h(t) = h_0 - \frac{OPA \times |G(t)|}{2}, \tag{3}$$

where *G(t)* was the patient derived normalized respiratory kinetics curve, h_o=20px, *t* was the time instance during the acquisition and *OPA* was a scalar specifying the out-of-plane amplitude attributed to out-of-plane respiratory motion (Figure 4-4b). In plane motion was imposed by varying the center of the rectangle according to (2).

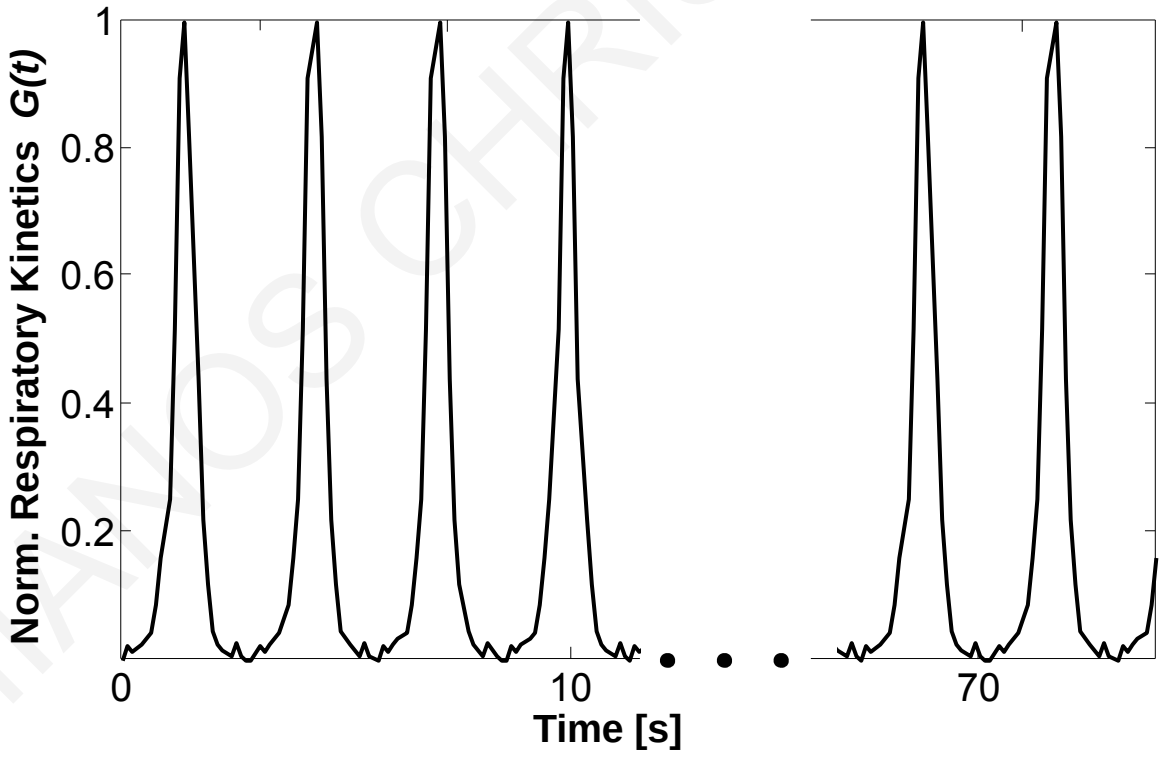

Figure 4-3: Normalized respiratory kinetics curve extracted from patient data that was used to drive the respiration motion of the respiratory motion simulation model.

Multiplicative noise was applied to the DCEUS side of the simulation in order to compare errors caused by respiratory motion to those produced by noise. The gamma

distribution multiplicative noise model proposed by Barrois et al[27] was used according to (4),

$$gamma(\mathrm{x};\kappa,\alpha)=\frac{x^{\kappa-1}e^{-\frac{x}{\alpha}}}{\Gamma(\kappa)\alpha^{\kappa}}, \quad (4)$$

where κ=3 and α=0.5. The k value of 3 was based on measurements performed by Barrois et al whereas the alpha value of 0.5 was derived based on the condition that the mode of the distribution (*Mo*) must have a value of 1. In order to apply the multiplicative noise from the gamma distribution each DCEUS frame of the simulation was multiplied by a random sample of a 300 x 300 matrix derived from the a gamma distribution with κ=3 and α=0.5. The random sample was generated using the "gamrnd" function part of MATLAB's Statistics Toolbox.

Three sets of simulations were run to study the effect of lesion size, in-plane and out-of-plane respiration amplitude. An additional set of simulations was run this time with multiplicative noise applied on the contrast side of the acquisition to investigate the effect of noise on the DCEUS quantification parameters extracted from the RMSM. The effect of lesion size on the DCEUS quantification parameters was studied with a set of simulations with increasing lesion radius between 10 and 35 px; the IPA was varied between 0 to 36 px and the OPA was set to 0 px. A set of simulations with a constant *OPA* of 10 px and a varying *IPA* between 0 to 36 px, a set with a constant *IPA* of 10px and a varying *OPA* between 0 to 36 px in order to evaluate the error introduced on the DCEUS quantification parameters from both in-plane and out-of-plane motion. The maximum amplitude of 36 px was chosen in order to simulate the clinical scenario in which the lesion is not visible in the imaging plane at the end phases of respiration. A set of simulations were also run with a constant *OPA* of 10 px and a varying *IPA* between 0 to 36 px with the presence of multiplicative noise on the DCEUS side of the acquisition.

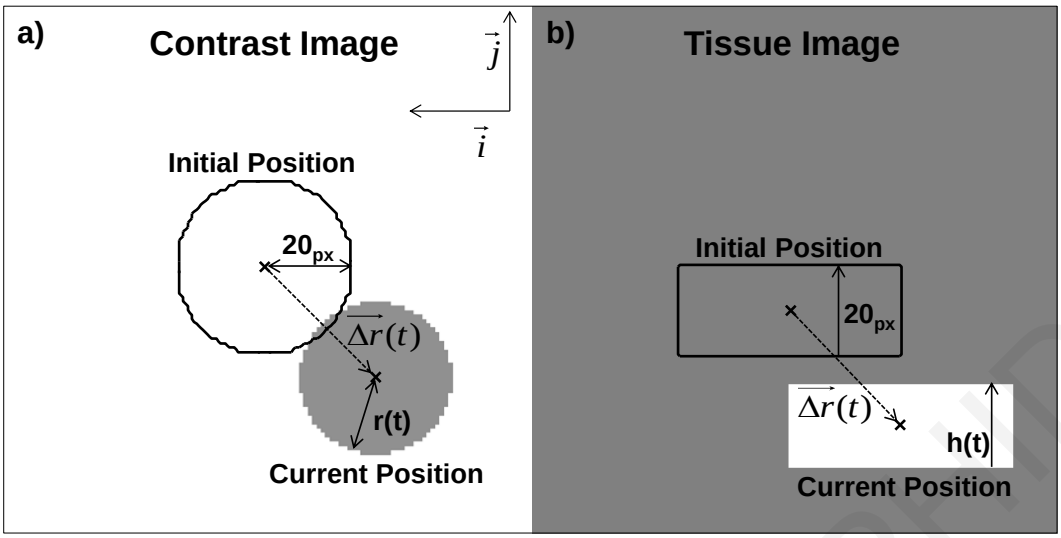

Figure 4-4: Zoom-in on a simulated dual contrast imaging acquisition at the time of peak of the parenchyma (29 seconds). a) Simulated DCEUS side of the acquisition with the initial position of the lesion indicated (solid black line) encompassing mostly the parenchyma with the lesion moved out of position in-plane by a vector $\Delta r(t)$ and a reduction of its radius from the initial radius of R_L (20 px) to $r(t)$ due to out-of-plane respiratory motion. b) Simulated tissue side of the acquisition with the moving structure out of position in-plane by a vector $\Delta r(t)$ and a variation in its height from h_0 (20 px) to $h(t)$ accounting for out-of-plane motion.

The mean linear intensity within a ROI corresponding to the initial position of the lesion on the contrast side of the RMSM (Figure 4-4a) at time zero was extracted across time. Due to the respiratory motion present in the simulation the lesion time intensity curve extracted will exhibit similar breathing artefacts as in the clinic. The lognormal indicator dilution model was fitted onto lesion time intensity curves extracted with and without the use of ARG. The quantification parameters of RT, MTT, area under the curve (AUC) and PI were calculated and compared to the input perfusion parameters of the RMSM. By comparing the error introduced on the quantification parameters the accuracy of DCEUS quantification with and without ARG can be assessed.

4.2.2 Clinical DCEUS acquisitions

Twenty-two (22) patients (10 female, 12 male) with liver metastasis were imaged. The median age of the female patients was 69 (range, 47-72) and the male median age was 74 (range, 59-77). Approval for the scanning was obtained by the ethics review board of our hospital. Also the procedure was fully explained to all participating patients and informed consent was obtained.

The Philips iU22 scanner (Philips Medical Systems, Bothell, WA) along with the C5-1 curve-linear array probe was utilized for all imaging. The imaging frequency was set at 1.7 MHz and the pulsing scheme used was power modulation with a mechanical index

(MI) of 0.06. One minute loops were acquired at a frame rate between 7-10 Hz in dual contrast imaging acquisition mode with an image resolution of 0.39mm/px. The time-gain-compensation (TGC) was set so that a very low level of uniform noise was present on the image before the arrival of the microbubbles, ensuring that the TGC was at the threshold of detection. In an effort to maintain a uniform pressure field the focus was set below the depth of the lesion. The Sonovue (Bracco s.p.a., Milan, Italy) microbubble contrast agent was injected as a 2.4mL bolus. The clinician maintained a constant imaging plane by monitoring the "tissue" side of the acquisition.

4.2.3 Image data analysis

The patient DICOM files were extracted from the Philips iU22 scanner and transferred to the commercial quantification software QLAB version 8.1 (Philips Medical Systems, Bothell, WA) for analysis. Both the arterial and late portal phases of the DCEUS loop were used to accurately draw a ROI encompassing the liver lesion. The frame at which the lesion was delineated was the reference that defined the breathing cycle phase to be extracted by the ARG algorithm. In particular this frame served as the "trigger" frame by which ARG was performed (see section 4.2.4). The lesion time intensity curves from linearized image data were extracted from QLAB and were analyzed with and without the implementation of the ARG.

Non-linear regression fits of the lognormal indicator dilution model [26] were performed on the lesion time intensity curves using MATLAB's Curve Fitting Toolbox trust region algorithm. The quantification parameters of AUC, PI, RT, and MTT were extracted from the lognormal model fit. In addition the quality of fit of the lognormal model on to the data was assessed by calculating the coefficient of determination (R^2_{LN}). The quality of fit has been used in the literature[21], [23], [25] as a metric of the improvement in the reliability of DCEUS quantification.

The effect of respiration on the DCEUS acquisitions was quantified by calculating the respiration amplitude (*RA*) of the time intensity curves extracted without the use of ARG. The *RA* was calculated by first computing the frequency spectrum of the lesion time intensity curves. The faster varying respiration component of the lesion time intensity curve was between the respiration range of 0.1-0.5 Hz [28] in contrast to the slower changing lesion perfusion pattern that was below 0.1Hz (Figure 4-5). The RA was calculated as the ratio between the area under the frequency spectrum between 0.1-0.5Hz and the area between 0-0.1Hz.

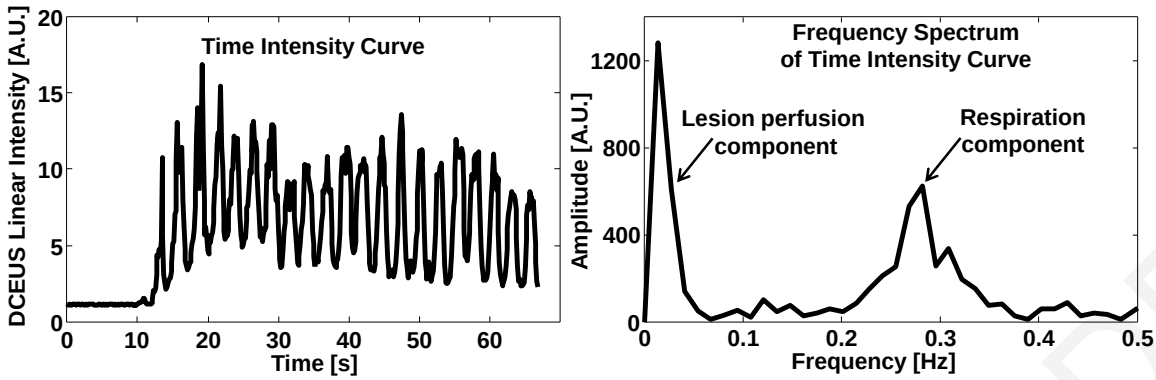

Figure 4-5: Example of a clinical lesion time intensity curve extracted from a DCEUS acquisition under the influence of respiratory motion (left) and its frequency spectrum (right). The separation of the lesion perfusion and respiration components is clearly shown in the frequency domain.

4.2.4 ARG algorithm

The ARG algorithm was applied on the tissue side of the dual contrast imaging acquisition. The MATLAB® (2012b, The MathWorks Inc., Natick, MA) scientific computing software was used to implement the ARG algorithm (Figure 4-6).

The location and intensity of motion produced by bright structures in the loop was identified by subtracting each frame from the average from all the frames[29] and summing the result. Bright moving structures were identified on the trigger frame and the intensity of the motion corresponding to each structure was calculated as the average motion intensity encompassed by the structure. In addition a frequency domain analysis was performed to calculate the respiratory contents associated with each moving structure. A ROI was constructed from the structure with the highest contents of respiratory motion and applied on the tissue loop to extract the time intensity curve. The troughs and peaks of the time intensity curve correspond to the time instances at which the acquisition was out-of-phase and in-phase with the trigger frame respectively. By removing the frames that were below 40% from the peak intensity the respiratory motion in the loop was reduced. The threshold value of 40% was a compromise between preserving enough time intensity curve data to perform a reliable fit of the lognormal indicator dilution model, while at the same time reducing the amount of respiratory motion in the loop. A more detailed description of the implementation of the ARG algorithm can be found in the literature[25].

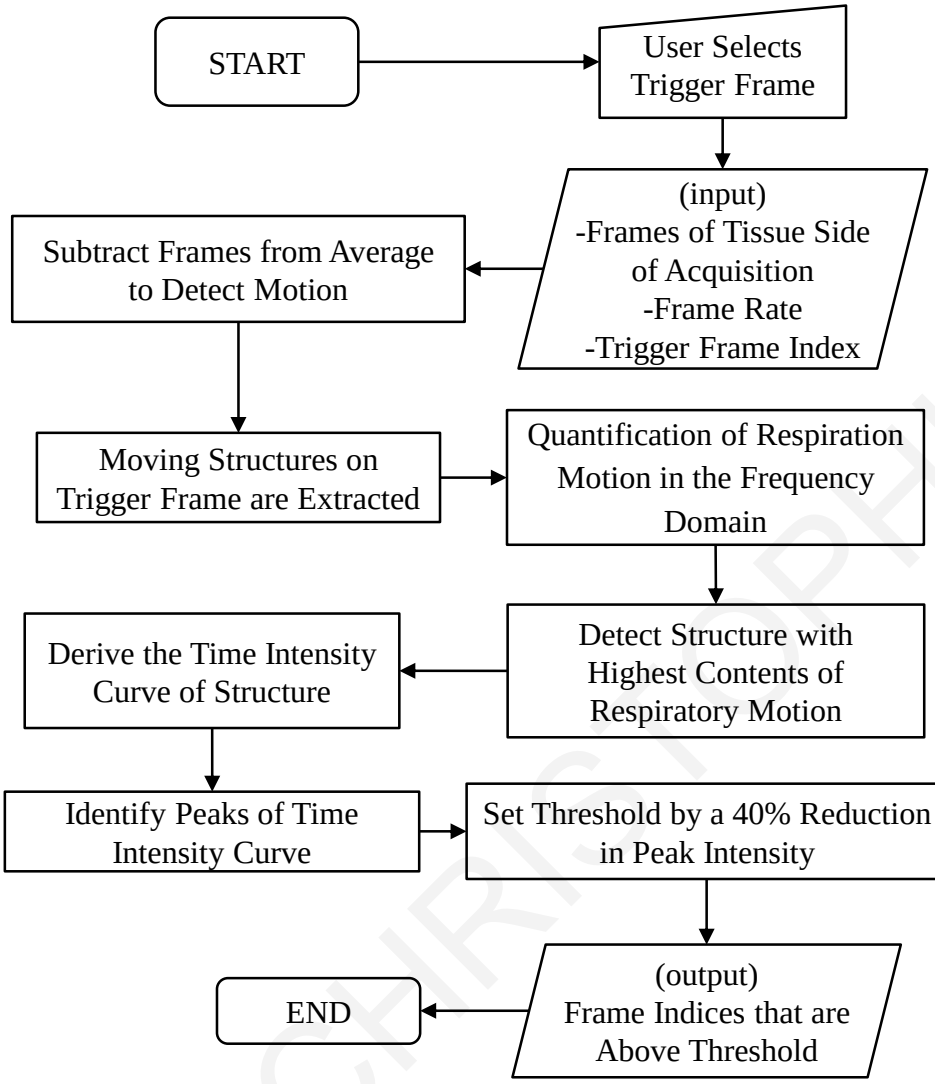

Figure 4-6: Summary flowchart of the processes used to implement the ARG algorithm in MATLAB.

4.3 Results

From the simulations investigating the effect of lesion size with increasing IPA it was shown that as the lesion size decreases the percentage error in the parameters increases for the same IPA (Figure 4-7). However when the IPA was normalized to the lesion radius of each simulation the percentage error of the quantification parameters was shown to be constant for the same IPA/R_L ratio (Figure 4-8). The results reported hereafter are in reference to the IPA/R_L and OPA/R_L.

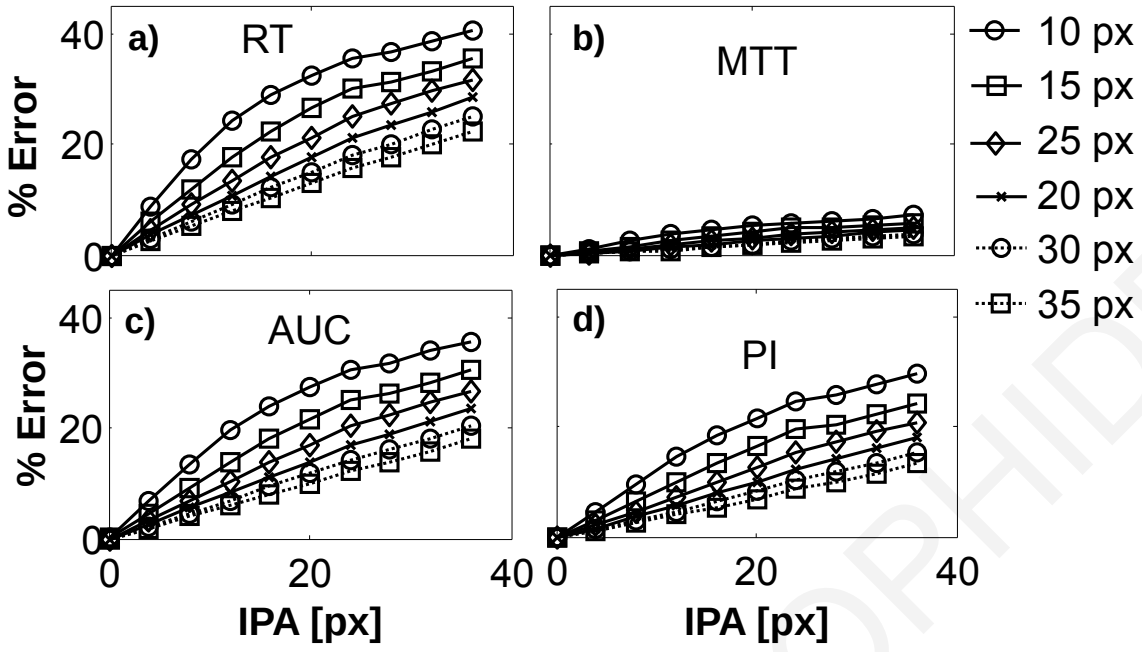

Figure 4-7: RMSM results with increasing in-plane respiratory amplitude and different lesion sizes. The percentage error for a) RT, b) MTT, c) AUC, and d) PI is shown.

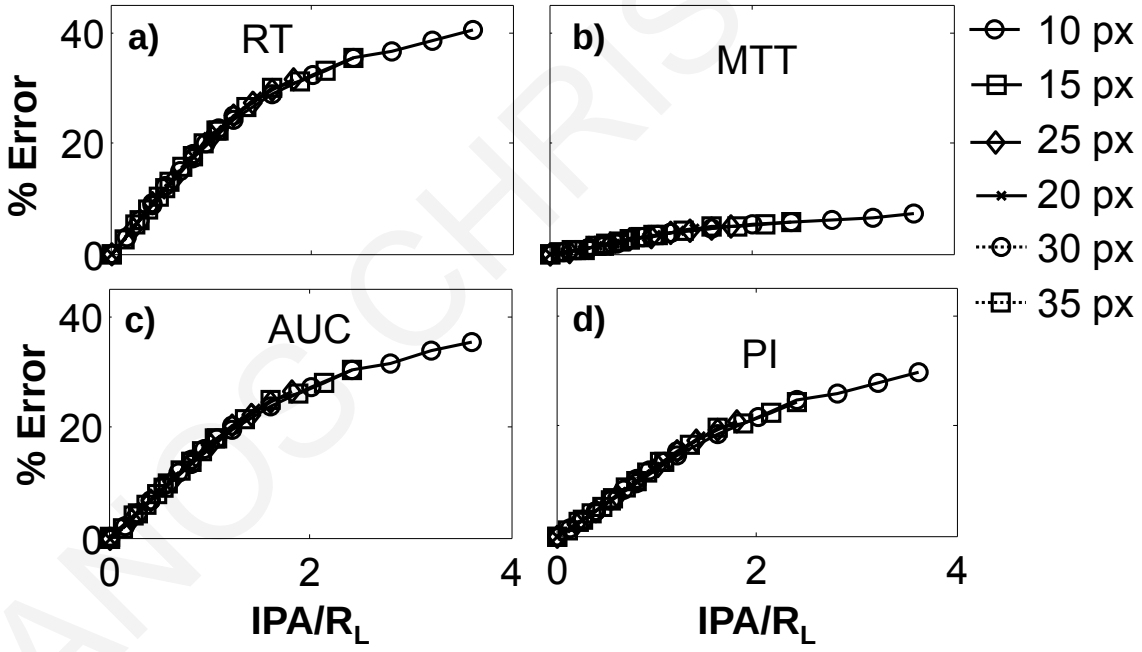

Figure 4-8: RMSM results from Figure 4-7 with the x-axis of the plots displaying the IPA normalized to the lesion radius (R_L=20px).

The results from the RMSM showed that ARG algorithm reduced the error in the quantification parameters introduced from in-plane respiratory motion (Figure 4-9). The overall errors where reduced from a mean of 13.0% to a mean of 2.4%. Specifically for the RT the mean error was decreased from 20.0% to a mean of 3.9%, for the MTT from a mean of 3.1% to 1.3%, for the AUC from 16.4% to a mean of 2.6% and for the PI from a mean of 12.4% to 2.0%. In addition to reducing errors introduced from in-plane respiratory

motion the ARG algorithm was shown to also reduce the errors from out-of-plane motion. The mean error introduced with increased OPA was reduced by 16.4%, 1.2%, 14.1% and 9.9% for the RT, MTT, AUC and PI respectively (Figure 4-10).

The reduction in the mean percentage error of quantification parameters with the use of ARG was tested using the paired t-test at a significance level of 0.001. It was found to be statistically significant for the RT, AUC and PI ($p<0.001$) both for in-plane and out-of-plane respiratory motion. The reduction of the MTT percentage error was found not to be significant for the in-plane ($p=0.014$) and out-of-plane ($p=0.044$) motion. MTT did not suffer much from motion as it is a time parameter associated with the overall duration of the bolus that despite the respiratory noise it still remains unaffected. As an example, consider adding high frequency noise (respiratory noise) on a low frequency signal (MTT). The overall effective period of the low frequency signal remains unaffected.

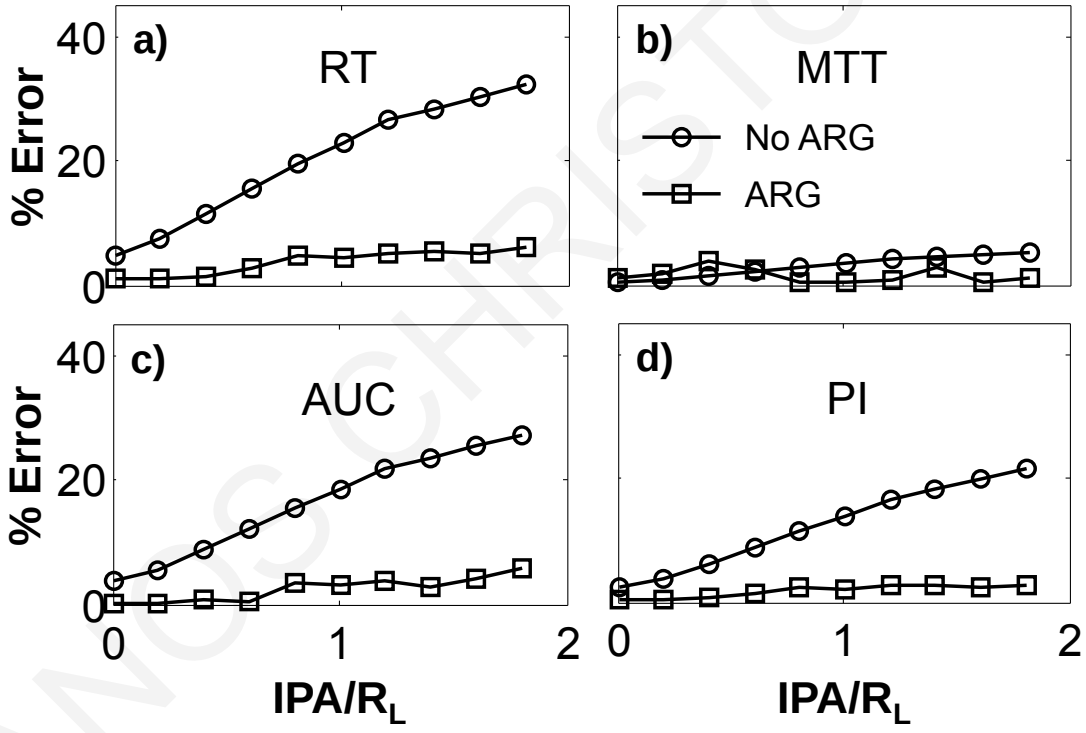

Figure 4-9: Percent error of the quantification parameters with increasing in-plane respiratory amplitude with (squares) and without (circles) the use of the ARG algorithm.

The multiplicative noise introduced on the DCEUS simulation had no effect on the RT and MTT with the results with and without noise being almost identical [compare Figure 4-9(a)-(b) with Figure 4-11(a)-(b)]. However noise did increase the errors for the amplitude quantification parameters by a mean value of 50.0% for AUC and 50.0% for PI [compare Figure 4-9(c)-(d) with Figure 4-11(c)-(d)]. The error increase due to noise for the amplitude parameters was almost constant across increasing IPA with the calculated standard deviation of the mean increase in error being less than 0.6%.

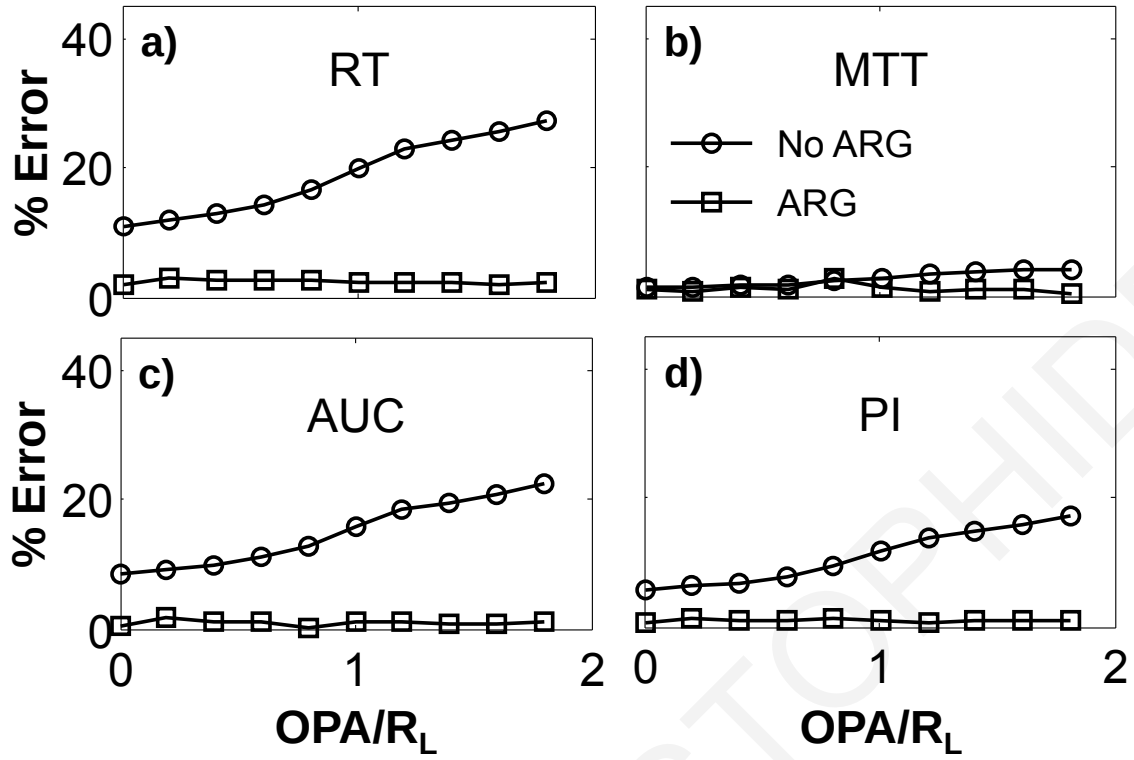

Figure 4-10: Same as Figure 4-9 but with out-of-plane motion. Percent error of the quantification parameters with increasing out-of-plane respiratory amplitude with (squares) and without (circles) the use of the ARG algorithm.

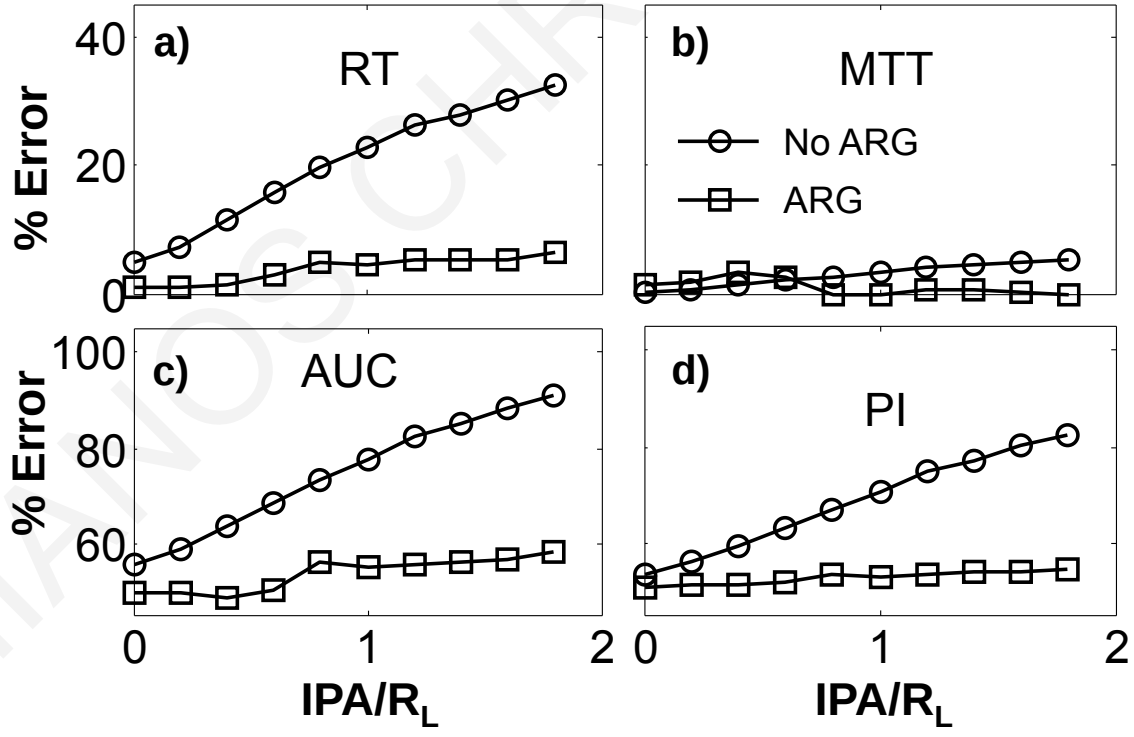

Figure 4-11: Same as Figure 4-9 but with added multiplicative noise. Percent error of the quantification parameters with the application of multiplicative noise under increasing in-plane respiratory amplitude with (squares) and without (circles) the use of the ARG algorithm.

The overall RMSM validity was evaluated by comparing the relationship between the R^2_{LN} and the respiration amplitude (RA) extracted both from the simulation and patient

data. Simulation data using the parenchyma perfusion model extended to an *RA* of 1.1 whereas the clinical data extended to an *RA* of 2.2. This was attributed to the fact that clinical data include signal from nearby vessels, like veins, that can contribute to a higher linear intensity within the lesion ROI compared to the parenchyma. In order to investigate the effect of vessels to lesion DCEUS quantification parameters a set of simulations were run with constant OPA and variable IPA. The parenchyma perfusion model was replaced with a vein model with a RT of 27 seconds, a MTT of 54 seconds and a PI of 190 AIU derived from the clinical data. The results from both simulation sets were compared with the clinical data (Figure 4-12). Both the clinical data and the simulations demonstrate a negative correlation with the R^2_{LN} decreasing as the *RA* increases without the use of ARG. The slope of the linear regression was -0.33 and -0.40 for the clinical and simulation data respectively. With the use of ARG the slope was decreased for both the patient (-0.12) and simulation data (-0.14).

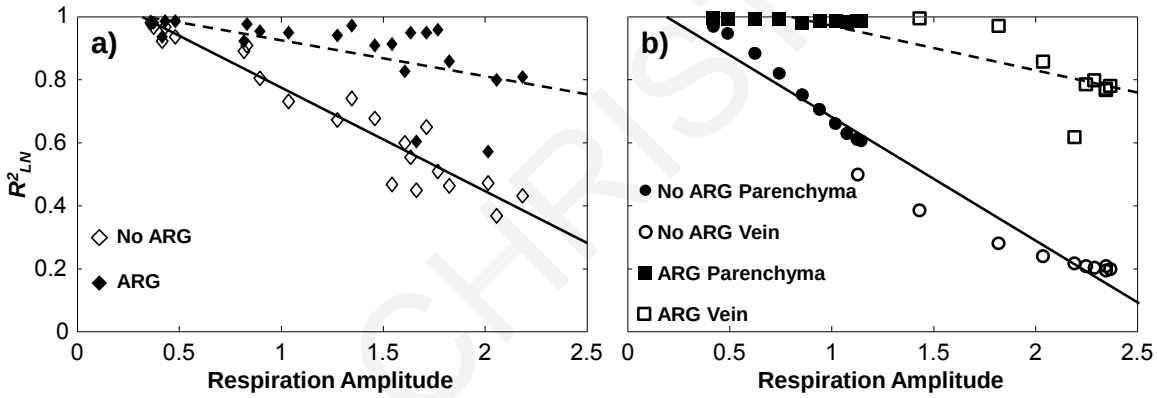

Figure 4-12: Scatter plots of R^2_{LN} vs. respiration amplitude with and without the use of automatic respiratory gating (ARG) for a) clinical patient data and b) simulation results from the RMSM. The linear regression lines of the displayed data are also shown without (dotted) and with (solid) ARG.

4.4 Discussion

In this study a RMSM was developed that was used to study the effectiveness of an ARG algorithm in increasing the absolute accuracy of liver lesion DCEUS quantification. The use of simulation to evaluate respiratory compensation algorithms for liver lesion DCEUS has been previously suggested by Renault et al[20]. The simulation by Renault et al examined the effects of respiration for a single in-plane and out-of-plane amplitude with only the contrast side of the acquisition being simulated. Furthermore the errors that respiration introduced on lesion time intensity curves were evaluated qualitatively without looking into specific quantification parameters. That study concluded that image registration based algorithms for respiratory motion compensation were inadequate in

removing out-of-plane motion from liver DCEUS acquisitions. The independent component analysis (ICA) method proposed by Renault et al and the principal component analysis (PCA) examined by Mule et al[19] have been shown to remove both in-plane and out-of-plane motion from DCEUS loops. However only the end phases of the respiratory cycle can be extracted using ICA and PCA analysis, and since the acquisition is two dimensional there is the uncertainty whether a portion or any part of the lesion will be present on the extracted frames.

The RMSM used in this study considers a broad range of out-of-plane and in-plane respiratory motion amplitudes. The application of the ARG algorithm on the dual contrast imaging mode simulation has been shown to significantly reduce the errors on DCEUS quantification parameters. Overall the implementation of the ARG algorithm significantly reduced the errors introduced by respiratory motion ($p<0.001$) from a maximum of 32.3% to less than 6.3%. ARG produced significant gains in DCEUS quantification parameter accuracy for the RT, AUC and PI ($p<0.001$) whereas the impact of ARG on MTT was not significant. This was also the case for a clinical study [24] where the MTT was found to be unaffected by the ARG algorithm.

The increase in the accuracy from the use of the ARG algorithm can improve clinical outcomes in liver DCEUS quantification. For example in a clinical study on liver lesion DCEUS quantification by Averkiou et al [10] the response of patients to treatment was detected as a mean change in the wash-in time ratio quantification parameter of 17% after the first treatment. Zocco et al [30] found significant changes from the baseline of -20% and -25% in the AUC and PI respectively for patients that had a response to hepatocellular carcinoma treatment. Both Averkiou et al and Zocco et al used respiratory gating to improve the accuracy of their quantitative analysis. These changes in the quantification parameters would be impossible to detect if there is an error of about 30% already present due to the respiratory motion. Furthermore in the quantification parameter reproducibility study performed by Averkiou et al an average deviation of 9% was calculated which is above the maximum residual error of 6.3% remaining after the use of ARG.

By taking into consideration multiplicative noise on the contrast side of the dual contrast imaging simulation no change was observed on the time quantification parameters of RT and MTT. The results were almost identical with the maximum difference being less than 1.8% for the RT and MTT extracted both with and without ARG. On the other hand the amplitude parameters of AUC and PI were severely affected with the value of the AUC error increasing by a maximum of 51.4% and of the PI by a maximum of 50.5%.

Simulations run by Barrois et al [27] found absolute error differences for the AUC of 49.8-50.3% , the MTT of 15.5-22.0% and 4.3-5.6% for the RT. The simulations applied multiplicative noise directly onto each data point of the time intensity curve, corresponding to a mean signal from a 5x5 block of pixels, in contrast with the RMSM that takes the average within a 20px radius ROI. Thus the sample size used to calculate the values of the time intensity curve data points for the current study is 1257 compared with 25 from Barrois et al. The standard error of the mean, $SE = \frac{\sigma}{\sqrt{n}}$ [31], is thus expected to be higher for the smaller sample explaining the discrepancy between the results obtained from the two studies. Therefore the errors reported by Barrois et al are more relevant to parametric imaging studies rather than the modeling of the average perfusion of a liver lesion.

The errors introduced from the gamma distribution noise model on the amplitude parameters can be predicted analytically. The mean and standard deviation can be calculated from the moments of the gamma distribution[32] and are given by $\mu = \kappa \times \alpha$ and $\sigma = \sqrt{k} \times \alpha$. Also by differentiating (4) the mode (i.e. maximum of the probability density function) can be calculated as $Mo = (\kappa - 1) \times \alpha$. By eliminating κ and α the mode can be written in respect to μ and σ as $Mo = \frac{\mu^2 - \sigma^2}{\mu}$. The multiplicative model used from the work of Barrois et al[27] uses the relationship between the standard deviation (σ), the mean (μ), and the shape parameter κ of the gamma distribution to estimate κ from DCEUS measurements of the standard deviation and mean linear intensity with increasing concentration of microbubbles. Since the relationship used [27] between σ and μ is a linear model $\sigma = slope \times \mu$ and also $\sigma = \frac{\mu}{\sqrt{\kappa}}$, derived from the moments of the gamma distribution, the mean, and the mode can directly related to the shape parameter κ by $\mu = \left(\frac{\kappa}{\kappa - 1} \right) \times Mo$. Consequently the mean (μ) linear intensity within the ROI will be one and a half times the value of the mean liner intensity before the gamma distribution noise was applied with parameters κ=3 and *Mo*=1 used in the RMSM. The overall mean error between the amplitude parameters extracted with and without multiplicative from the simulation was found to be 50.0% with a standard deviation of less than 0.5% verifying the analysis made. As already mentioned in the previous paragraph the error obtained from the simulations by Barrois et al for the AUC was between 49.8-50.3% agreeing with the prediction of the analysis presented.

Limitations of the RMSM include simplifications made compared to the complexity of clinical dual contrast imaging acquisitions. The shape of clinical lesions does not follow a strict spherical shape as used in the RMSM although an ellipsoidal shape is generally assumed for demonstration purposes[7]. In addition respiratory motion does not only cause rigid in-plane and out-of-plane motion but also results in deformation due to the elasticity of tissue. The deformation of the lesions due to respiratory motion was not accounted for in the RMSM. Despite of these limitations of the RMSM it offers a controlled platform by which to study the absolute errors introduced by respiratory motion on DCEUs quantification parameters. Furthermore the RMSM has the potential to be used in the training of clinicians in DCEUS quantification in an effort to increase intra-observer and inter-observer agreement. This could be especially useful for multi-centre studies since the training can be performed remotely and data analysis can be centralized. Future studies of respiratory motion could also simulate 3D DCEUS acquisitions to investigate the effect of respiratory motion compensation schemes on DCEUS quantification. However 3D DCEUS is not currently used routinely in the clinic[33] thus there are not enough clinical data available to construct such a model.

Both the perfusion and respiration kinetics of the RMSM were derived from clinical dual contrast imaging acquisitions in an effort to maximize the clinical relevance of the model. The similarities of the relationship between R^2_{LN} and *RA* for the RMSM and the clinical data give confidence to the clinical suitability of the model (Figure 4-12). This further reinforces that the results obtained for the error reduction in DCEUS quantification parameters are expected to occur in the clinic.

4.5 Conclusion

A RMSM was presented that takes into account in-plane, out-of-plane respiratory motion, and multiplicative noise. The RMSM was used to investigate the effectiveness of an ARG algorithm in increasing the accuracy of liver lesion DCEUS quantification by removing in-plane and out-of-plane motion from dual contrast imaging mode acquisitions. The use of RMSM clearly revealed that the ARG algorithm significantly reduces errors introduced from in-plane and out-of-plane respiratory motion. The time quantification parameters of RT and MTT remained almost unaffected under the presence of multiplicative speckle noise whereas the amplitude quantification parameters of AUC and PI showed a constant error of 50% from their set values. The relationship between the quality-of-fit (R^2_{LN}) and the respiration amplitude (*RA*) for both clinical and RMSM-

simulated data was similar thus confirming the clinical relevance of the simulation. Finally, the RMSM has proven to be a useful tool in studying bolus kinetics and investigating the impact of ARG on the accuracy of liver lesion DCEUS quantification parameters.

References

[1] P. N. Burns, "Harmonic imaging with ultrasound contrast agents.," *Clin Radiol*, vol. 51 Suppl 1, pp. 50–5, Feb. 1996.

[2] C. Huang-Wei, A. Bleuzen, P. Bourlier, J. Roumy, A. Bouakaz, L. Pourcelot, and F. Tranquart, "Differential diagnosis of focal nodular hyperplasia with quantitative parametric analysis in contrast-enhanced sonography.," *Invest Radiol*, vol. 41, no. 3, pp. 363–8, Mar. 2006.

[3] L. Galiuto, B. Garramone, A. Scarà, A. G. Rebuzzi, F. Crea, G. La Torre, S. Funaro, M. Madonna, F. Fedele, and L. Agati, "The Extent of Microvascular Damage During Myocardial Contrast Echocardiography Is Superior to Other Known Indexes of Post-Infarct Reperfusion in Predicting Left Ventricular Remodeling," *J Am Coll Cardiol*, vol. 51, no. 5, pp. 552–9, Feb. 2008.

[4] R. Senior et al., "Detection of coronary artery disease with perfusion stress echocardiography using a novel ultrasound imaging agent: two Phase 3 international trials in comparison with radionuclide perfusion imaging.," *Eur J Echocardiogr*, vol. 10, no. 1, pp. 26–35, Jan. 2009.

[5] K. Wei, A. R. Jayaweera, S. Firoozan, A. Linka, D. M. Skyba, and S. Kaul, "Basis for detection of stenosis using venous administration of microbubbles during myocardial contrast echocardiography: bolus or continuous infusion?," *J Am Coll Cardiol*, vol. 32, no. 1, pp. 252–260, Jul. 1998.

[6] M. Averkiou, M. Bruce, S. Jensen, P. Rafter, T. Brock-Fishe, and J. Powers, "Pulsing schemes for the detection of nonlinear echoes from contrast microbubbles," in *9th European Symposium on Ultrasound Contrast Imaging*, 2004, pp. 17–24.

[7] S. R. Wilson and P. N. Burns, "Microbubble-enhanced US in body imaging: what role?," *Radiology*, vol. 257, pp. 24–39, 2010.

[8] A. Muhi, T. Ichikawa, U. Motosugi, H. Sou, H. Nakajima, K. Sano, M. Sano, S. Kato, T. Kitamura, Z. Fatima, K. Fukushima, H. Iino, Y. Mori, H. Fujii, and T. Araki, "Diagnosis of colorectal hepatic metastases: Comparison of contrast-enhanced CT, contrast-enhanced US, superparamagnetic iron oxide-enhanced MRI, and gadoxetic acid-enhanced MRI," *J. Magn. Reson. Imaging*, vol. 34, no. 2, pp. 326–335, Aug. 2011.

[9] F. Tranquart et al., "Role of contrast-enhanced ultrasound in the blinded assessment of focal liver lesions in comparison with MDCT and CEMRI: Results from a multicentre clinical trial," *Eur. J. Cancer Suppl.*, vol. 6, no. 11, pp. 9–15, Sep. 2008.

[10] M. Averkiou, M. Lampaskis, K. Kyriakopoulou, D. Skarlos, G. Klouvas, C. Strouthos, and E. Leen, "Quantification of tumor microvascularity with respiratory gated contrast enhanced ultrasound for monitoring therapy.," *Ultrasound Med Biol*, vol. 36, no. 1, pp. 68–77, Jan. 2010.

[11] M. Bertolotto, G. Pozzato, L. S. Crocè, F. Nascimben, C. Gasparini, M. A. Cova, and C. Tiribelli, "Blood flow changes in hepatocellular carcinoma after the administration of thalidomide assessed by reperfusion kinetics during microbubble infusion: preliminary results.," *Invest Radiol*, vol. 41, no. 1, pp. 15–21, Jan. 2006.

[12] N. Lassau, S. Koscielny, L. Chami, M. Chebil, B. Benatsou, A. Roche, M. Ducreux, D. Malka, and V. Boige, "Advanced hepatocellular carcinoma: early evaluation of response to bevacizumab therapy at dynamic contrast-enhanced US with quantification--preliminary results.," *Radiology*, vol. 258, no. 1, pp. 291–300, Jan. 2011.

[13] C. F. Dietrich, M. A. Averkiou, J.-M. Correas, N. Lassau, E. Leen, and F. Piscaglia, "An EFSUMB introduction into Dynamic Contrast-Enhanced Ultrasound (DCE-US) for quantification of tumour perfusion.," *Ultraschall Med*, vol. 33, no. 4, pp. 344–51, Aug. 2012.

[14] E. Leen, M. Averkiou, M. Arditi, P. Burns, D. Bokor, T. Gauthier, Y. Kono, and O. Lucidarme, "Dynamic contrast enhanced ultrasound assessment of the vascular effects of novel therapeutics in early stage trials.," *Eur Radiol*, vol. 22, no. 7, pp. 1442–50, Jul. 2012.

[15] A. Thapar, J. Shalhoub, M. Averkiou, C. Mannaris, A. H. Davies, and E. L. S. Leen, "Dose-dependent artifact in the far wall of the carotid artery at dynamic contrast-enhanced US.," *Radiology*, vol. 262, no. 2, pp. 672–9, Feb. 2012.

[16] M. Lampaskis and M. Averkiou, "Investigation of the relationship of nonlinear backscattered ultrasound intensity with microbubble concentration at low MI.," *Ultrasound Med Biol*, vol. 36, no. 2, pp. 306–12, Mar. 2010.

[17] D. Klein, M. Jenett, H.-J. Gassel, J. Sandstede, and D. Hahn, "Quantitative dynamic contrast-enhanced sonography of hepatic tumors.," *Eur. Radiol.*, vol. 14, no. 6, pp. 1082–91, Jun. 2004.

[18] H. S. Markus and M. J. Harrison, "Estimation of cerebrovascular reactivity using transcranial Doppler, including the use of breath-holding as the vasodilatory stimulus.," *Stroke*, vol. 23, no. 5, pp. 668–73, May 1992.

[19] S. Mulé, N. Kachenoura, O. Lucidarme, A. De Oliveira, C. Pellot-Barakat, A. Herment, and F. Frouin, "An automatic respiratory gating method for the improvement of microcirculation evaluation: application to contrast-enhanced ultrasound studies of focal liver lesions.," *Phys Med Biol*, vol. 56, no. 16, pp. 5153–65, Aug. 2011.

[20] G. Renault, F. Tranquart, V. Perlbarg, A. Bleuzen, A. Herment, and F. Frouin, "A posteriori respiratory gating in contrast ultrasound for assessment of hepatic perfusion.," *Phys Med Biol*, vol. 50, no. 19, pp. 4465–80, Oct. 2005.

[21] N. Rognin, R. Campos, J. Thiran, T. Messager, P. Broillet, P. Frinking, M. Mercier, and M. Arditi, "A new approach for automatic motion compensation for improved estimation of perfusion quantification parameters in ultrasound imaging," in *Proceedings of the 8th French Conference on Acoustics*, 2006, pp. 61–65.

[22] N. G. Rognin et al., "Parametric imaging for characterizing focal liver lesions in contrast-enhanced ultrasound.," *IEEE Trans Ultrason Ferroelectr Freq Control*, vol. 57, no. 11, pp. 2503–11, Nov. 2010.

[23] J. Zhang, M. Ding, F. Meng, M. Yuchi, and X. Zhang, "Respiratory motion correction in free-breathing ultrasound image sequence for quantification of hepatic perfusion," *Med Phys*, vol. 38, no. 8, pp. 4737–4748, Aug. 2011.

[24] D. Christofides, E. L. S. Leen, and M. A. Averkiou, "Improvement of the accuracy of liver lesion DCEUS quantification with the use of automatic respiratory gating.," *Eur. Radiol.*, Apr. 2015.

[25] D. Christofides, E. Leen, and M. Averkiou, "Automatic respiratory gating for contrast ultrasound evaluation of liver lesions.," *IEEE Trans. Ultrason. Ferroelectr. Freq. Control*, vol. 61, no. 1, pp. 25–32, Jan. 2014.

[26] C. Strouthos, M. Lampaskis, V. Sboros, A. McNeilly, and M. Averkiou, "Indicator dilution models for the quantification of microvascular blood flow with bolus administration of ultrasound contrast agents.," *IEEE Trans Ultrason Ferroelectr Freq Control*, vol. 57, no. 6, pp. 1296–310, Jun. 2010.

[27] G. Barrois, A. Coron, T. Payen, A. Dizeux, and L. Bridal, "A multiplicative model for improving microvascular flow estimation in dynamic contrast-enhanced ultrasound (DCE-US): theory and experimental validation.," *IEEE Trans. Ultrason. Ferroelectr. Freq. Control*, vol. 60, no. 11, pp. 2284–94, Nov. 2013.

[28] S. Fleming, M. Thompson, R. Stevens, C. Heneghan, A. Plüddemann, I. Maconochie, L. Tarassenko, and D. Mant, "Normal ranges of heart rate and respiratory rate in children from birth to 18 years of age: a systematic review of observational studies.," *Lancet*, vol. 377, no. 9770, pp. 1011–8, Mar. 2011.

[29] A. Jain, *Fundamentals of Digital Image Processing*. Englewood Cliffs, NJ: Prentice-Hall, 1989.

[30] M. A. Zocco et al., "Early prediction of response to sorafenib in patients with advanced hepatocellular carcinoma: The role of dynamic contrast enhanced ultrasound," *J. Hepatol.*, vol. 59, no. 5, pp. 1014–1021, 2013.

[31] D. G. Altman and J. M. Bland, "Standard deviations and standard errors.," *BMJ*, vol. 331, no. 7521, p. 903, Oct. 2005.

[32] R. Scheaffer, M. Mulekar, and J. McClave, *Probability and Statistics for Engineers*, 5th ed. Cengage Learning, 2010.

[33] J. M. Hudson, R. Williams, C. Tremblay-Darveau, P. S. Sheeran, L. Milot, G. A. Bjarnason, and P. N. Burns, "Dynamic contrast enhanced ultrasound for therapy monitoring.," *Eur. J. Radiol.*, 2015.

5

Carotid atherosclerotic plaque perfusion of symptomatic and asymptomatic patients with DCEUS

Submitted for review; by Damianos Christofides, Edward Leen, Brahman Dharmarajah, Alun Davies, Andrew Nicolaides and Michalakis Averkiou in European Radiology. 2015 Jul

Patent Application: Michalakis Averkiou, Edward Leen, and Damianos Christofides, "Evaluation of carotid plaque using contrast enhanced ultrasonic imaging," World Intellectual Property Organization Provisional Patent Application #PCT/IB2015/050452, 2015. (Appendix 2)

Abstract

Objectives: To detect differences in the extent of carotid intraplaque microflow between symptomatic and asymptomatic patients using both qualitative and quantitative dynamic contrast-enhanced ultrasound (DCEUS) analysis.

Methods Twenty-seven patients were enrolled in the study and underwent DCEUS of the carotid artery. The extent of the microflow within the carotid plaques was qualitatively graded as 1 if more of 50% of their area was covered by moving microbubbles otherwise a score of 0 was given. Quantitative analysis was also performed in which the percent perfusion coverage of the carotid plaques was calculated. The qualitative and quantitative analyses were performed by two independent observers. The study was approved by the UK National Research Ethics Service and informed consent was obtained.

Results: The proportion of asymptomatic patients that received a qualitative score of 1 was significantly greater than the symptomatic($p<0.05$). The quantitative scores of carotid plaque percent perfusion coverage were significantly higher in asymptomatic patients compared to symptomatic($p<0.05$). Significant inter-observer agreement was demonstrated($p<0.05$).

Conclusions: Qualitative and quantitative analysis demonstrated that carotid plaques from asymptomatic patients had a greater extent of microflow compared to symptomatic patients. The increased perfusion in asymptomatic patients is indicative of plaque vulnerability in some of the plaques examined.

Key Points:

- DCEUS quantification can measure the percent perfusion coverage of carotid plaques
- Carotid plaques from symptomatic patients have reduced perfusion coverage compared to asymptomatic
- Quantitative DCEUS can monitor the microflow in carotid plaques for risk stratification

Keywords: Contrast Agents; Carotid Artery Plaque; Neovascularization,;Ultrasound Imaging;Microbubbles

5.1 Introduction

Stroke is a significant cause of death in the western world accounting for more than 5% of deaths in the United States[1] and 650,000 deaths annually in Europe[2]. Up to 20 % of ischemic strokes can be attributed to stenosis in extra-cranial carotid arteries[3]. The ability to categorize which carotid atherosclerotic plaques are likely to cause symptoms is a key challenge in addressing the high morbidity and mortality caused by stroke.

Histological results by Moreno et al[4] showed that plaques that have ruptured contained a higher density of microvessels than non-ruptured plaques. Furthermore McCarthy et al[5] showed that significantly more neovessels are formed in plaques from symptomatic patients than from asymptomatic patients. The histology studies suggest that plaques that are vulnerable in causing symptoms are at some point of their evolution perfused to a greater extent than non-vulnerable plaques.

Non-invasive imaging techniques are an ideal tool for the characterization of perfusion in carotid atherosclerotic plaques. Dynamic contrast enhanced ultrasound (DCEUS) utilizes gas filled microbubbles as a pure intravascular contrast agent to detect very low velocity blood flow (<1 cm/sec) in carotid atherosclerotic plaques. In a qualitative DCEUS study by Staub et al[6] the perfusion characteristics of 293 atherosclerotic plaques were evaluated and a correlation was established between the degree of plaque echogenicity in B-mode and the extent of moving microbubbles within the carotid plaque using DCEUS. Coli et al[7] demonstrated an association between qualitative scores of intraplaque microbubble coverage and the histological density of microvessels in carotid plaques. Xiong et al[8] employed both qualitative and quantitative DCEUS to demonstrate increased signal enhancement in carotid atherosclerotic plaques from symptomatic patients compared to asymptomatic. A quantitative analysis of carotid plaque DCEUS loops from 22 patients with severe (70-99%) stenosis by Hoogi et al[9] showed a strong correlation between the percentage coverage of plaque neovascularization measured using histology and quantitative DCEUS. Furthermore Akkus et al[10] found significant correlation between the area of intraplaque neovascularization calculated using an adaptive image threshold technique and visual scores from 45 carotid plaque DCEUS loops.

In this study DCEUS was performed on 27 symptomatic and asymptomatic patients with carotid atherosclerotic plaques. A novel DCEUS quantification technique was developed specifically to address the challenge of measuring the extent of low intensity microflow within carotid plaques. The purpose of this study is to detect differences in the extent of carotid intraplaque microflow between symptomatic and asymptomatic patients using both qualitative and quantitative DCEUS analysis.

5.2 Materials and methods

5.2.1 Patient population

Ethical approval was obtained prior to commencing the study (Ref 09/H0706/89). Written informed consent was obtained from all patients. Twenty-seven consecutive

patients with a discrete 50-99% internal carotid artery stenosis in relation to the normal distal internal carotid diameter (NASCET equivalent[11]) were recruited from neurovascular clinics between January 2011 and January 2012. Inclusion criteria were: male or female patients aged 18 years or over with a 50-99% (NASCET) internal carotid artery stenosis. Exclusion criteria were: atrial fibrillation, mechanical heart valve, cardiomyopathy, elevated troponin, contrast contraindication, NYHA III/IV cardiac failure, myocardial infarction within 3 months and neurovascular ischemic symptoms >4 weeks previously. An independent stroke physician assigned the diagnosis of carotid territory ischemic symptoms after a workup including intracranial computed tomography, 24 hour electrocardiogram, troponin result, echocardiography and for cases of amaurosis fugax, an ophthalmic opinion. If no history of stroke, transient ischemic attack or amaurosis were present, an asymptomatic status was recorded.

5.2.2 DCEUS acquisitions

The Philips iU22 scanner (Philips Medical Systems, Bothell, WA) along with the L9-3 linear array probe was utilized for all imaging. System settings were: power modulation (PM) with a mechanical index (MI) of 0.06 and frame rate between 13-16 Hz. One minute loops of carotid plaques were acquired in dual contrast imaging mode. The 2D gain was carefully set just above the noise floor for maximum sensitivity. The focus was set below the depth of the plaque for a uniform pressure field[12]. A 2 mL bolus of microbubble contrast agent Sonovue (Bracco s.p.a., Milan, Italy) was injected intravenously. A constant imaging plane was maintained by monitoring the "tissue" side of the acquisition.

The acquired DCEUS loops were evaluated off-line by an independent, blinded observer, not present at the DCEUS scans. The twenty-seven (27) patients enrolled in the study were analyzed both quantitatively and qualitatively with the methods developed in the present work.

5.2.3 Qualitative analysis

The DICOM files of the patient's scans were exported to QLAB for off-line analysis by a trained observer. The observer changed zoom, contrast and brightness in low light ambient conditions to optimize viewing of the DCEUS loop images. Moving microbubbles within the ROI encompassing the plaque were considered indicators of plaque perfusion. The trained observer would visually compare the area that had moving microbubbles to the total area of the plaque. A qualitative assessment was then made in regards to the percentage area of the plaque covered with moving microbubbles. Carotid

atherosclerotic plaques were graded as having significant perfusion if more than 50% of their area was considered to be covered by moving microbubbles.

5.2.4 Quantitative analysis

The quantitative analysis was divided into two stages. The first stage of the analysis was performed in QLAB version 8.1 (Philips Medical Systems, Bothell, WA). The data derived from the QLAB stage of the analysis were then accessed from MATLAB (2012b, The MathWorks Inc., Natick, MA) in order to quantify the extent of perfusion in the carotid plaques.

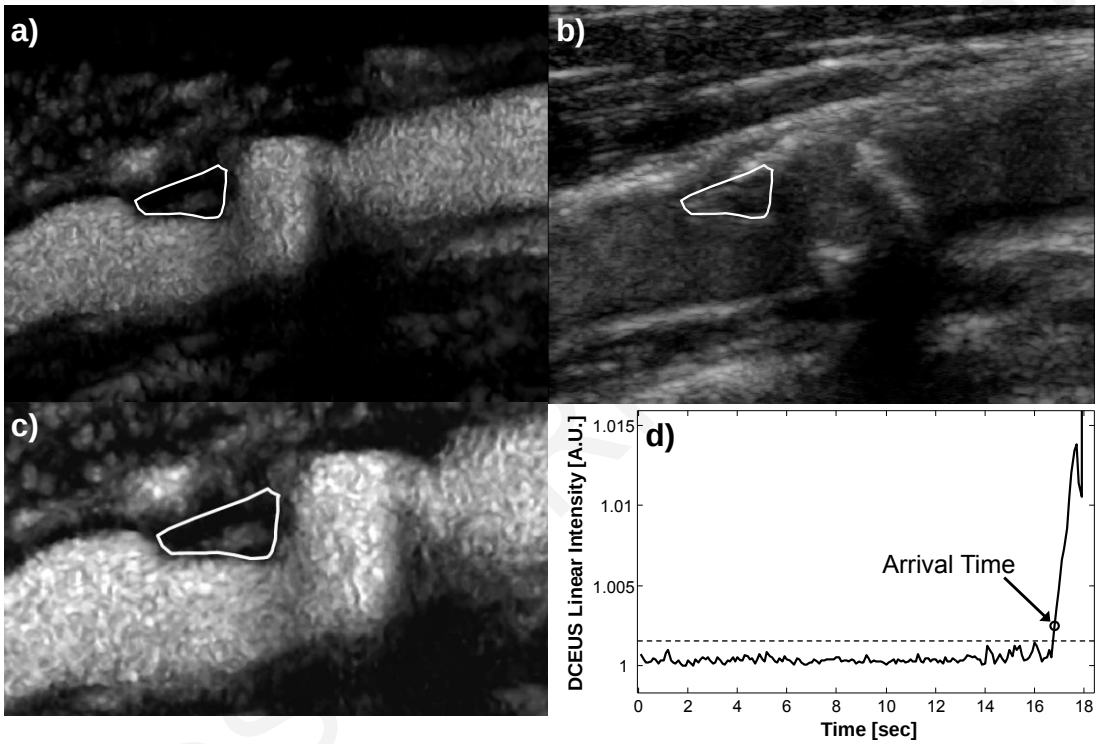

Figure 5-1: a) Contrast side of the dual-contrast imaging carotid plaque acquisition with the carotid plaque delineated using QLAB's polygon tool to draw the region of interest (ROI), b) tissue side of the dual-contrast imaging carotid plaque acquisition and c) zoom-in on the carotid plaque on the contrast image with the upper level of the contrast window decreased to enhance the low intensity signal within the plaque. d) Detection of microbubble arrival in carotid atherosclerotic plaques. The arrival time was defined as the first time instance at which the mean linear intensity value from within the ROI encompassing the plaque exceeds the maximum value present in the background noise (dashed line).

For the first stage of the analysis the DICOM files of the acquired DCEUS loops were transferred to QLAB. A region of interest (ROI) was drawn around the plaque using the ROI polygon tool of QLAB's quantification suite (Figure 5-1a-c). Caution was taken not to include any nearby tissue or arterial lumen in the ROI. Frames in which there was an excessive amount of out of plane motion were manually removed. In-plane motion was treated with the motion compensation tool of QLAB. Manual corrections in the position of the ROI were also performed as a final step in ensuring that the ROI encompassed only the

plaque. The steps described are crucial in the correct quantification of the loops since the low intensity microflow signal within the plaque can be contaminated by high intensity signal from within the lumen and the surrounding tissue, and thus introducing errors in the quantification results.

The second stage of the quantitative DCEUS analysis was performed in MATLAB. The DCEUS loop image data were imported into MATLAB. For each loop, the ROI was reconstructed in MATLAB using the coordinates of the vertices of QLAB's polygon ROI. The coordinates of the polygon vertices were imported into MATLAB from the "parameters.xml" file, as well as the 2D translation values from the motion compensation, the rejected frame indices and the time intensity curve (TIC) of the ROI.

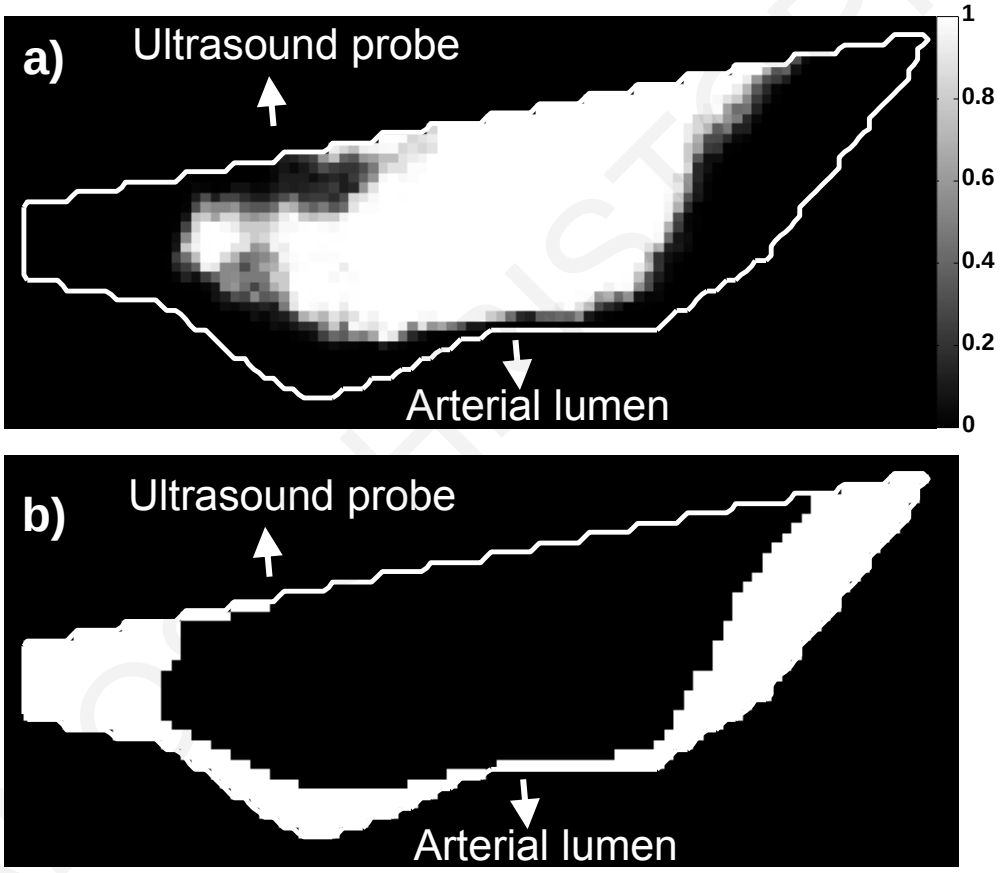

Figure 5-2: Results of dynamic contrast-enhanced ultrasound (DCEUS) quantification analysis of a near-wall carotid plaque (delineated with white line) from a symptomatic patient. a) Parametric map of p-values from the two sample Kolmogorov-Smirnoff test used to detect intraplaque perfusion is shown. b) A threshold of 0.001 is used on the p-value parametric map to differentiate between perfused (p-value<0.001) and non-perfused pixels (p-value≥0.001). In this symptomatic patient the plaque had 32% perfusion coverage.

The first step in the MATLAB quantification analysis was to determine the arrival time of the contrast agent in the ROI. The arrival time was defined as the first time instance at which the TIC intensity value exceeds the maximum value of the background noise recorded (Figure 5-1d). The ROI was then applied as a binary mask on each valid frame of the DCEUS loop. At each pixel location within the ROI the distribution of image intensity

values recorded before the arrival of the contrast agent in the ROI were considered to be a sample from the noise distribution. For each pixel the noise distribution sample was compared to the distribution of image intensity values after the arrival of the contrast agent. The comparison of the two samples was performed using the two sample Kolmogorov-Smirnoff test at a significance level of 0.1%. If the two samples differed significantly (i.e. p-value<0.001) then that pixel location was considered to be perfused, since the distribution of image intensity values after the arrival of the contrast agent differs significantly from that of noise. The number of pixels in the ROI that were perfused was divided by the total number of pixels in the ROI to evaluate the percent perfusion coverage of the plaque (Figure 5-2).

5.2.5 Statistical analysis

The qualitative and quantitative analysis was performed by a vascular surgery research fellow and repeated by a Professor of Bioengineering with more than 20 years of experience in clinical ultrasound research. Inter-observer agreement was calculated using the intraclass correlation coefficient and Cohen's kappa for the quantitative and qualitative analysis respectively. The qualitative scores reported were mutually agreed upon following the inter-observer agreement analysis. From the quantitative analysis the mean of the percent perfusion coverage calculated by the two observers was reported.

Differences in the qualitative scores between asymptomatic and symptomatic patients were tested using Fisher's exact test. The Mann-Whitney U test was used to calculate differences in the percent perfusion coverage of the carotid atherosclerotic plaques between symptomatic and asymptomatic patients. Furthermore the results from the quantitative analysis were placed into two groups based on their qualitative score. The differences between the two groups were compared using the unpaired two sample t-test. The significance level for the statistical tests was set at a p-value of 0.05. The data were analyzed using the R programming language (R Foundation for Statistical Computing, Vienna, Austria).

5.3 Results

5.3.1 Qualitative analysis

A substantial degree of agreement was found between the two observers with a calculated Cohen's kappa of 0.703 ($p<0.05$). The results of the qualitative analysis show that 12 (77%) out of the15 asymptomatic patients exhibited greater than 50% perfusion

coverage of the carotid atherosclerotic plaques compared with 4 (33%) out of the 12 symptomatic patients ($P < 0.05$) (Figure 5-3).

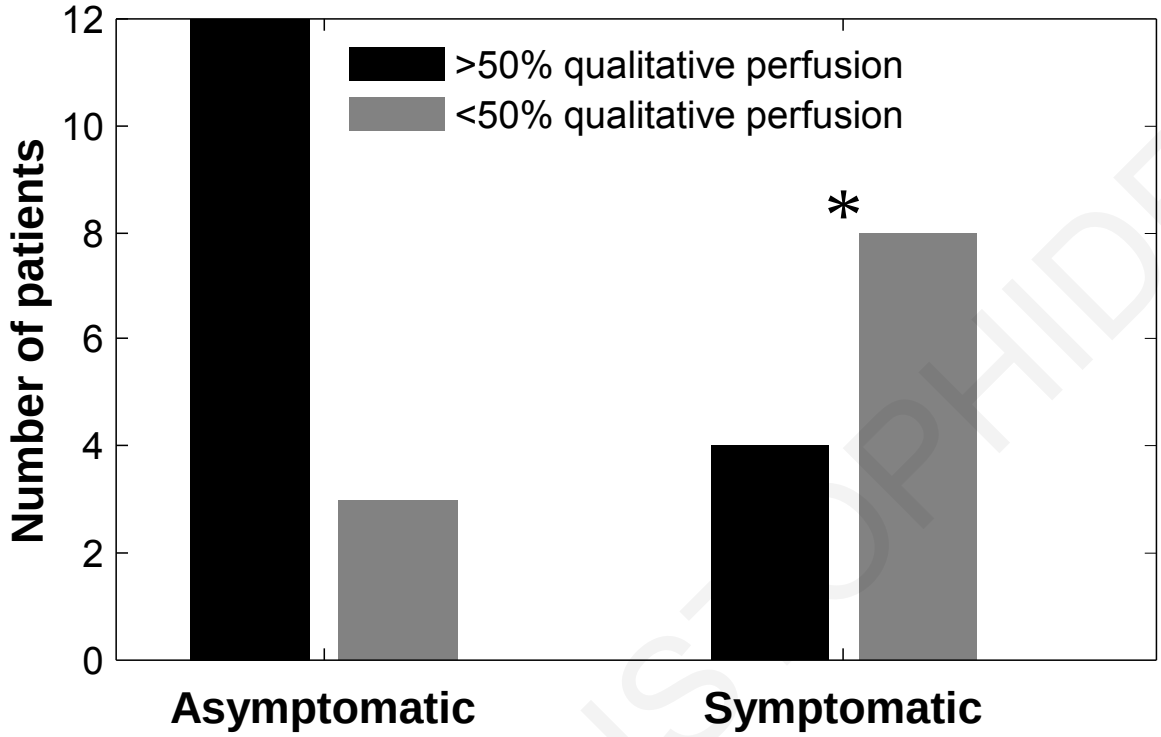

Figure 5-3: Bar plot of the results from the qualitative analysis of the carotid plaque DCEUS scans. Symptomatic patients showed significantly higher proportions of plaques graded as having moving microbubbles in less than 50% of their area. * = P≤0.05

5.3.2 Quantitative analysis

Strong inter-observer agreement was demonstrated for the quantification analysis with a calculated intraclass correlation coefficient of 0.831(95% confidence interval, 0.662-0.919). The values of percent perfusion coverage for symptomatic patients concentrated in their majority (8/12) below 50% with 4/12 of symptomatic patients exhibiting percent perfusion coverage of over 80%. The percent perfusion coverage of plaques in asymptomatic patients was evenly spread between 40-100%, with only one of the asymptomatic plaques having percent perfusion coverage less than 50% (Figure 5-4). The results of the quantitative analysis were compared with the qualitative visual scores (Figure 5-5) and a significant increase of the percent perfusion coverage was demonstrated for the plaques that received a qualitative score of higher than 50% perfusion coverage ($p<0.05$).

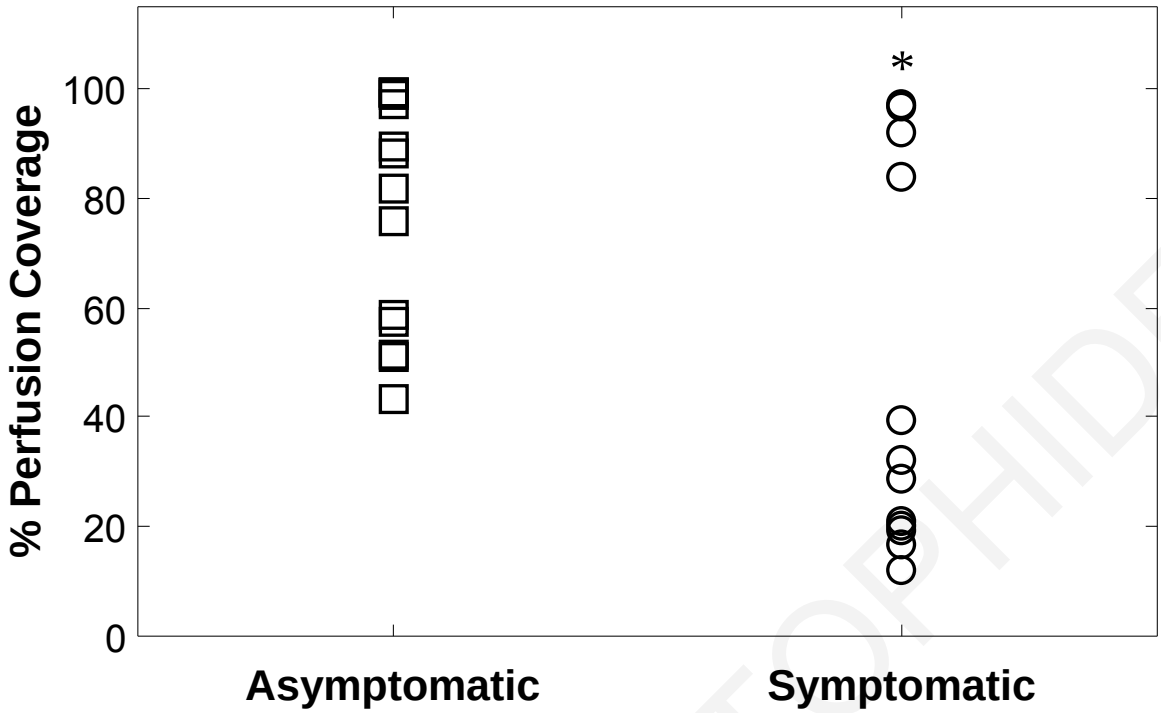

Figure 5-4: Scatter plot of percentage perfusion coverage of plaques between symptomatic and asymptomatic patients. Plaques in asymptomatic patients have percentage perfusion coverage values covering the range between 40 to 100% whereas the majority of plaques from symptomatic patients (8/12) have less than 50% perfusion coverage. * = P≤0.05.

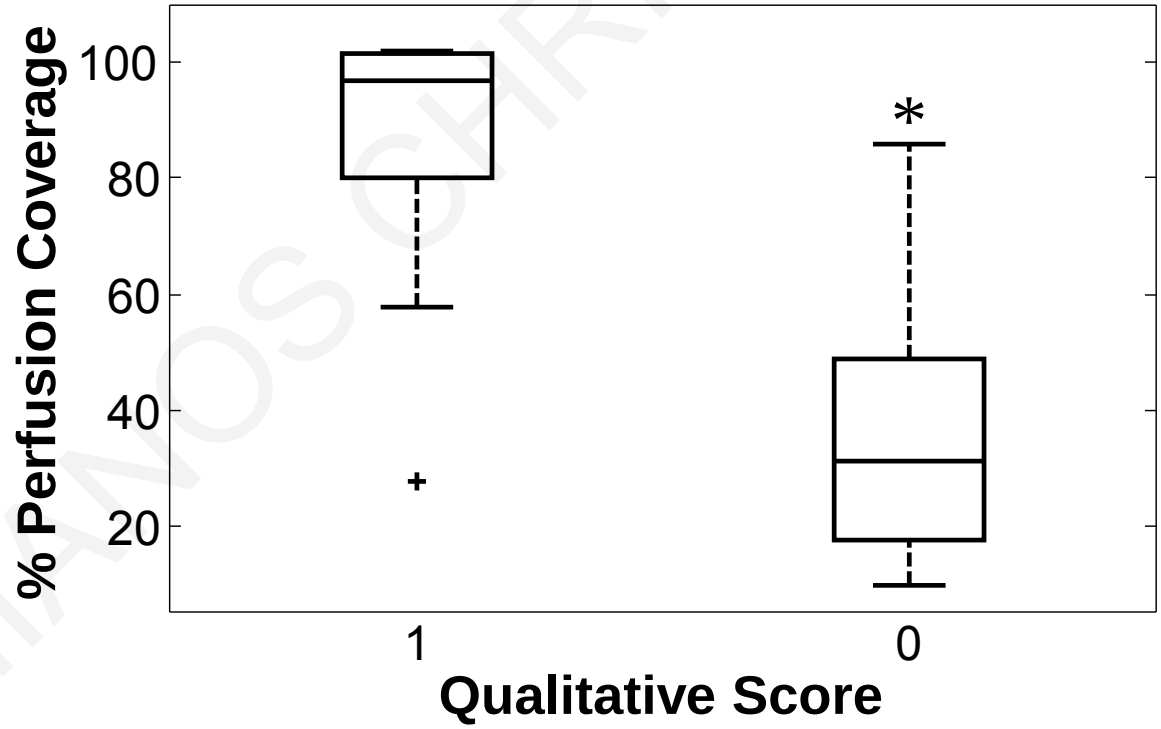

Figure 5-5: Boxplots of the percentage perfusion coverage of carotid plaques grouped according to results of the qualitative analysis. Carotid atherosclerotic plaques that received a qualitative score of 1 where considered to be perfused in more than 50% of their area. The percentage perfusion coverage values where significantly higher in the group with a qualitative score of 1 compared with the values that received a qualitative score of 0. * = P≤0.05, Power=1.0.

5.4 Discussion

Both the qualitative and quantitative analysis of this study found that carotid atherosclerotic plaques from symptomatic patients exhibit significantly less perfused area compared with asymptomatic patients. The results of the qualitative and quantitative analysis were examined for inter-observer variability with correlation scores demonstrating substantial and strong agreement respectively. In addition the results of the quantitative analysis where validated against the qualitative scores.

Akkus et al[10] performed a DCEUS quantitative study of 45 plaques using an adaptive image threshold technique to detect the perfusion within the plaques. The patients participating in the study presented with symptomatic stenosis and they exhibited mean percentage perfusion coverage of 32.7% ± 24.7% (mean ± standard deviation). In the current study the mean percentage perfusion coverage for symptomatic patients was 47.4% ±34.9% (N=12) compared with 80.1% ±21.2% for the asymptomatic patients (N=15). Using an unpaired t-test no significant difference can be shown between the symptomatic patients from Akkus et al and this study ($p=0.192$). On the contrary when comparing the results of the asymptomatic patients of the current study and the mean percentage coverage reported by Akkus et al a significant difference can be demonstrated ($p<0.001$). The agreement of the results for the symptomatic patients between our study and the one by Akkus further amplifies our finding that carotid plaques from symptomatic patients often have reduced perfusion coverage compared to asymptomatic patients.

In a quantitative DCEUS study by Hoogi et al[9] active contouring image segmentation[13] was used to detect the microflow within carotid plaques. Regions of contrast enhancement within a plaque were considered areas of neovascularization. Strong correlation was demonstrated between the ratio of intraplaque area neovascularization calculated using DCEUS and histology. No differences could be shown between the symptomatic and asymptomatic patients. Although this contradicts the findings of the current study there are several differences in the methodology and carotid plaque characteristics to be considered. The current study uses statistics to detect perfusion in carotid plaques whereas Hoogi et al utilizes image segmentation. In addition the ratio of intraplaque area neovascularization reported by Hoogi et al varies approximately between 0 and 20% whereas in the present study the percent perfusion coverage varies between 10 and 100%. The low percentage of the perfused plaque area reported by Hoogi et al also differs from the mean percent perfused area of 32.69% reported by Akkus et al and could

indicate that perhaps the plaques analyzed had a high content of intraplaque calcification or prior hemorrhage and thrombus formation.

Xiong et al[8] used an indicator dilution model to calculate the peak intensity (PI) in plaques and the ratio of the PI in plaques to the PI in the lumen of arteries. The study found that plaques from symptomatic patients exhibit more intense contrast agent enhancement than asymptomatic patients. The quantification method used in this study is different from the one was used by Xiong et al since we used pixel-by-pixel parametric imaging to calculate the percent perfusion coverage of the plaque. No relationship can be established between percent perfusion coverage and PI since high values of the PI could be originating from a very large signal in a small area within the plaque and do not represent the extent of perfusion within the whole of the plaque. Although indicator dilution models have been used in the quantification of liver lesion perfusion[14] and myocardial blood flow[15] the low flows observed in the plaques of this study does not satisfy the assumptions made by indicator dilution models[14], [16]–[19] and that is the reason why we have not used it. Furthermore Akkus et al[10] found very poor correlation between the PI metric used by Xiong et al and visual scores of intraplaque neovascularization prompting them to disregard any further consideration of this parameter.

DCEUS qualitative studies have shown a strong correlation between visual scores of enhanced plaque perfusion and predictors of plaque vulnerability. Staub et al[6] used a qualitative grading system to categorize carotid plaques as having no perfusion, moderate perfusion and extensive appearance of moving microbubbles. A significant correlation between plaque echolucency in B-mode and the qualitative DCEUS scores was established. Plaque echolucency in B-mode is a suggested predictor of cerebrovascular events[20], [21] and therefore of plaque vulnerability. In addition, in a study of 52 carotid plaques by Coli et al[7] a significant correlation was shown between DCEUS enhancement and microvessel density measured with histology.

Contrary to the qualitative DCEUS studies mentioned, this work does not aim to identify vulnerable plaques but to detect differences in the perfusion characteristics between plaques from symptomatic and asymptomatic patients. It is reasonable to expect that a group of asymptomatic patients will have plaques with a mixed of degree of vulnerability. This can be clearly seen from the 40-100% range of percentage perfusion coverage values for the asymptomatic patients in this study (Figure 5-4). Once a patient exhibits symptoms there is a high probability that a rupture event took place which could have disrupted the microvessel network which in turn may give rise to a reduced perfusion

of the plaque. The presence of large necrotic cores, thrombus and hemorrhage could also contribute to the reduced perfusion of plaques from symptomatic patients [22].

Although the statistical results of this study show that plaques from symptomatic patients to have significantly less perfusion compared with asymptomatic patients a close examination of the quantitative data (Figure 5-4) is needed. Whereas the symptomatic perfusion data are mostly concentrated below 50% (8/12) the remaining four plaques have perfusion coverage of more than 80%. The authors believe that these four cases are not necessarily outliers to the low percentage perfusion coverage distribution of symptomatic patients but could be vulnerable plaques with extensive neovascularization that have caused symptoms without their microvessel network being yet disrupted. Similarly, close examination of the perfusion of asymptomatic patients, shows that one had percent area less than 50%, and four 50-60% and the rest higher. It is possible that some of the asymptomatic patients with high degree of perfusion might develop symptoms in the future thus suggesting that they may be the ones with the vulnerable plaques. Similar conclusions may be drawn from the qualitative analysis in Figure 5-3.

Several limitations can be identified in the present study. Although the results are statistically significant further studies with a larger number of patients and a stricter classification of their symptom status will give more confidence in the findings and further progress the research towards identifying the characteristics of vulnerable plaques.

Furthermore the percent perfusion coverage calculated in the quantitative analysis of this study is representative of only a 2D slice through the plaque. Future volumetric 3D studies can provide additional insight into the perfusion patterns of vulnerable plaques and also increase sensitivity. In addition, in 2D DCEUS the plaque might not be perfectly centered on the elevation plane of the ultrasound probe or might be thin compared to the elevation plane thickness and signal from nearby lumen might be perceived as originating from within the plaque.

Inherent limitations to carotid plaque DCEUS include the presence of non-linear artefact[23], insufficient resolution and limited sensitivity in detecting the perfusion in the microscopic scale of plaque vasculature, signal saturation due to the large discrepancy in the image intensity between the lumen and the plaque, and the presence of non-linear signal cancellation artefacts (from the nonlinear pulsing schemes). These sources of uncertainty do not just affect the current study but are intrinsically present in all of the DCEUS studies done in the past too.

Another limitation is that the findings of the current study have not been verified against histology. Even though histological results were available for the symptomatic patients and a limited number of high risk asymptomatic patients there was no ethical justification for performing surgery on the majority of asymptomatic patients. Thus any comparison of the results from the DCEUS analysis with histology would be biased. Furthermore the current study aims to identify differences in the extend of carotid plaque perfusion based on the appearance of symptoms rather than performing a direct comparison with histology.

In conclusion, a new metric of plaque neovascularization, percent plaque perfused area, was developed and measured in a group of both symptomatic and asymptomatic patients. The new metric is more appropriate for plaque perfusion quantification than other metrics based on bolus wash-in/washout kinetics. The findings of our study show that plaques in patients that already demonstrated symptoms had reduced perfused area, possibly due to intraplaque hemorrhage, large necrotic cores and thrombus formation. The opposite was observed in asymptomatic patients and their plaques had increased perfused area. The increased perfusion in asymptomatic patients is suggesting that some of these plaques may be vulnerable. Thus, a more appropriate study in the future would be one in which plaques are identified in asymptomatic patients and evaluated through a period of time in order to better understand and monitor plaque microvessel flow progression.

References

[1] D. Lloyd-Jones et al., "Heart disease and stroke statistics--2010 update: a report from the American Heart Association.," *Circulation*, vol. 121, no. 7, pp. e46–e215, Feb. 2010.

[2] J. J. Guilbert, "The world health report 2002 - reducing risks, promoting healthy life.," *Educ. Health (Abingdon).*, vol. 16, no. 2, p. 230, Jul. 2003.

[3] S. Chaturvedi, A. Bruno, T. Feasby, R. Holloway, O. Benavente, S. N. Cohen, R. Cote, D. Hess, J. Saver, J. D. Spence, B. Stern, and J. Wilterdink, "Carotid endarterectomy--an evidence-based review: report of the Therapeutics and Technology Assessment Subcommittee of the American Academy of Neurology.," *Neurology*, vol. 65, no. 6, pp. 794–801, Sep. 2005.

[4] P. R. Moreno, K. R. Purushothaman, V. Fuster, D. Echeverri, H. Truszczynska, S. K. Sharma, J. J. Badimon, and W. N. O'Connor, "Plaque neovascularization is increased in ruptured atherosclerotic lesions of human aorta: implications for plaque vulnerability.," *Circulation*, vol. 110, no. 14, pp. 2032–8, Oct. 2004.

[5] M. J. McCarthy, I. M. Loftus, M. M. Thompson, L. Jones, N. J. London, P. R. Bell, A. R. Naylor, and N. P. Brindle, "Angiogenesis and the atherosclerotic carotid plaque: an association between symptomatology and plaque morphology.," *J. Vasc. Surg.*, vol. 30, no. 2, pp. 261–8, Aug. 1999.

[6] D. Staub, S. Partovi, A. F. L. Schinkel, B. Coll, H. Uthoff, M. Aschwanden, K. A. Jaeger, and S. B. Feinstein, "Correlation of carotid artery atherosclerotic lesion echogenicity and severity at standard US with intraplaque neovascularization detected at contrast-enhanced US.," *Radiology*, vol. 258, no. 2, pp. 618–26, Feb. 2011.

[7] S. Coli, M. Magnoni, G. Sangiorgi, M. M. Marrocco-Trischitta, G. Melisurgo, A. Mauriello, L. Spagnoli, R. Chiesa, D. Cianflone, and A. Maseri, "Contrast-enhanced ultrasound imaging of intraplaque neovascularization in carotid arteries: correlation with histology and plaque echogenicity.," *J. Am. Coll. Cardiol.*, vol. 52, no. 3, pp. 223–30, Jul. 2008.

[8] L. Xiong, Y.-B. Deng, Y. Zhu, Y.-N. Liu, and X.-J. Bi, "Correlation of carotid plaque neovascularization detected by using contrast-enhanced US with clinical symptoms.," *Radiology*, vol. 251, no. 2, pp. 583–9, May 2009.

[9] A. Hoogi, D. Adam, A. Hoffman, H. Kerner, S. Reisner, and D. Gaitini, "Carotid plaque vulnerability: Quantification of neovascularization on contrast-enhanced ultrasound with histopathologic correlation," *Am. J. Roentgenol.*, vol. 196, no. 2, pp. 431–436, 2011.

[10] Z. Akkus, A. Hoogi, G. Renaud, S. C. H. van den Oord, G. L. ten Kate, A. F. L. Schinkel, D. Adam, N. de Jong, A. F. W. van der Steen, and J. G. Bosch, "New Quantification Methods for Carotid Intra-plaque Neovascularization Using Contrast-Enhanced Ultrasound," *Ultrasound Med. Biol.*, vol. 40, no. 1, pp. 25–36, 2014.

[11] C. P. Oates, A. R. Naylor, T. Hartshorne, S. M. Charles, T. Fail, K. Humphries, M. Aslam, and P. Khodabakhsh, "Joint recommendations for reporting carotid ultrasound investigations in the United Kingdom.," *Eur. J. Vasc. Endovasc. Surg.*, vol. 37, no. 3, pp. 251–61, Mar. 2009.

[12] D. Christofides, E. Leen, and M. Averkiou, "Automatic respiratory gating for contrast ultrasound evaluation of liver lesions.," *IEEE Trans. Ultrason. Ferroelectr. Freq. Control*, vol. 61, no. 1, pp. 25–32, Jan. 2014.

[13] T. F. Chan and L. A. Vese, "Active contours without edges," *IEEE Trans. Image Process.*, vol. 10, no. 2, pp. 266–277, 2001.

[14] C. Strouthos, M. Lampaskis, V. Sboros, A. McNeilly, and M. Averkiou, "Indicator dilution models for the quantification of microvascular blood flow with bolus administration of ultrasound contrast agents.," *IEEE Trans. Ultrason. Ferroelectr. Freq. Control*, vol. 57, no. 6, pp. 1296–310, Jun. 2010.

[15] S. Kaul, P. Kelly, J. D. Oliner, W. P. Glasheen, M. W. Keller, and D. D. Watson, "Assessment of regional myocardial blood flow with myocardial contrast two-dimensional echocardiography.," *J. Am. Coll. Cardiol.*, vol. 13, no. 2, pp. 468–82, Feb. 1989.

[16] M. Averkiou, M. Lampaskis, K. Kyriakopoulou, D. Skarlos, G. Klouvas, C. Strouthos, and E. Leen, "Quantification of tumor microvascularity with respiratory gated contrast enhanced ultrasound for monitoring therapy.," *Ultrasound Med. Biol.*, vol. 36, no. 1, pp. 68–77, Jan. 2010.

[17] C. F. Dietrich, M. A. Averkiou, J.-M. Correas, N. Lassau, E. Leen, and F. Piscaglia, "An EFSUMB introduction into Dynamic Contrast-Enhanced Ultrasound (DCE-US) for quantification of tumour perfusion.," *Ultraschall Med.*, vol. 33, no. 4, pp. 344–51, Aug. 2012.

[18] T. P. Gauthier, A. Muhammad, H. S. Wasan, P. D. Abel, and E. L. S. Leen, "Reproducibility of quantitative assessment of altered hepatic hemodynamics with dynamic contrast-enhanced ultrasound.," *J. Ultrasound Med.*, vol. 31, no. 9, pp. 1413–20, Sep. 2012.

[19] N. Lassau, S. Koscielny, L. Chami, M. Chebil, B. Benatsou, A. Roche, M. Ducreux, D. Malka, and V. Boige, "Advanced hepatocellular carcinoma: early evaluation of response to bevacizumab therapy at dynamic contrast-enhanced US with quantification--preliminary results.," *Radiology*, vol. 258, no. 1, pp. 291–300, Jan. 2011.

[20] E. B. Mathiesen, K. H. Bønaa, and O. Joakimsen, "Echolucent plaques are associated with high risk of ischemic cerebrovascular events in carotid stenosis: the tromsø study.," *Circulation*, vol. 103, no. 17, pp. 2171–2175, 2001.

[21] M. L. Grønholdt, B. G. Nordestgaard, T. V Schroeder, S. Vorstrup, and H. Sillesen, "Ultrasonic echolucent carotid plaques predict future strokes.," 2001.

[22] A. N. Nicolaides, *Ultrasound and carotid bifurcation atherosclerosis*. London; New York: Springer-Verlag London Ltd., 2012.

[23] A. Thapar, J. Shalhoub, M. Averkiou, C. Mannaris, A. H. Davies, and E. L. S. Leen, "Dose-dependent artifact in the far wall of the carotid artery at dynamic contrast-enhanced US.," Radiology, vol. 262, no. 2, pp. 672–9, Feb. 2012

6

Summary and future directions

6.1 Summary

Dynamic contrast enhanced ultrasound (DCEUS) can have enormous clinical potential in analyzing and visualizing the dynamics of tissue perfusion. However the necessary tools need to be developed to enable clinicians to perform reproducible, reliable and quantitative analysis of DCEUS in routine clinical practice. The work in this thesis was motivated by the need for algorithms and methods in order to remove noise and isolate useful information of quantitative DCEUS. Challenges in quantifying the perfusion in tissues with a high amount of blood flow using indicator dilution models were addressed in Chapters 2-4 with the use of an automatic respiratory gating (ARG) algorithm developed for liver lesion DCEUS quantification. Indicator dilution models cannot be applied in cases of low amount of blood flow for that reason a method for calculating the percent perfusion coverage of carotid atherosclerotic plaques was developed in Chapter 5.

In Chapter 2 the technical aspects of the ARG algorithm were presented. In essence the ARG algorithm fully automates the manual respiratory gating process described by Averkiou et al. [1]. Instead of relying on an observer to identify the diaphragm or other moving bright reflectors the ARG algorithm made use of frame subtraction [2] to detect moving structures in the tissue loop of a dual-contrast imaging acquisition. An observer would also be able to avoid selecting moving structures that are not related to respiration like vessel movement due to the pulsating blood pressure. The ARG algorithm analyzes the motion from each moving structure detected using frequency domain analysis and the prior knowledge that the frequency of respiration is between 0.1-0.5Hz [3].

Since the ARG algorithm was designed with the aim to be used clinically, computational speed was an important technical characteristic that needed to be taken into account. The ARG algorithm developed in this thesis can process 100 frames in less than a second. For a 2 minute clinical liver lesion dual-contrast imaging acquisition at a frame rate of 8Hz the ARG algorithm can perform respiratory gating in less than 9 seconds. This calculation time compares favorably with the current solutions proposed in the literature and is 6 times faster than the second fastest reported algorithm [4].

The ARG algorithm presented can readily remove out-of-plane as well as in-plane respiratory motion. Removing out-of-plane motion can be a challenge especially for motion compensation schemes that make use of image registration since out-of-plane respiratory motion can cause anatomical landmarks to move completely outside the imaging plane causing failures in the registration process [5], [6]. Zhang et al. [7]

implemented a scheme by which image registration was used for the rejection of frames with excessive out-of-plane motion. However the extra steps implemented by Zhang et al. in order to remove out-of-plane motion resulted in a clinically unacceptable computational time of 3 minutes for 100 frames.

Respiratory motion correction algorithms based on independent [8] and principal [4] component analysis can efficiently remove out-of-plane motion as well as in-plane motion but allow only for the end-of-respiration breathing cycle phases to be extracted. This can cause problems in liver lesion DCEUS quantification since a crucial step of the quantification process requires the operator to choose an optimal frame to delineate the lesion in order to extract a time intensity curve representative of the lesion's perfusion. If this optimal frame is not part of the extracted loop then the DCEUS quantification may not be as reliable or fail completely if the lesion is not present on the imaging plane due to out-of-plane motion. The ARG algorithm presented in Chapter 2 allowed for the user to choose the optimal frame to perform the quantification and used that frame as the "trigger" frame to extract the ARG-processed loop. This allowed not only for the optimal frame to be present in the extracted loop but to also be the reference by which respiratory gating was performed.

Chapter 3 assessed the impact of the ARG algorithm on clinical liver lesion DCEUS quantification. The main hypothesis tested in Chapter 3 is whether there is a varying degree by which respiration affects DCEUS quantification. It is likely that the use of ARG offers marginal, if any benefit at all, to liver lesion DCEUS quantification if respiration induces minimal movement on a lesion. Respiration amplitude (*RA*) was developed and introduced as a metric by which to quantify the effect of respiration on liver lesion DCEUS. To the author's knowledge no other study has quantified the effect of respiration on liver lesion DCEUS quantification.

It is expected that as *RA* increases the accuracy of liver lesion DCEUS quantification decreases. This was demonstrated by comparing the *RA* with the quality of fit of the lognormal indicator dilution model [9] on liver lesion time intensity curves (R^2_{LN}). As expected with the increase in *RA* the quality of fit decreased with a strong linear correlation of -0.96, whereas with the use of ARG the correlation was reduced by 33%. Overall the quality of fit increased significantly with the use of ARG with 88% of the lesion time intensity curves exhibiting an R^2_{LN} of greater than 0.8 compared with only 32% without ARG. Furthermore the use of ARG had a significant impact on the quantification parameters of rise time (RT), peak intensity (PI) and area under the curve (AUC). However

this was not the case for liver lesion time intensity curves with an *RA* of less than 1.5 with ARG affecting none of the quantification parameters. This further demonstrated the need of *RA* in the analysis of respiratory motion compensation algorithms before any conclusions can be reached on their clinical impact.

The need of determining the absolute decrease in accuracy of liver lesion DCEUS quantification in the presence of respiratory motion was addressed in Chapter 4. Although metrics like the R^2_{LN} and *RA* are useful in analyzing the effect of the ARG algorithm on clinical data, it was impossible to quantify the exact impact of ARG since the true lesion perfusion was not known. A respiratory motion simulation model (RMSM) was constructed from clinical data to formulate the perfusion and respiratory kinetics of the model. The perfusion of a virtual spherical lesion inside of a cubic liver parenchyma was determined by a lognormal normal indicator dilution model derived from clinical averages of RT, MTT and PI. The virtual lesion was captured on the imaging frame as a disk with variable location and radius due to in-plane and out-of-plane respiratory motion respectively.

The RMSM showed that the ARG algorithm reduced the maximum percentage error in the quantification parameters caused by out-of-plane motion almost nine-fold from 27.3% to 3.1%. A decrease of the maximum percentage error from 32.2% to 6.2% was calculated in the case of in-plane respiratory motion. The clinical relevance of the RMSM was demonstrated by comparing the relationship between the R^2_{LN} and *RA* derived from the RMSM and clinical liver lesion DCEUS. The slope of the linear regression for the clinical data increased from -0.33 to -0.12 with the use of ARG compared to a similar increase of -0.40 to -0.14 for the RMSM.

In addition to investigating the impact of respiration, the RMSM was also used for the analysis of the effect of multiplicative noise on liver lesion DCEUS quantification. The gamma distribution multiplicative noise model proposed by Barrois et al. [10] was used to introduce noise onto the RMSM. It was shown in Chapter 4 that the multiplicative noise model increased the error introduced from respiratory motion by 50% for the amplitude parameters of AUC and PI; whereas no increase in error was demonstrated for the RT and MTT. However the increase in the error of the amplitude quantification parameters was theoretically predicted using the moments of the gamma distribution to be directly proportional to the true values of the parameters.

Finally in Chapter 5 a novel method was introduced in quantifying the percent perfusion coverage of the microflow within carotid atherosclerotic plaques. The DCEUS

quantitative method was verified using visual qualitative scores of the extent of moving microbubbles within the plaque. The area of perfusion within carotid plaques was determined to be significantly less in symptomatic patients compared to asymptomatic using both qualitative and quantitative DCEUS. Furthermore the results of the study were tested for inter-observer variability demonstrating strong agreement for the qualitative and quantitative analysis. The values of percent perfusion coverage of Chapter 5 were in agreement with results reported by Akkus et al. [11] for patients with symptomatic stenosis, supporting the validity of the analysis performed in this thesis.

An important conclusion drawn from Chapter 5 was that the comparison of the extent of plaque perfusion between symptomatic and asymptomatic patients does not provide a definitive answer to the perfusion characteristics of vulnerable carotid plaques. The results indicate that as the disease progresses in asymptomatic patients the perfusion coverage of the plaques will increase until symptoms occur. Symptoms are associated with the presence of hemorrhage, large necrotic cores and thrombus in the carotid plaques [13] that explains the reduced perfusion coverage observed in symptomatic patients. Additional work is needed both in terms of validating tools for carotid plaque microflow quantification and in the design of new clinical studies. In order to characterize vulnerable plaques a clinical study would need to monitor the carotid plaque microflow in asymptomatic patients prospectively for a period of time to identify the microflow patterns that can lead to symptoms.

6.2 Conclusion

In his bestselling book "*The Signal and the Noise*" Nate Silver says that "*The signal is the truth. The noise is what distracts us from the truth*."[14]. The methods and algorithms developed in this thesis were aimed to remove noise from liver lesion and carotid plaque DCEUS quantification so that the true perfusion values could be quantified. In the case of liver lesion DCEUS the ARG algorithm developed has been shown to significantly reduce the noise imparted by respiration onto lesion time intensity curves. The reduction in respiration noise resulted in greater accuracy for liver lesion DCEUS quantification demonstrated using both clinical data and the RMSM. In addition the ARG algorithm was fast, easy-to-implement and allowed the user to choose the breathing cycle phase to be extracted. The algorithm for detecting the percent perfusion coverage of the carotid plaques was able to show distinct perfusion characteristics between symptomatic and asymptomatic patients. Furthermore the results from the algorithm were validated

using qualitative visual scores. Although overall the results were inconclusive in answering the crucial question whether quantitative DCEUS can predict vulnerable carotid plaques they do provide the tools and insight that is crucial in the design of future studies in answering this question.

6.3 List of Original Contributions

- In this thesis advanced algorithms and methods were designed that contribute significantly to the reliability of liver lesion and carotid plaque DCEUS quantification. Specifically a novel ARG algorithm was developed that overcame the limitations of the algorithms presented in the literature in terms of computational speed, ease of implementation, and efficiency in removing both in-plane and out-of-plane respiratory motion.

- The *RA* was introduced as an important metric for quantifying the amount of respiratory motion present in liver lesion DCEUS acquisitions. The relationship of the quality of fit of the lognormal indicator dilution model onto liver lesion time intensity curves and the *RA* was used to demonstrate the efficiency of the ARG algorithm in significantly reducing respiratory motion across the range of *RA* observed in the clinic.

- A RMSM was constructed to overcome the limitation of establishing the true perfusion characteristics of liver lesions in the clinic. The RMSM allowed for the absolute determination of the efficiency of the ARG algorithm in improving the accuracy of DCEUS quantification parameters in the presence of respiratory motion. Furthermore the clinical relevance of the RMSM was validated by comparing the relationship between *RA* and R^2_{LN} extracted from the simulation and clinical data.

- The effect of multiplicative noise on liver lesion DCEUS quantification was also investigated using the RMSM. It was demonstrated that multiplicative noise had no impact on the time parameters of RT and MTT. However it was shown that it did affect the amplitude parameters of PI and AUC through a theoretically derived linear relationship.

- A novel algorithm was developed for the quantification of the extent of perfusion within carotid atherosclerotic plaques. The algorithm made use of statistics, image and

signal processing to remove sources of noise from carotid plaque DCEUS quantification and calculate the percent perfusion coverage. The results of the quantification method were verified against visual scores of the extent of plaque perfusion.

- Carotid plaque percent perfusion coverage scores were able to show a significant decrease in the extent of microflow in symptomatic patients compared to asymptomatic. The carotid plaque DCEUS quantification algorithm developed contributes to the limited number of studies in the literature and provides better understanding for the design of future clinical studies.

6.4 List of publications that resulted from this thesis

Patents

1. M. Averkiou and **D. Christofides**, "Eliminating motion effects in medical images caused by physiological function," World Intellectual Property Organization Patent Application #WO2014111860 A2. Publication Date: July 24, 2014. http://www.google.com/patents/WO2014111860A2?cl=en
2. M. Averkiou, E. Leen, and **D. Christofides**, "Evaluation of carotid plaque using contrast enhanced ultrasonic imaging," World Intellectual Property Organization Provisional Patent Application #PCT/IB2015/050452, 2015.

Journal Articles

1. **D. Christofides**, E. Leen, and M. Averkiou, "Automatic respiratory gating for contrast ultrasound evaluation of liver lesions," IEEE Trans. Ultrason. Ferroelectr. Freq. Control, vol. 61, no. 1, pp. 25–32, Jan. 2014. (front cover image)
2. **D. Christofides**, E. Leen, and M. A. Averkiou, "Improvement of the accuracy of liver lesion DCEUS quantification with the use of automatic respiratory gating," Eur. Radiol., [Epub ahead of print], 2015. http://link.springer.com/article/10.1007/s00330-015-3797-x
3. **D. Christofides,** E. Leen, and M. A. Averkiou, "Evaluation of the accuracy of liver lesion DCEUS quantification with respiratory gating," IEEE Trans. Med. Imaging, [Under Revision], Jul. 2015

4. **D. Christofides**, B. Dharmarajah, A. Davies, A. Nicolaides, E. Leen and M. Averkiou, "Carotid atherosclerotic plaque perfusion of symptomatic and asymptomatic patients with DCEUS," European Radiology, [Submitted], Jul. 2015

Conference Proceedings

1. **D. Christofides**, E. Leen, and M. Averkiou, "Automatic respiratory motion gating for the quantification of liver therapy monitoring," in 18th European Symposium on Ultrasound Contrast Imaging, 2013.
2. **D. Christofides**, E. Leen, and M. Averkiou, "Automatic respiratory gating for perfusion quantification of DCEUS," in Joint IEEE UFFC, EFTF and PFM Symposium, 2013.
3. **D. Christofides**, E. Leen, and M. A. Averkiou, "Automatic respiratory gating for the quantification of perfusion of liver metastasis with DCEUS," in 99th Annual Meeting of the Radiological Society of North America, 2013.
4. M. L. Izamis, C. Keravnou, **D. Christofides**, and M. Averkiou, "Quantification of liver perfusion is a sensitive approach to non-invasive evaluation of donor liver viability," in Annual Meeting of the American Association for the Study of Liver Diseases, 2013.
5. M. L. Izamis, C. Keravnou, **D. Christofides**, and M. A. Averkiou, "Basic bolus kinetics explored in an ex vivo liver machine perfusion model," in 19th European Symposium on Ultrasound Contrast Imaging, 2014.
6. **D. Christofides**, E. Leen, and M. Averkiou, "Improvement of accuracy of liver lesion DCEUS quantification using automatic respiratory gating," in 19th European Symposium on Ultrasound Contrast Imaging, 2014.
7. M. Averkiou, **D. Christofides**, B. Dharmarajah, A. Thapar, A. Davies, and E. Leen, "Evaluation of carotid plaque perfusion using DCEUS," in 19th European Symposium on Ultrasound Contrast Imaging, 2014.
8. M. Averkiou, **D. Christofides**, and P. Polyviou, "Ultrasound and microbubbles for monitoring therapies targeting tumor vascularity," in 1st Cyprus Interdisciplinary Congress on Oncology, 2014.

6.5 Acknowledgements

I thankfully acknowledge the funding sources that made my Ph.D. work possible.

- The University of Cyprus funded my work from the "AXMUS" and "SONODRUGS" (EU's Seventh Framework Program, FP7) research programs.

- I received funding from the Republic of Cyprus Research Promotion Foundation through the Bubble Liver research program (Project: DIDAKTOR/ 0311/78).
- Philips (Bothell, WA, USA) made their iU22 scanner and QLAB software available for measurements and analysis.
- The Cyprus State Scholarship Foundation for providing me with a three-year academic scholarship grant.

References

[1] M. Averkiou, M. Lampaskis, K. Kyriakopoulou, D. Skarlos, G. Klouvas, C. Strouthos, and E. Leen, "Quantification of Tumor Microvascularity with Respiratory Gated Contrast Enhanced Ultrasound for Monitoring Therapy," *Ultrasound Med. Biol.*, vol. 36, no. 1, pp. 68–77, 2010.

[2] A. Jain, *Fundamentals of Digital Image Processing*. Englewood Cliffs, NJ: Prentice-Hall, 1989.

[3] S. Fleming, M. Thompson, R. Stevens, C. Heneghan, A. Plüddemann, I. MacOnochie, L. Tarassenko, and D. Mant, "Normal ranges of heart rate and respiratory rate in children from birth to 18 years of age: A systematic review of observational studies," *Lancet*, vol. 377, no. 9770, pp. 1011–1018, 2011.

[4] S. Mulé, N. Kachenoura, O. Lucidarme, A. De Oliveira, C. Pellot-Barakat, A. Herment, and F. Frouin, "An automatic respiratory gating method for the improvement of microcirculation evaluation: application to contrast-enhanced ultrasound studies of focal liver lesions.," *Phys. Med. Biol.*, vol. 56, no. 16, pp. 5153–5165, 2011.

[5] N. Rognin, R. Campos, J. Thiran, T. Messager, P. Broillet, P. Frinking, M. Mercier, and M. Arditi, "A new approach for automatic motion compensation for improved estimation of perfusion quantification parameters in ultrasound imaging," in *Proceedings of the 8th French Conference on Acoustics*, 2006, pp. 61–65.

[6] N. G. Rognin, M. Arditi, L. Mercier, P. J. A. Peter, M. Schneider, G. Perrenoud, A. Anaye, J. Y. Meuwly, and F. Tranquart, "Parametric imaging for characterizing focal liver lesions in contrast-enhanced ultrasound," *IEEE Trans. Ultrason. Ferroelectr. Freq. Control*, vol. 57, no. 11, pp. 2503–2511, 2010.

[7] J. Zhang, M. Ding, F. Meng, M. Yuchi, and X. Zhang, "Respiratory motion correction in free-breathing ultrasound image sequence for quantification of hepatic perfusion," *Medical Physics*, vol. 38, no. 8. p. 4737, 2011.

[8] G. Renault, F. Tranquart, V. Perlbarg, A. Bleuzen, A. Herment, and F. Frouin, "A posteriori respiratory gating in contrast ultrasound for assessment of hepatic perfusion.," *Phys. Med. Biol.*, vol. 50, no. 19, pp. 4465–4480, 2005.

[9] C. Strouthos, M. Lampaskis, V. Sboros, A. Mcneilly, and M. Averkiou, "Indicator dilution models for the quantification of microvascular blood flow with bolus administration of ultrasound contrast agents," *IEEE Trans. Ultrason. Ferroelectr. Freq. Control*, vol. 57, no. 6, pp. 1296–1310, 2010.

[10] G. Barrois, A. Coron, T. Payen, A. Dizeux, and L. Bridal, "A Multiplicative Model for Improving Microvascular Flow Estimation in Dynamic Theory and Experimental Validation," *IEEE Trans. Ultrason. Ferroelectr. Freq. Control*, vol. 60, no. 11, pp. 2284–2294, 2013.

[11] Z. Akkus, A. Hoogi, G. Renaud, S. C. H. van den Oord, G. L. ten Kate, A. F. L. Schinkel, D. Adam, N. de Jong, A. F. W. van der Steen, and J. G. Bosch, "New Quantification Methods for Carotid Intra-plaque Neovascularization Using Contrast-Enhanced Ultrasound," *Ultrasound Med. Biol.*, vol. 40, no. 1, pp. 25–36, 2014.

[12] A. Hoogi, D. Adam, A. Hoffman, H. Kerner, S. Reisner, and D. Gaitini, "Carotid plaque vulnerability: Quantification of neovascularization on contrast-enhanced ultrasound with histopathologic correlation," *Am. J. Roentgenol.*, vol. 196, no. 2, pp. 431–436, 2011.

[13] A. N. Nicolaides, *Ultrasound and carotid bifurcation atherosclerosis*. London; New York: Springer-Verlag London Ltd., 2012.

[14] N. Silver, *The signal and the noise: why so many predictions fail - but some don't.* New York: Penguin Press, 2012.

Appendix 1

Eliminating motion effects in medical images caused by physiological function

This application claims the benefit of U.S. provisional application serial no. 61/753,898 filed January 17, 2013, which is incorporated herein by reference.

This invention relates to ultrasonic diagnostic imaging systems and, in particular, to the use of ultrasonic diagnostic imaging systems to assess the progress of therapeutic treatment of tumors.

International patent publication WO 2006/090309 (Bruce et al.) describes an ultrasonic imaging technique for detecting lesions in the liver by use of an ultrasonic contrast agent. A bolus of contrast agent is introduced into the body and the time of arrival of the contrast agent in the liver is detected. When a bolus of contrast agent travels through the blood vessels of the body and begins to appear at a specific organ or location in the body, the build-up of contrast in the images is termed the "wash-in" of the contrast agent. As the infusion of contrast agent plateaus at the location in the body and then declines as it is carried away from the location by the flow of blood, the decline is termed the "wash-out" of the contrast agent. In the aforementioned patent publication the inventors take advantage of the fact that the flow of blood to the liver comes from two sources, the hepatic artery and the portal vein. Since the flow of blood during the first, arterial phase of blood flow will perfuse HCC and metastatic liver lesions first, the inventors identify such lesions by detecting the times of arrival of contrast agent in the liver during the arterial and the later portal phase of blood flow. An area of early wash-in of contrast agent to the liver can be symptomatic of a lesion.

Once a lesion or metastasis has been identified by this and/or other means, a treatment regimen is generally prescribed by a physician. The therapy may

involve hyper-/hypothermia, cytotoxic chemotherapy, or anti-angiogenesis agents, for example. The therapy is usually not performed in a single session, but in several sessions over a period of weeks or months. At each therapy session it is generally desirable for a physician to assess the progress of the therapy to determine its effectiveness for the patient. The lesion or metastasis may be imaged diagnostically to see whether it is shrinking, for instance. But often the progress of treatment is slow and only small changes in the lesion or metastasis have occurred since the previous session. In such instances it is desirable to assess the progress of therapy quantitatively by measuring certain characteristics of the tumor. One such measure is the regression of tumor angiogenesis. As a lesion or metastasis shrinks with the necrosis of its cells, the microvasculature which developed to nourish the lesion will provide a smaller supply of blood for the lesion and may itself begin to shrink. One quantitative approach is to assess this regression of angiogenesis, the decline in performance of the lesion's microvasculature. A preferred technique for doing this is with a contrast agent which brightly illuminates the blood flow during the uptake of blood containing the agent, and the subsequent decline in brightness during the wash-out phase of the contrast agent. Measurement of the time-intensity curve of this reperfusion enables precise assessment of the success of the treatment therapy toward lesion necrosis. But the acquisition of the necessary image sequence of contrast agent wash-in and wash-out requires that the imaging probe steadily image the lesion in the image plane during the wash-in and wash-out period of the contrast agent, which can last for as long as 100 seconds or more. However, the liver is adjacent to the

diaphragm in the body, causing the patient's respiratory motion to cause some small movement of the aiming of the probe during the imaging procedure. This movement can cause the lesion to move into and out of the image plane during the procedure. As a result, the brightness of the lesion and its contrast agent in the image will vary with the lesion movement rather that solely due to contrast agent wash-in and wash-out. Consequently it is desirable to eliminate these unwanted motional effects when acquiring images used for perfusion assessment.

One technique for eliminating motional effects is described in U.S. Pat. 8,529,453 (Averkiou et al.) This technique involves acquiring images of the target anatomy, in this case the liver, which also show a portion of the diaphragm in the image. The size and position of the diaphragm in the images is used as a landmark. Images containing the diaphragm in the desired size and position are used for perfusion assessment, while images in which the diaphragm has changed its size and/or position or is absent entirely are deleted from subsequent processing. This in effect retains for processing only those images in which the lesion is shown in a consistent image plane. But recognition and deletion of images from the sequence is a manual process, requiring individual inspection and assessment of each image and its view of the diaphragm. Accordingly it is desirable to eliminate motional effects in an automated process which is both robust and requires less intensive user analysis of images.

In accordance with the principles of the present invention, methods are described for processing medical images so that movement due to a certain physiological function, such as the cyclic movement due to respiration or cardiac motion, can be identified and selectively removed from subsequently

processed images. This is preferably done by processing only those image frames which belong to the same range of phases of the motion cycle. By processing only those image frames acquired during the same phase range of the motion cycle, the image data is more uniformly affected by the motion and disparate motional effects are largely eliminated from the data, allowing for more precise quantitative assessment of anatomical performance such as perfusion. Clinical applications of the methods include liver, kidney, pancreas, breast, and prostate cancer assessment.

In one implementation, a sequence (loop) of images is acquired during one, and preferably more, cycles of the motion. The normal breathing rate of an adult at rest is 8-16 breaths per minutes, so the acquisition of a one-minute loop will acquire images over about 8-16 cycles of respiratory motion, for instance. The acquired images are tagged with their times of acquisition so that these times can be related to phases of the motion. Strong reflecting structures are identified in the images and their motion followed throughout the loop, which is identified by their cyclic variation in position and/or brightness throughout the loop. For instance, a reflector may start at one location in an image, move to another location over a first series of images, then back to its original location over a second series of images, the time to acquire the two series of images being the time of one cycle of motion. As a second example, a reflector may start with a given brightness in an image, increase in brightness during a first series of images, then decrease in brightness back to its original intensity during a second series of images. Again, the time required to acquire the two series of images is the time of a motion cycle. The identified time or times

of motion cycles may be compared with typical cycle times of the physiological function in question to see that they correlate. For example, if an identified motion cycle is outside an expected range of 5-20 breaths per minute, the cycle measurement would be discarded as a respiratory cycle and another cycle measurement made.

Once the motion cycles of the loop have been identified, those images which were acquired during desired phases of the motion cycle are accepted for further processing while the remainder are discarded. For example, it may be desired to accept for processing only those images which were acquired during a 25% range of phases of a respiratory cycle. Images acquired within this range of the respiratory phase of each cycle are then accepted for processing for quantified measurement, such as time-intensity curve and reperfusion measurement.

In the drawings:

FIGURE 1 illustrates in block diagram form an ultrasonic diagnostic imaging system constructed in accordance with the principles of the present invention.

FIGURES 2 and 3 illustrate details of the operation of the QLab processor of FIGURE 1 when calculating a time-intensity curve for perfusion assessment.

FIGURES 4a, 4b, and 4c illustrate the variation of the appearance of a tumor and blood vessels as the image plane moves due to respiratory motion.

FIGURE 5 illustrates in block diagram form a first method for removing respiratory motion effects from image characteristic quantification as performed by the ultrasound system of FIGURE 1 in accordance with the principles of the present invention.

FIGURE 6 illustrates in block diagram form a second method for removing respiratory motion effects

from image characteristic quantification as performed by the ultrasound system of FIGURE 1 in accordance with the principles of the present invention.

FIGURES 7a, 7b and 7c are ultrasound images illustrating the formation of a motion information matrix used to extract a respiratory curve in accordance with the present invention.

FIGURE 8 illustrates respiratory gating using a respiratory curve in accordance with the present invention.

FIGURE 9 illustrates time-intensity curves of a liver metastasis processed with and without respiratory gating in accordance with the present invention.

Referring first to FIGURE 1, an ultrasound system constructed in accordance with the principles of the present invention is shown in block diagram form. This system operates by scanning a two or three dimensional region of the body being imaged with ultrasonic transmit beams. As each beam is transmitted along its steered path through the body, the beam returns echo signals with linear and nonlinear (fundamental and harmonic frequency) components corresponding to the transmitted frequency components. The transmit signals are modulated by the nonlinear response of contrast agent microbubbles encountered by the beam, thereby generating echo signals with harmonic components.

The ultrasound system of FIGURE 1 utilizes a transmitter 16 which transmits waves or pulses of a selected modulation characteristic in a desired beam direction for the return of harmonic echo components from scatterers within the body. The transmitter is responsive to a number of control parameters which determine the characteristics of the transmit beams, including the frequency components of the transmit beam, their relative intensities or amplitudes, and

the phase or polarity of the transmit signals. The transmitter is coupled by a transmit/receive switch 14 to the elements of an array transducer 12 of an ultrasound probe 10. The array transducer can be a one dimensional array for planar (two dimensional) imaging or a two dimensional array for two dimensional or volumetric (three dimensional) imaging. A two dimensional matrix array can also be operated in an xMatrix mode in which a single plane (xPlane) which can be steered over a volumetric region is scanned by the matrix array probe.

The transducer array 12 receives echoes from the body containing fundamental (linear) and harmonic (nonlinear) frequency components which are within the transducer passband. These echo signals are coupled by the switch 14 to a beamformer 18 which appropriately delays echo signals from the different transducer elements then combines them to form a sequence of linear and harmonic signals from along the beam direction from shallow to deeper depths. Preferably the beamformer is a digital beamformer operating on digitized echo signals to produce a sequence of discrete coherent digital echo signals from a near field to a far field depth of the image. The beamformer may be a multiline beamformer which produces two or more sequences of echo signals along multiple spatially distinct receive scanlines in response to a single transmit beam, which is particularly useful for 3D imaging. The beamformed echo signals are coupled to an ensemble memory 22.

In the ultrasound system of FIGURE 1, multiple waves or pulses are transmitted in each beam direction using different modulation techniques, resulting in the reception of multiple echoes for each scanned point in the image field. The echoes corresponding to a common spatial location are referred to herein as an ensemble of echoes, and are

stored in the ensemble memory 22, from which they can be retrieved and processed together. The echoes of an ensemble are combined in various ways by the nonlinear signal separator 24 to produce the desired nonlinear or harmonic signals. For example, two pulses with different phase or polarity modulation can be transmitted to each point in the image field. When the echoes resulting from the two pulses are received by the ultrasound system and additively combined, the different modulation causes the fundamental frequency components of the echoes to cancel and the harmonic components to reinforce each other. This separates out the harmonic components of the echo signals. Alternatively, when the two echoes are subtracted from each other, the fundamental frequency components are reinforced and the harmonic components cancel. This separates out fundamental frequencies for construction of a standard B mode image. This modulation is referred to as "pulse inversion," and can be done by phase, polarity or amplitude modulation as described in US patents 5,706,819 (Hwang et al.), 5,951,478 (Hwang et al.), and 5,577,505 (Brock Fisher et al.)

The separated signals are filtered by a filter 30 to further remove unwanted frequency components, then subjected to B mode or Doppler detection by a detector 32. The detected signals are coupled to a nonlinear signal combiner 34 to reduce image speckle content. The signals are then processed for the formation of two dimensional, three dimensional, spectral, parametric, or other desired image in image processor 36, and the image is then displayed on a display 38. Detected fundamental (linear) signals which do not need speckle reduction processing are coupled directly to the image processor 36 for image formation and display.

In the system of FIGURE 1, the ultrasound image

data is also coupled to a QLab image processor 40 for the production of time-intensity curves and contrast agent wash-in and wash-out characteristics. The time-intensity curves and characteristics produced by the QLab processor are coupled back to the image processor where they may be displayed numerically or graphically on the display 38 along with the ultrasound images. A standard QLab processor which is suitable for the production of time-intensity curves is available from Philips Healthcare of Andover, Massachusetts.

A standard QLab processor produces the well-known time-intensity curves, also referred to as perfusion curves or reperfusion curves. See US patent 5,833,613 (Averkiou et al.), international patent publication WO 2005/099579 (Rafter), and international patent publication WO 2005/054898 (Garg et al.) As these publications illustrate, the build-up of contrast agent at points in the tissue (points in the image) is monitored during the arrival of the contrast agent at locations in the body. The amount of contrast agent at a point is indicated by the intensity of echoes returned from contrast agent microbubbles at each point, and is present in a sequence of images acquired by low power (low MI) transmission as the contrast agent washes into the tissue. A time-intensity curve can be formed of this build-up of contrast intensity and its subsequent decline during wash-out of the contrast agent for each point in the tissue which returns the time sequence of echoes frame-by-frame. A qualitative presentation of the time-intensity curves for the entire tissue being viewed can be formed by coloring each pixel in an anatomical image with a color that represents a parameter of the time-intensity curves at each point in the image. The Garg et al. application illustrates the formation of a parametric

image of the myocardium where the color of each pixel in the image represents the peak level attained by the time-intensity curve at each point in the myocardium, for example. Alternatively, the slope of the time-intensity curve can be used to indicate the rate of reperfusion instead of the peak. See also US patent 6,692,438 (Skyba et al.)

In an implementation of the present invention, contrast agent perfusion echo data is acquired over a sequence (loop) of images as the contrast agent arrives at the location of a metastasis in the body, builds up, and then washes out. The intensity values of the echoes will thus start from a baseline level of no contrast agent present, then rise, plateau, and decline as the contrast agent washes out. A curve-fitting algorithm then fits this data variation to an error function defined as

$$I(t) = A[erf\{(t-t_0)/T\} + I_0]$$

where I(t) is the linear intensity at time t, A is the maximum intensity over the baseline offset, T is wash-in time parameter which is linearly proportional to wash-in time (*e.g.*, from 5%-95%), I_0 is baseline offset, and t_0 is a time offset. The wash-in time is preferably extracted from the fitted curve rather than the noisy image data. Preferably the contrast agent echo data does not undergo data compression prior to this processing so that the data remains in its acquired linear relationship. Another approach is to fit the whole time-intensity curve (instead of just the wash-in part) to appropriate mathematical models as the lognormal distribution for example defined as

$$I(t) = \frac{A}{\sqrt{2\pi}\sigma(t-t_0)} e^{\frac{[\ln(t-t_0)-\mu]^2}{2\sigma^2}} + C$$

where μ and σ are the mean and standard deviation of the normal distribution from which the logarithmic transformation was obtained. The curve

can be scaled horizontally by varying μ and changed in terms of skewness by varying σ. The area under the curve is A, t_0 is the time offset, and C is the baseline intensity offset. The lognormal fitted curve is used to extract the wash-in time.

The ultrasound system of FIGURE 1 can compute a quantitative measure of the perfusion of a metastasis, a parameter referred to as the wash-in time ratio (WITR). The WITR is computed as shown by the block diagram of FIGURE 2. From a temporal sequence of images of a metastasis or lesion during contrast agent wash-in and wash-out, contrast agent intensity values are computed for the ROI_{Met} of the metastasis 50, a region of interest in the metastasis, as indicated by box 72. As explained above, these values can be computed by combining the pixel values of the metastasis ROI for each image of the sequence acquired during wash-in. In box 74 intensity values are computed for an ROI_{Par} of normal parenchyma of the tissue. This may be done by tracing a region of normal tissue in an image of the liver metastasis and using the normal tissue perfusion pixel values within this second tracing. These values are therefore perfusion values of normal tissue. In box 76 a time-intensity curve is fitted to the perfusion values of ROI_{MET}, and in box 78 a time-intensity curve is fitted to the perfusion values of ROI_{PAR}. The fit is not always necessary but it gives a better estimation of WITR. While WITR can be measured directly from the data, noise in the data can interfere with the accuracy of the measurement, hence the preference for curve-fitting. A wash-in time parameter WIT is found for each curve, for example by use of the error function or lognormal distribution described above. This determines a wash-in time parameter for both the metastasis and normal parenchyma, WIT_{MET} and WIT_{PAR}, respectively. A

wash-in time ratio WITR is then computed from the two wash-in parameters by dividing WIT_{Met} by WIT_{Par} as shown by box 70. The effect of normalizing WIT_{Met} by the wash-in time parameter of normal tissue is to reduce or eliminate the effects of variables in the procedure such as bolus size, cardiac output, and ultrasound system settings, which may differ from one therapy session to another. Thus, comparable quantitative measures of the growth or shrinkage of the metastasis as indicated by its angiogenesis can be produced for each therapy session over the period of weeks or months that the patient is being treated.

Another quantified measure of metastasis angiogenesis which reduces or removes the effects of bolus injection rate, cardiac output of the patient, or variation in machine settings is illustrated in FIGURE 3. A time-intensity curve is fitted for each of the ROIs of the metastasis and the parenchyma as shown in boxes 76 and 78. In boxes 82 and 84, the range of each time-intensity curve is normalized. A convenient normalization scale is zero to one. In box 80 a difference curve ΔT-I Curve is computed as the difference between the two normalized curves T-I $Curve_{MET}$ and T-I $Curve_{PAR}$. Further details of this production of a time-intensity curve may be found in U.S. Pat. 8,529,453 (Averkiou et al.) which is incorporated herein by reference.

As mentioned above, a typical period of contrast agent wash-in and wash-out can last for as long as 100 seconds or more. This means that a clinician acquiring the image data must maintain the same image of the lesion steadily for 100 seconds so that each intensity value is of the same region of the lesion. If the probe moves during the acquisition, for instance, the lesion can move out of the image plane and the data acquired cannot be used. Even if the probe is held steady against the body of the patient,

the lesion can still move relative to the probe field of view due to the respiratory motion of the patient. This is illustrated by the ultrasound images of FIGURES 4a, 4b, and 4c. These are images of a liver lesion indicated by the white pointer over the images with the hepatic artery visible in the images beneath the lesion and above the circle 2. These images were acquired while the sonographer was trying to hold the probe steady against the abdomen of the patient so that the same anatomy was continuously shown in the images from one image to the next. But the images are affected by the breathing of the patient and the respiratory motion causes the lesion and the desired image to move in and out of the image plane of the probe. This is best illustrated in these images by the variation seen of the hepatic artery. In FIGURE 4a it is seen that the image cut plane through the hepatic artery is through the central region of the artery and the artery appears large in the image. But that central portion of the artery has moved out of the image plane in FIGURE 4b and the artery appears much thinner as a different cut plane through the artery has moved into the image plane. In FIGURE 4c the artery is barely visible as it has move almost completely out of the probe's image plane. Corresponding, the size and position of the lesion indicated by the white pointer also changes from one image to another. One way to overcome the deleterious effect of respiratory motion is to gate the image acquisition to the respiratory cycle. A respiratory signal can be acquired by known means such as an elastic band with strain or pressure sensors around the chest of the patient. Another technique is to transmit small signals between sensors across the chest of the patient and measure the patient's chest impedance variations. These and other techniques can produce cyclical signals of the

respiratory cycle and can be used to gate the acquisition of images to the same phase of the respiratory cycle.

In accordance with the principles of the present invention, respiratory gating is performed by image processing as shown by the block diagram of FIGURE 5, which illustrates one implementation of the present invention. In step 50 a sequence of successive images is acquired during one or more motion cycles. This image loop could be a sequence of images acquired during the 100+ seconds of contrast agent wash-in and wash-out mentioned above, and could comprise hundreds or even thousands of images. Obviously, manually processing this many images would be a painstaking task. An image loop this long would cover over 20 respiratory cycles at a nominal breathing rate of thirteen breaths per minute. A loop this long would cover about 100 heartbeat cycles at a nominal heart rate of one beat per second. This loop would therefore be contaminated by many cycles of motion of either physiological phenomenon.

In step 52 the cyclical motion is identified. One way to do this may be understood with reference to the images of FIGURE 4. It is seen in these images that the hepatic artery above the circle 2, filled as it is with contrast agent, is a very bright reflector in the images, indeed it is the largest bright structure in the images. The artery is seen to be at its largest and brightest when the cut plane of the image passes through the center of the artery as it is in FIGURE 4a, and less so in the other images. Thresholding or decimation of the pixel values of these images below the hepatic artery brightness will extract the pixels of the hepatic artery from the center of the images and the pixel values summed or integrated to indicate the brightness of this structure in each image. The

recurrence of the peak brightness of the hepatic artery each time it moves fully into the cut plane of the probe image plane indicates the periodicity of the respiratory motion moving the image plane, and the duration of the motional cycle is the time between the acquisition of two such images as shown by their time-tagging. With the motion cycle thus identified, the images acquired during a desired phase or phase range of the motion are identified in step 54. For instance, it may be decided to use each image of peak brightness (FIGURE 4a) and the five images preceding and succeeding the peak brightness image in every respiratory cycle. These eleven images of each respiratory cycle are then selected for perfusion assessment processing as shown in step 56. The images which were acquired during less desirable phases of the respiratory cycle are omitted from processing. As a result the perfusion measurement should be relatively unaffected by the effects of respiratory motion.

FIGURE 6 illustrates a preferred implementation of the present invention in block diagram form. Using the acquired image sequence from step 50 in this drawing, the motion information contained in the image sequence is extracted in what is referred to herein as a "motion information matrix." FIGURES 7a-7d illustrate one way to form a motion information matrix (MIM). FIGURE 7a illustrates an ultrasound image of the liver and FIGURE 7b illustrates an image which is an average of all of the image frames in the loop containing the image of FIGURE 7a. Each frame of the loop such as that of FIGURE 7a is subtracted from the average of the frames (FIGURE 7b) and pixel intensities above a certain threshold are assigned a value of 1 with all others assigned a value of zero. This produces a binary image of bright structures in each image such as the one shown in FIGURE 7c. The

resulting binary images are added together to form an MIM as shown in FIGURE 7d, an image of structures which can be readily identified in the image loop and which are potentially affected by motion.

The next step 62 is the selection of a trigger frame from the loop. A trigger frame is one which will be included among the finally processed images. It may be one, for instance, in which the lesion is clearly defined as by a high intensity or large size in the image. Or it may be an image which appears virtually identical to previously and/or successively acquired images in the loop and thus exhibits little or no motion contamination. The trigger frame may be designated by the user by inspection, or may be selected by an automated method such as by subtracting each pair of successive frames and using using one of the frames which produced the most minimal difference image. Candidate structure for motion identification are then extracted from the trigger frame for motion curve formation as shown by step 64. This extraction may comprise a binary image produced from the trigger frame as discussed above. The structures extracted from the trigger image are compared with the structures of the MIM to choose one which is significantly affected by motion. A structure of the MIM which varies over a wide intensity range or positional range could be selected, for instance. The frequency of the variation can be compared with the frequency of the physiological phenomenon to ascertain that its variation corresponds to that of the physiological function. If it does not, the structure is disregarded and another structure of the MIM selected for motion identification. To aid in the selection, the structures of the MIM can be ranked in accordance with their likelihood of exhibiting effects of motion. The structure which is found to be the

region of greatest interest for motion extraction is then used as a binary mask that is used to extract a curve of the respiratory or other bodily motion. The mask of the structure is applied to the corresponding location in each image in the loop and a series of intensity values extracted from the image frames which exhibit intensity variation during the loop that is representative of the cyclical motion. These intensity values are plotted as a function of time (or, equivalently, frame number in the sequence) to yield an approximate respiratory curve. The initial plot may be fitted to an average curve to produce a smoothly varying respiratory curve as shown by respiratory curve 100 in FIGURE 8. Known curve fitting techniques may be used to produce a smoothly varying curve, such as a piecewise cubic Hermite interpolating polynomial fitted to the peaks and troughs of the approximate curve, for instance.

FIGURE 8 illustrates a respiratory curve 100 formed from respiratory motion intensity variation of a structure over a loop of 600 image frames. It is seen that the curve 100 indicates 21 respiratory cycles occurring during acquisition of the 600 image frames. The small circles 110 at the top of the plot indicate some of the discrete frames of the loop. The circles are shown on the respiratory curve in correspondence to the points in the respiratory cycles. A threshold 102 is applied to the curve 100 to delineate the phase range of each respiratory cycle during which image frames will be accepted for perfusion processing. For instance, suppose that the lower peaks of the respiratory curve are points where the patient has fully inhaled, and the upper peaks of the curve are points where the patient has fully exhaled. The clinician may decide to use image frames that all were acquired around the time of full exhalation, for example, just before and just after

the patient has fully exhaled. The system then applies a threshold 102 as shown in the drawing which delineates, in this example, this phase range of each respiratory cycle, which is seen in this example to comprise about 30% of each cycle. The image frames acquired during this respiratory phase range, the frames represented by the circles 110, are then selected for processing as shown in step 66 of FIGURE 6. The processed image frames of step 68 are thus a set of frames which all were acquired during the same phase range of respiratory motion and should thus generally correspond spatially to each other, with the structures and lesions of the images appearing generally the same in size and position in each of the processed images. This will yield accurate quantification of physiological measures and functions such as time-intensity curve production and perfusion assessment. The data for such quantification may be selected from the accepted images using the trigger frame. The lesion is identified in the trigger frame as a region of interest (ROI), and data extracted from the location of the ROI in each of the accepted image frames. This data is then processed to produce time-intensity curves as described above and in European patent EP 2 234 544 B1, the contents of which are incorporated herein.

The foregoing technique was applied to clinically acquired image loops from a number of liver cancer patients. FIGURE 9 illustrates time-intensity curves produced in one of these cases, both with and without respiratory phase gating. The intensity data of a region of interest in the images was fitted to a lognormal function to produce time-intensity curves of reperfusion. The goodness of fit was quantified using the R-squared value and the root mean squared error technique. The time-intensity

curve 120 was produced from data of all of the image frames without gating, and is seen to be affected by the highly oscillatory characteristic of the intensity values 140 sampled at the ROI of the images, which contains large spikes due to sampling of images outside the lesion caused by respiratory motion of the anatomy. When gating is applied in accordance with the present invention and only the image frames 110 acquired around the lower phase range of motion are used, the oscillatory effects of the intensity data are greatly diminished because sampling more uniformly occurs within the lesion since the size and position of the lesion ROI are more uniform over the image frames 110 accepted for processing.

The mathematical formulae used in an implementation of the present invention is detailed in Appendix A, and their use in a method of the present invention explained.

Appendix A

Step Index	Description	Mathematical Formulae and Description
1	Import the video	I_{ori}=I(x, y, z) x is the frame's rows y is the frame's columns z is the number of frames
2	Decimate the video's frames by 2 for faster processing	I_{ori}=I$(x, y, \hat{z})$ $\hat{z} = \{2n + 1 : n \; is \; an \; integer; and 0 \leq n \leq \lfloor \frac{(z-1)}{2} \rfloor \}$
3	Compress the video frames for faster processing	I_{comp}=I$(\hat{x}, \hat{y}, \hat{z})$ Pixel intensity values corresponding to $\hat{x}, \hat{y}$ pixel coordinates calculated via piecewise constant interpolation (nearest-neighbour interpolation)
4	Calculated average frame from the compressed video I_{comp}	$I_{ave} = \frac{\sum_{i=1}^{\max(\hat{z})} I_{comp}(\hat{x}, \hat{y}, i)}{\max(\hat{z})}$
5	Subtract each frame for the average	$I_{mov} = I_{comp}(\hat{x}, \hat{y}, \hat{z}) - I_{ave}(\hat{x}, \hat{y}) \quad \forall \; \hat{z}$
6	Set pixel intensities below a certain threshold to zero in I_{mov} and pixels	$I_{zero}(I_{mov} \leq threshold) = 0$

	above that threshold to 1	$I_{thre}(I_{zero} \neq 0) = 1$
7	Remove pixels from frames that are surrounded by zeros	I_{clean}=($I_{thre} \not\supseteq$ non zero intensity pixels surrounded by zero values)
8	Extract n^{th} largest group of connected pixels from each frame	I_{larg}=($I_{clean} \supset n^{th}$ largest group of connected pixels)
9	Perform the morphological operation of close on each frame of I_{larg} with a 4-pixel wide square structuring element	I_{close}=$(I_{larg} \otimes S) \ominus S$ $S = \begin{matrix} 1 & 1 & 1 & 1 \\ 1 & 1 & 1 & 1 \\ 1 & 1 & 1 & 1 \\ 1 & 1 & 1 & 1 \end{matrix}$
10	Add all frames of I_{close} together	I_{sum}=$\sum_{i=1}^{\max(\hat{z})} I_{close}(\hat{x}, \hat{y}, i)$
11	Resize the I_{sum} frames to the original resolution of I_{ori} using bicubic interpolation to acquire the MIM	$MIM = resize(I_{sum})$
12	Produce average frame of the original video	I_{ave_ori}=$\frac{\sum_{i=1}^{\max(z)} I_{ori}(x,y,i)}{\max(z)}$
13	Subtract the T-frame chosen by the user from the I_{ave_ori}	I_{mov_ori}=$I_{ori}(x, y, z_{trigger}) - I_{ave\_ori}$
14	Repeat steps 6-7 on I_{mov_ori}	$I_{mov\_ori} \rightarrow I_{clean\_ori}$
15	Extract the k^{th} largest groups of connected pixels from I_{clean_ori}	$I_{larg_{ori}}$=($I_{clean_{ori}} \supset k^{th}$ largest groups of connected pixels)

16	Perform the morphological operation of close on each frame of I_{larg_ori} with a 4-pixel wide square structuring element	$I_{close\_ori}=(I_{larg\_ori} \otimes S) \ominus S$ $S=\begin{matrix}1&1&1&1\\1&1&1&1\\1&1&1&1\\1&1&1&1\end{matrix}$
17	Extract the x,y coordinates of the contour of each structure in I_{close_ori} and pass them through a median filter	$x_{filt}[i]=\text{median}(x[i],(i) \in w)$ $y_{filt}[j]=\text{median}(y[j],(j) \in w)$ w is the median filter window size
18	Reconstruct the C-ROIs from the x_{filt} and y_{filt} vectors and store them in I_{C-ROI}	$x_{filt}, y_{filt} \rightarrow I_{C-ROI}$
19	Acquire the total pixel intensity contained in a M x M pixel square with its centre around the centre of gravity of each C-ROI in I_{C-ROI}, across the z-dimension (i.e. across the frames) of $I_{ori}(x,y,z)$.	$V^q(i) = \sum I_{ori}(x_{square}, y_{square}, i)$ x_{square}, y_{square} *are the coordinates assigned to the* $M \times M$ *square around the centre of gravity of each* $C-ROI$ i: *frame index* q: $C-ROI$ *index*
20	Smooth the data contained in $V(i)$ using robust locally weighted scatterplot smoothing (RLOESS) and a 2nd degree polynomial model	$V^q(i) \rightarrow V^q(i)_{smooth}$
21	Perform a Fast Fourier Transform (FFT) on each $V(i)$ and retrieve the maximum frequency (F_{major}) contained in each $V(i)$	$F^q(k) = \sum_{i=1}^{N} V^q(i)_{smooth}\, \omega_N^{(j-1)(k-1)}$ $F^q{}_{major} = \max(\lvert F^q(k) \rvert)$
22	Compare the F_{major} of each structure and check if it lies within the range of the motion the user desires to remove. Remove structures from I_{C-ROI} that do not fulfil criterion.	$I_{C-ROI} \rightarrow I_{freq\_filt}$

23	Element-by-element multiplication of the MIM matrix with I_{freq_filt}	$I_{intersect} = MIM \odot I_{freq\_filt}$
24	Calculate mean value of the matrix elements contained within each ROI in $I_{intersect}$	$M(i) = \frac{\sum I_{intersect}(i)}{N(i)}$ i: identifies each ROI $N(i)$: number of pixels within each ROI $\sum I_{intersect}(i)$: sum of the matrix elements contained in each ROI (i) of $I_{intersect}$
25	Choose the ROI with the highest $M(i)$ and store the resulting ROI as a binary image in I_{E-ROI}	I_{E-ROI}
26	Extract the mean intensity contained in I_{E-ROI}, across the frames of the original video. The resulting vector is stored as an IC.	$I_{ROI-intersect}=I_{ori}(x,y,z) \odot I_{E-ROI}(x,y) \quad \forall z$ $IC(z) = \frac{\sum I_{ROI-intersect}(\acute{x},\acute{y},z)}{N} \forall z$ $\acute{x},\acute{y}$: row and column coordinates of the intersection between I_{ori} and I_{E-ROI} N: number of pixels of the $E-ROI$
27	Gate the IC by finding the peaks and troughs of the IC and keep the frames that are within a user-defined percentage of the peaks, troughs or any other portion of the IC in-between	$I_{ori}(x,y,z) \rightarrow I^{l}{}_{gated}(x,y,\tilde{z})$ $\tilde{z}$: Index of frames kept after gating l: Index of cyclic motion phase

WHAT IS CLAIMED IS:

1. A method for reducing the effect of physiological motion in image data acquired from a sequence of medical images of a subject comprising:

acquiring a sequence of medical images containing image data of a target region of a subject during the occurrence of cyclical physiological motion affecting the target region;

using image data of the images to identify cycles of the physiological motion;

identifying images acquired during a certain range of phases of the identified motion cycles; and

processing image data of the identified images to assess a property of the target region.

2. The method of Claim 1, wherein the acquiring step further comprises acquiring a loop of medical images which are affected by respiratory motion or cardiac motion.

3. The method of Claim 1, wherein using image data further comprises using image data of the same corresponding location in each of the images to identify cycles of the physiological motion.

4. The method of Claim 3, wherein using image data further comprises using intensity image data.

5. The method of Claim 1, wherein processing further comprises processing image data of the target region from each of the identified images.

6. The method of Claim 1, wherein acquiring further comprises acquiring a sequence of two dimensional medical images of an image plane during the occurrence of physiological motion affecting the

target region by moving the target region in and out of the image plane.

7. The method of Claim 1, wherein acquiring further comprises acquiring a sequence of two dimensional medical images of an image plane during the occurrence of physiological motion affecting the target region by varying its intensity or location in an image during the acquisition.

8. The method of Claim 1, wherein using image data further comprises extracting a motion information matrix from the image data.

9. The method of Claim 8, wherein using image data further comprises selecting a trigger frame acquired during the range of phases of one of the cycles.

10. The method of Claim 9, wherein using image data further comprises using image data of the trigger frame and data of the motion information matrix to select a structure in the images whose image data is to be used for motion curve identification.

11. The method of Claim 10, wherein using image data further comprises identifying a motion curve using the variation in brightness or position of the selected structure over the sequence of images.

12. The method of Claim 1, wherein using image data of the images to identify cycles of motion further comprises comparing the frequency of cycles of motion to an expected frequency of a cyclical physiological phenomenon.

13. The method of Claim 1, wherein processing image data further comprises processing image data from the target region in identified images to produce a time-intensity curve of perfusion.

14. The method of Claim 13, wherein processing image data further comprises processing contrast agent image data from an image region containing a tumor or lesion in identified images to produce a time-intensity curve of contrast reperfusion.

15. A method for reducing the effect of respiratory motion in image data of a time sequence of ultrasound images which is to be used to produce a time-intensity curve comprising:

acquiring a sequence of ultrasound images containing image data of a target region for which a time-intensity curve is to be produced, the sequence being acquired during the occurrence of respiratory motion affecting the target region;

using image data of the images to identify cycles of the respiratory motion;

selecting a range of phases of the identified respiratory motion cycles; and

processing image data of images of the sequence which were acquired at one of the phases of the selected range of phases of the respiratory motion cycles.

ELIMINATING MOTION EFFECTS IN MEDICAL IMAGES CAUSED BY PHYSIOLOGICAL FUNCTION

Abstract of the disclosure:

Ultrasonic imaging methods are described for eliminating the effects of physiological motion such as respiratory motion from image data of a sequence of images which is to be used for quantified analysis such as time-intensity curve computation. A bright reflector in the images of the loop which exhibits motional effects such as cyclical variation in brightness or position from image to image is identified and its variation used to identify cycles of motion. A phase or range of phases of the cycles is identified. Images acquired during the identified phase or phase range of the motion cycles during the loop are then used for quantified processing.

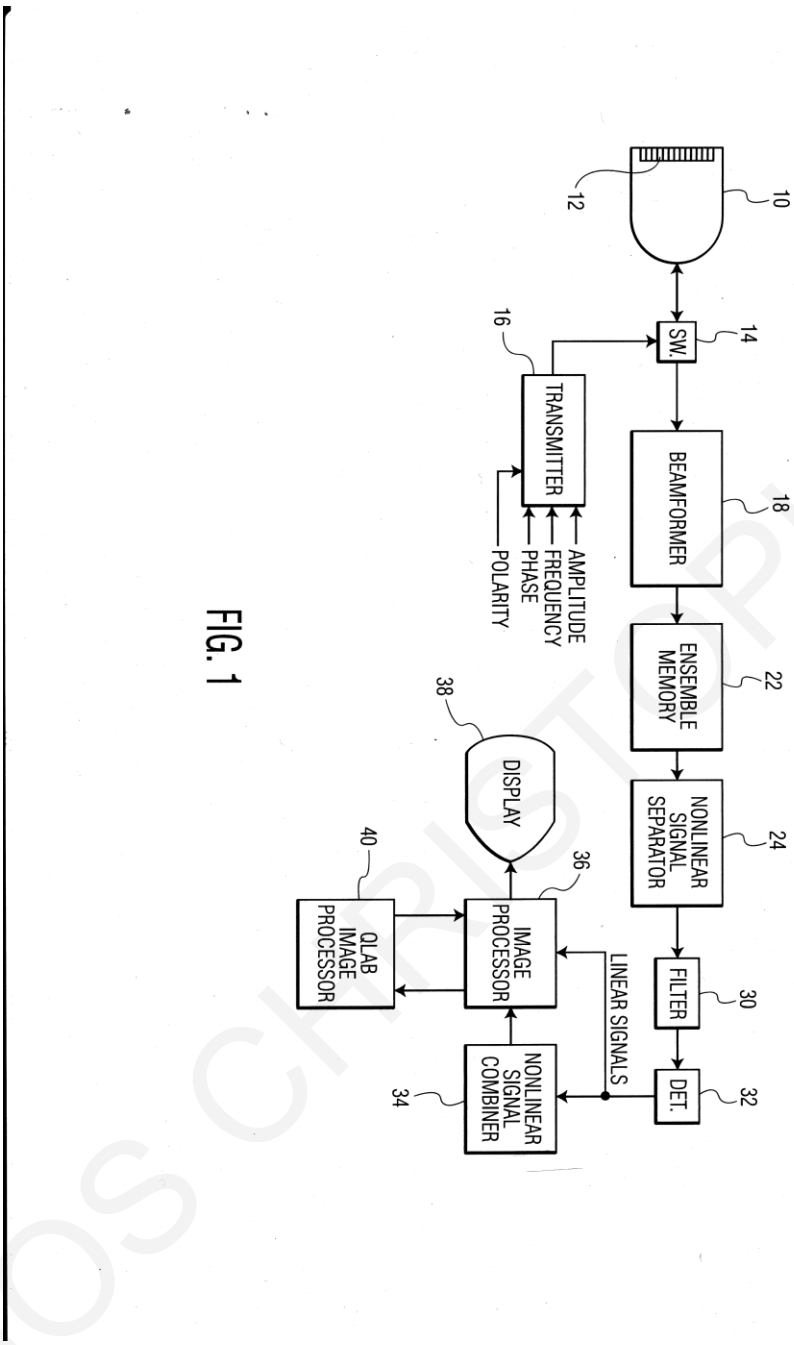

FIG. 1

ATL-550

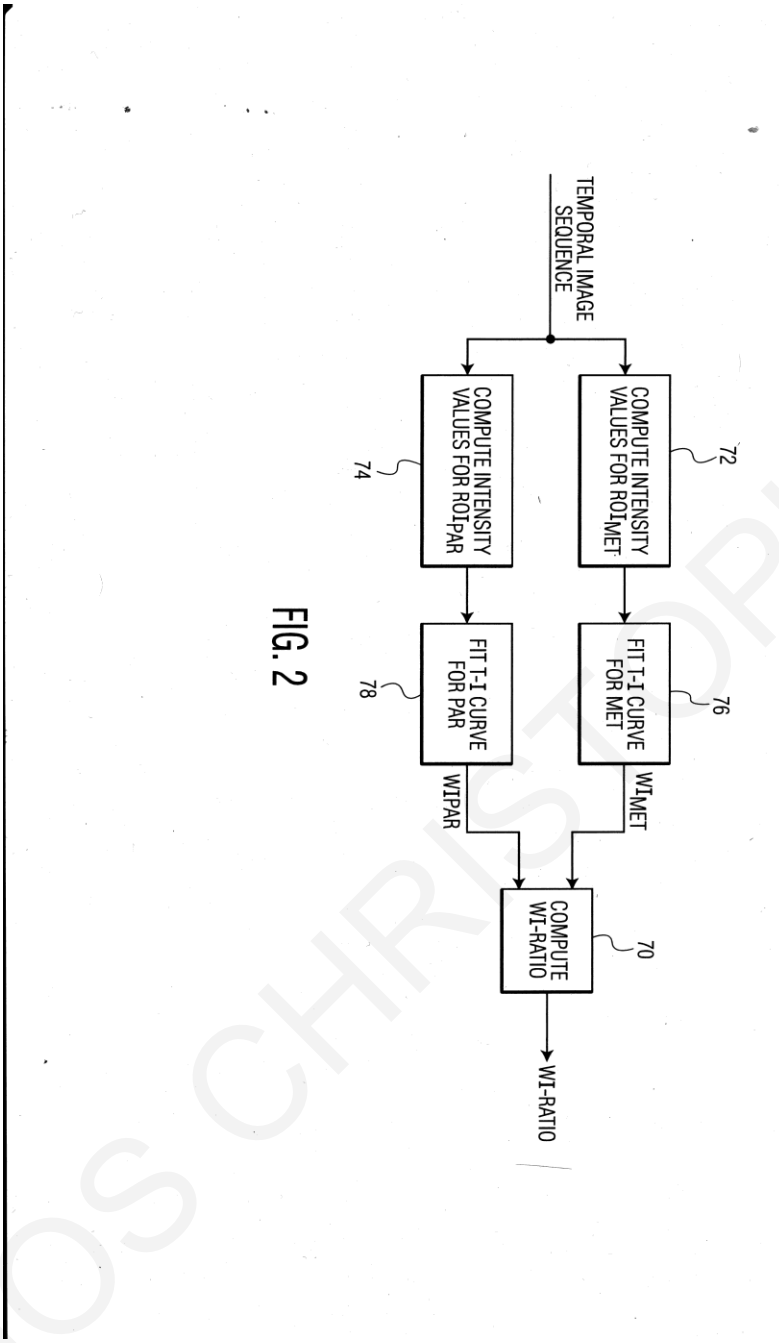

FIG. 2

ATL-550

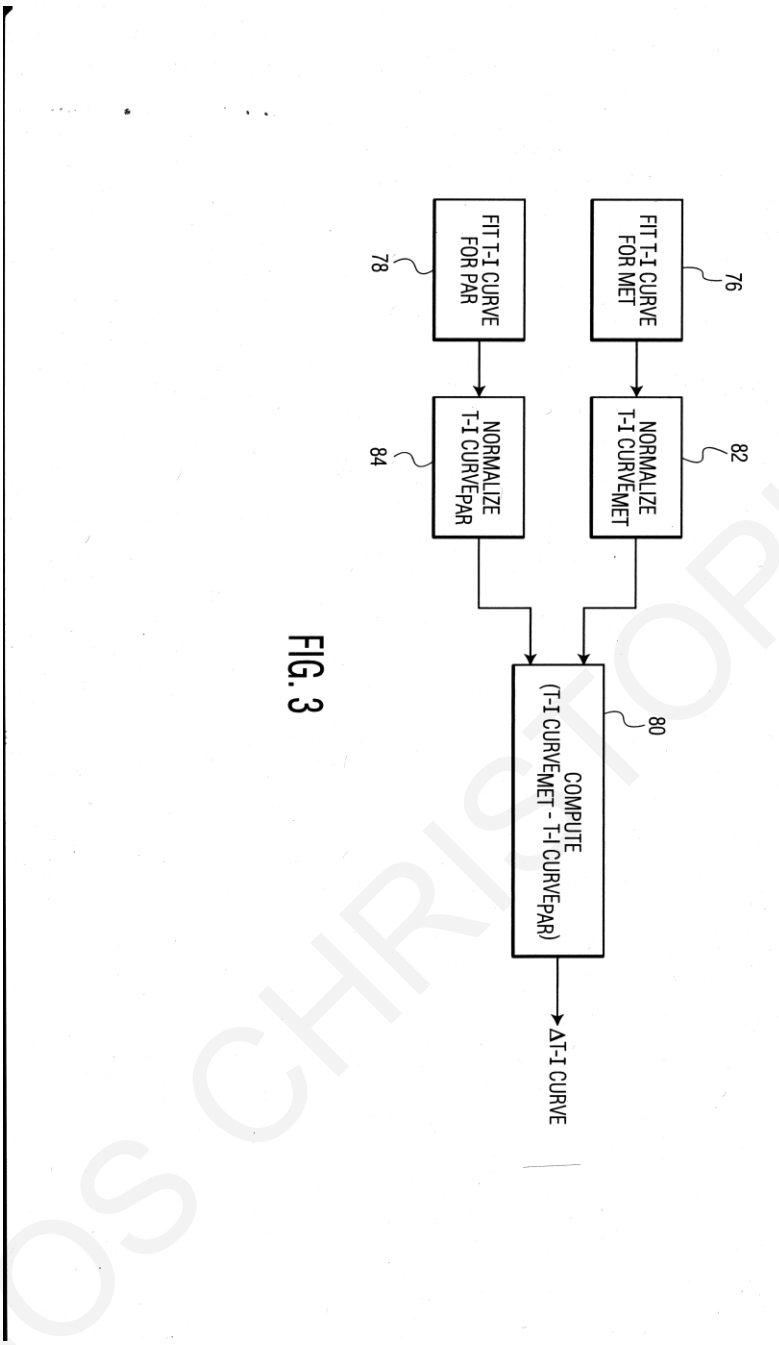

FIG. 3

ATL-550

ATL-550

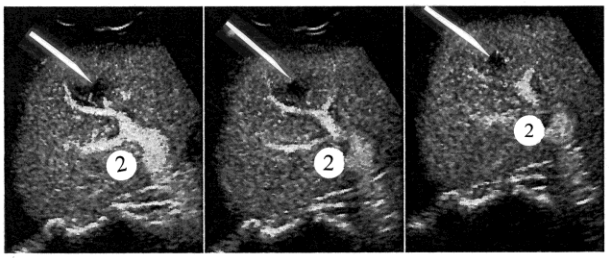

FIG. 4 a) b) c)

FIG. 7

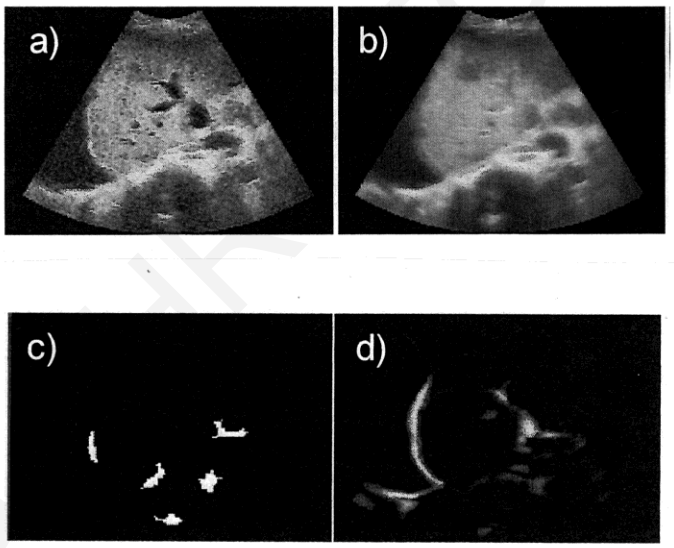

ATL-550

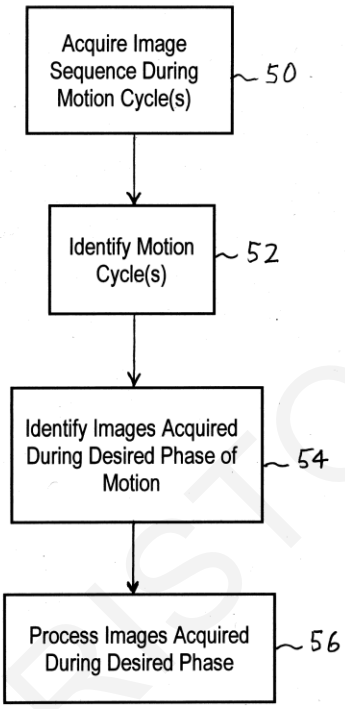

FIG. 5

ATL-550

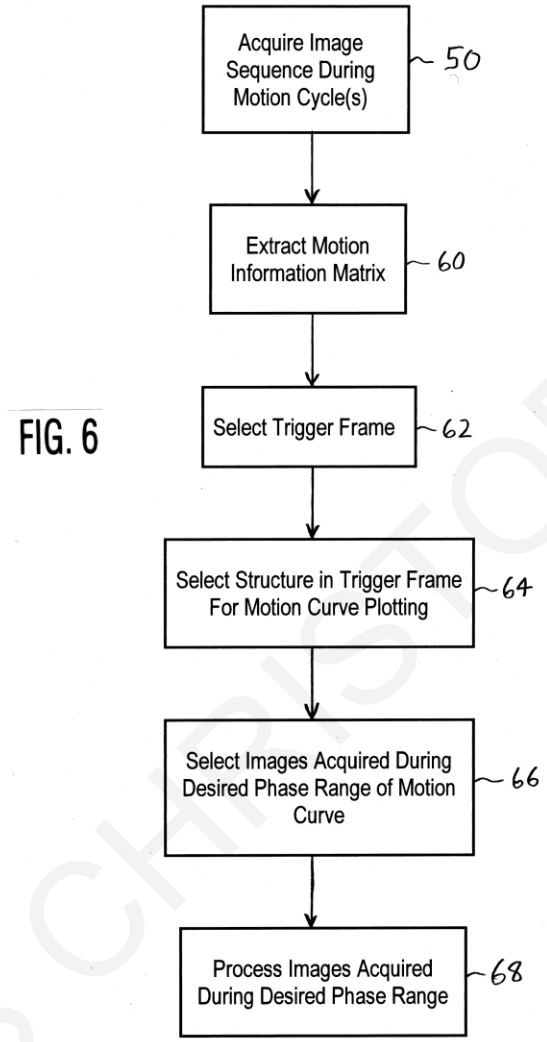

FIG. 6

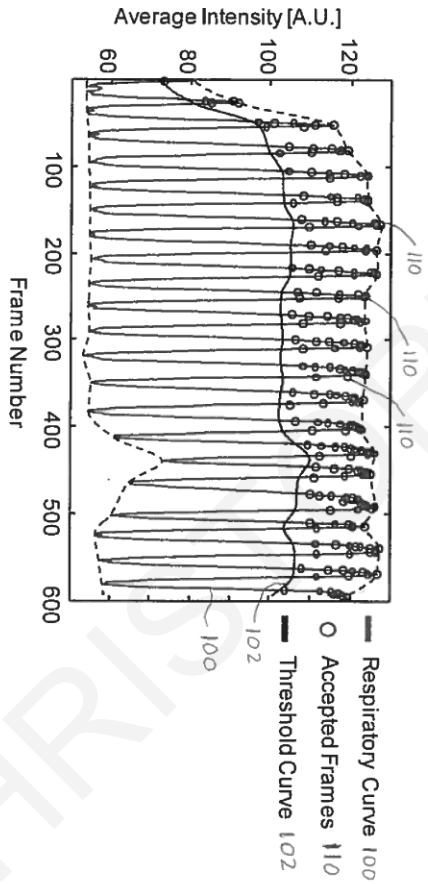

FIG. 8

ATL-55D

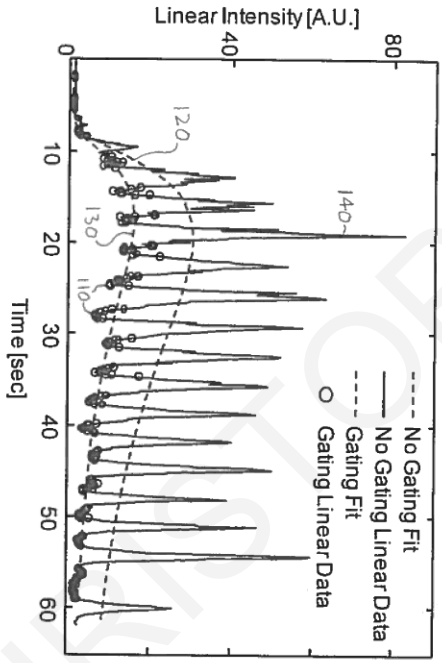

FIG. 9

AT1-550

Appendix 2

Evaluation of carotid plaque using contrast enhanced ultrasonic imaging

This invention relates to ultrasonic diagnostic imaging systems and, in particular, to the use of contrast enhanced ultrasonic imaging to evaluate the risk of stroke.

The development of plaque in the vascular system, particularly atherosclerosis in the carotid artery, is a common occurrence in many patients. Plaque can build up to a degree where partial and even total occlusion of blood vessels can occur. FIGURE 1 illustrates a blood vessel 110 with the vessel wall 18 partially cut away to show the lumen 16 inside, where a plaque build-up 24 is seen. Since the plaque 24 has filled most of the lumen at its thickest point it has partially occluded the flow of blood through the vessel. Not only does the plaque restrict the delivery of fresh blood to tissue and organs downstream of the occlusion, but it can also trap blood clots in the narrowed lumen, blocking all blood flow. An additional, equally serious occurrence can arise from carotid plaque. Since the carotid arteries provide the supply of blood to the brain, particulate matter in the carotid blood flow can pose a risk of cranial vessel occlusion and potentially stroke. Bits of plaque can break loose from the endothelial lining of the carotid arteries and flow to the brain, where they can occlude cranial blood vessels of different dimensions and functionality, depending on the size of the plaque particulates and their path of flow. It would be desirable to be able to identify plaques with this potential so that intervention can be taken to minimize or prevent the potential for stroke.

In accordance with the principles of the present invention, an ultrasonic diagnostic imaging system and method are described which enable the assessment of the risk of stroke from plaque build-up in the carotid artery. Carotid atherosclerotic plaques have

areas of plaque neovascularization and perfusion. A study using images from twenty-four patients was conducted to differentiate between symptomatic and asymptomatic patients based on plaque perfusion patterns. In this study the perfusion of carotid plaques was evaluated both qualitatively and quantitatively in order to investigate differences in the perfusion between symptomatic and asymptomatic patients. The patients were injected with 2ml of Sonovue (Bracco s.p.a., Milan, Italy), an ultrasonic microbubble contrast agent, and one minute ultrasound loops were acquired and saved as the contrast agent flowed through the carotid artery and perfused the plaque microvasculature with microbubbles. The ultrasound images can be acquired by B mode imaging which shows the increasing signal intensity from microbubbles which perfuse the plaque. Preferably, the images are acquired by colorflow imaging so that motion of the microbubbles can simultaneously be detected along with signal intensity. Signals exhibiting a high intensity harmonic return together with Doppler-detected motion at the same location are indicative of moving microbubbles at that location. This correlation can be used to distinguish over and reject signal returns from static bright reflectors which are often artifacts. The result is the detection of dynamic contrast agent microflow in the plaque vasculature.

Since the ultrasound image sequence is to be used to calculate contrast time-intensity curves (T-I curves) at each point in the plaque, it is important to hold the imaging probe as stationary as possible during image acquisition so that the plaque in the images will spatially correlate over the image sequence. The spatial correlation can be improved by the use of image stabilization, for instance, and/or by detecting and compensating for global motion in

the images as might occur due to probe motion or anatomical motion from pulsatility or patient movement.

For the assessment of contrast perfusion of the plaque a region-of-interest (ROI) is drawn around the plaque in the images. This delineates the plaque without including any portion of the lumen signal so that the potentially large amplitude signals returning from contrast agent flowing in the carotid lumen is excluded from the analysis. The mean intensity contrast agent signal from within the ROI containing the plaque is sampled across time from image to image to generate time intensity curves of the carotid plaque. The mean intensity signal from individual points in the plaque (pixels) can be used, or groups of pixels can be aggregated and the mean intensity of signals from the aggregated groups of pixels used. The signal intensity data is assessed by comparing the signal levels against a threshold noise level and by assessing the distribution of values of intensity before and after contrast arrival. If there is a significant difference and distribution of values characteristic of contrast build-up, the pixel is identified as indicating perfusion. The mean T-I curve signal amplitude after the arrival of the microbubbles into the plaque ROI is calculated for each pixel. A qualitative image of the mean intensity signal amplitudes of the pixels can be displayed as colors or intensities of a range of values to indicate qualitatively the vascularization of the plaque.

In accordance with a further aspect of the present invention, quantitative perfusion assessment is performed on the pixel data. The overall number of pixels that have perfusion are divided by the total number of pixels in the delineated image of the plaque. A binary grading system is then applied to

this result. Zero represents less than 50% of carotid plaque area contained moving microbubbles and 1 represents more than 50% of the carotid plaque area contained moving microbubbles. It was found that for the patients of the study the mean contrast agent intensity signal from the plaques was significantly higher for asymptomatic patients (patients with no history of plaque particulate breakup) than symptomatic patients (patients with a history of plaque particulates in the blood flow). The qualitative analysis results of the study showed that only 25% (3/12) of asymptomatic patients had a score of 0 in comparison to 67% (8/12) of symptomatic patients.

In the drawings:

FIGURE 1 is an illustration of a blood vessel containing plaque.

FIGURE 2 illustrates in block diagram form an ultrasound system constructed in accordance with the principles of the present invention.

FIGURE 3 illustrates a contrast time-intensity curve.

FIGURES 4a and 5a are ultrasound images in which plaques in carotid arteries have been outlined.

FIGURES 4b and 5b illustrate the change in signal intensity in the plaque areas of FIGURES 4a and 5a with the arrival of contrast agent flows in the plaques.

FIGURE 6 is a flowchart illustrating the steps of a method of the present invention.

FIGURE 7 illustrates four qualitative images of atherosclerotic plaque areas with different percentages of perfusion.

Referring now to FIGURE 2, an ultrasound system constructed in accordance with the principles of the present invention is shown in block diagram form. An ultrasonic probe 12 includes an array 14 of

ultrasonic transducer elements that transmits and receives ultrasonic signals. The array 14 may be a one dimensional linear or curved array for two dimensional imaging, or may be a two dimensional (2D) matrix of transducer elements for electronic beam steering in three dimensions. The array 14 may also be a one dimensional array that is mechanically swept back and forth by the ultrasonic probe 12 to scan a three dimensional volume of the body. The ultrasonic transducers in the array 14 transmit ultrasonic energy and receive echoes returned in response to this transmission. A transmit/receive ("T/R") switch 22 is coupled to the ultrasonic transducers in the array 14 to selectively couple echo signals from the transducer elements to A/D converters 30 during the receive phase of operation. The times at which the array 14 is activated to transmit signals may be synchronized to an internal system clock, or may be synchronized to a bodily function such as the heart cycle, for which a heart cycle waveform is provided by an electrocardiography (ECG) device 26. When the heartbeat is at the desired phase of its cycle as determined by the waveform provided by the ECG device 26, the ultrasonic probe 12 is commanded to acquire an ultrasonic image. In the conduct of the method of the present invention, a continuous sequence of real time image frames of a carotid artery is acquired as blood containing contrast agent begins to perfuse the vasculature of plaques in the carotid.

Echoes from the transmitted ultrasonic energy are received by the transducer elements of the array 14, which generate echo signals that are coupled through the T/R switch 22 and digitized by analog to digital ("A/D") converters 30 when the system uses a digital beamformer. Analog beamformers may alternatively be used. The A/D converters 30 sample the received echo signals at a sampling frequency

controlled by a signal f_s generated by a central controller 28. The desired sampling rate dictated by sampling theory is at least twice the highest frequency of the received passband, and might be on the order of 30-40 MHz. Sampling rates higher than the minimum requirement are also desirable. Control of the ultrasound system and the setting of various parameters for imaging, such as probe selection, are affected by user manipulation of the controls of the user interface of a control panel 20 which is coupled to and applies its control through the central controller 28.

The echo signal samples from the individual transducer elements of the array 14 are delayed and summed by a beamformer 32 to form digital coherent echo signals. For 3D imaging with a two dimensional array, it is preferable to partition the beamformer 32 between a microbeamformer located in the ultrasonic probe 12 and the main beamformer in the system mainframe as described in US Pat. 6,013,032 (Savord) and US Pat. 6,375,617 (Fraser). The digital coherent echo signals are then filtered by a digital filter 34. In this embodiment, the probe transmit frequency and the receiver frequency are individually controlled so that the beamformer 32 is free to receive a band of frequencies which is different from that of the transmitted band such as a harmonic frequency band for detection of harmonic contrast agents. The digital filter 34 bandpass filters the signals, and can also shift the frequency band to a lower or baseband frequency range. The digital filter 34 could be a filter of the type disclosed in U.S. Patent No. 5,833,613 (Averkiou et al.), for example. Filtered echo signals from scans of successive image frames are stored in a frame memory 42. Since it is important for the calculation of precise time intensity curves that pixels of

successive image frames be spatially aligned, registration of the successive frames is performed by an image stabilizer 44. This spatial correlation is preferably performed by use of an image stabilizer as described in US Pat. 6,589,176 (Jago et al.)

The spatially aligned image frames are coupled from the frame memory 42 to a B mode processor 36 for conventional B mode processing and the production of 2D B mode images. The image frames, and particularly their harmonic contrast agent signal content returned from microbubbles, are coupled to a contrast signal processor 38. The contrast signal processor 38 preferably separates echoes returned from harmonic contrast agents by the pulse inversion technique, in which echoes resulting from the transmission of multiple pulses to an image location are combined to cancel fundamental signal components and enhance harmonic components. A preferred pulse inversion technique is described in U.S. patent 6,186,950 (Averkiou et al.)

The filtered echo signals from the frame memory 42 are also coupled to a Doppler processor 40 for conventional Doppler processing to produce velocity and/or power Doppler images. The output signals from these three processors 36, 38, 40 may be scan converted and displayed as planar 2D images, for which their outputs are coupled to an image processor 50 for a display 52. Their output images, when 3D scanning is performed, may also be rendered as three dimensional (3D) images, which may also be processed for display on display 52.

After a sequence of image frames has been acquired during contrast agent delivery and stored in the frame memory 42, the user may review the images in the B mode, examples of which are shown in FIGURES 4a and 4b. These are images of carotid arteries containing plaque. The large bright areas 62 in the

images are regions of blood flow containing contrast agent, which return particularly strong (and hence brightly displayed) echo signals. The vessel wall 18 is distinctly shown in FIGURE 4a with its vasculature perfused with contrast. A discerning user can also spot plaques in the images. Unlike the lumen of the vessel, the microvasculature of plaques will contain much less contrast and hence appear as darker areas in the images. The user can trace or outline these plaques when they are spotted, and these outlined plaque areas are processed as described below. FIGURES 4a and 4b each contain a plaque 60 which the user has outlined using a control on the control panel 20 such as a trackball or mouse.

The identification of the plaque outline area 60 is coupled to a T-I curve calculator 46 as shown in FIGURE 2. The T-I curve calculator then processes the pixels of the plaques in the sequence of image frames to form a time intensity curve for each point in the plaque. When contrast agent is flowing at a particular point in the plaque during contrast delivery, the contrast agent will build up following its initial arrival time as shown in FIGURES 4b and 5b, which correspond to points in FIGURES 4a and 5a, respectively. The T-I curve calculator processes this build-up in contrast signal intensity to produce a time intensity curve as described in US pat. pub. no. US2012/0253190 (Gauthier et al.) and US Pat. 8,460,194 (Averkiou et al.) An idealized time intensity curve 60 is shown in FIGURE 3. It is seen that this curve begins to increase following the initial arrival of contrast agent at time t0, builds up to a maximum amplitude A at the time of maximum contrast perfusion, then gradually declines as the contrast agent flows out of that region of the body.

A comparator 48 performs several checks on the time intensity curve data to verify that contrast

agent is indeed present at each point for which a time intensity curve has been produced. (If there is no flow of contrast at a point, there will be no time intensity curve for that point.) One check is to compare the amplitude of the time intensity curve against a noise threshold. Amplitude spikes from artifacts in the image data are thereby eliminated from consideration as contrast. Another test is to compare the maximal amplitude region of the curve 60 against a contrast threshold. This threshold is a level which a contrast agent response should exceed for a sustained period of time. When the time intensity curve from a point in the plaque region passes both of these tests, it is confirmed that a flow of contrast agent was present at the point.

A qualitative image of perfusion may now be formed for the plaque region. The maximum intensity amplitudes A or the mean signal intensity of the time intensity curves at the points where contrast was present may be mapped to corresponding colors of a color map, and the color map may be displayed as a parametric overlay over a B mode image of the plaque region as described in US Pat. 6,692,438 (Skyba et al.) For instance, region of contrast perfusion may be displayed in varying shades of red and areas with no perfusion may be displayed as black. The user can thus observe the degree of perfusion of the plaque, the degree to which it contains vascularization. FIGURE 7 illustrates four regions of plaque 70 with varying degrees of perfusion, each shown against a black background. Within each plaque region, points which are perfused are shown in white and points with no perfusion are shown in black. In FIGURE 7a the plaque area 70 is 100% perfused. In FIGURE 7b the plaque area 70 is 76% perfused. In FIGURE 7c the plaque area 70 is 38% perfused and in FIGURE 7d the plaque area 70 is only 26% perfused.

In accordance with a further aspect of the present invention, the overall perfusion of a plaque is quantified by a perfusion quantifier 54. The overall number of pixels in a plaque area 70 that have perfusion are divided by the total number of pixels in the image of the plaque. A binary grading system is then applied to this result. Zero represents less than 50% of a carotid plaque area 70 contained moving microbubbles and 1 represents more than 50% of the carotid plaque area contained moving microbubbles. To enhance the reliability of these results, the perfusion quantifier receives the Doppler flow map of the plaque. Each point where a valid time intensity curve of contrast was found should also be found to exhibit motion at the corresponding point in the Doppler flow map, since the contrast agent must be flowing at the point. The presence of Doppler-identified motion at a point where contrast and a time intensity curve were found confirms the point as having contrast present. A highly reliable quantification of perfusion is thereby produced and displayed on the display 52. It has been found that the mean contrast agent intensity signal from a plaque is significantly higher for asymptomatic patients (patients with no history of plaque particulate breakup) than symptomatic patients, patients with a history of plaque particulates in the blood flow.

FIGURE 6 is a flowchart of a method of the present invention. In step 100 an image sequence of a carotid artery is acquired, typically lasting at least a minute following infusion of contrast. This captures images of any plaque microflow containing the contrast agent. In step 102 frame-to-frame motion is compensated using motion compensation techniques so that the plaque is in registration with the same pixels over the image sequence. In step 104

the plaque region is delineated in the images as by tracing. In step 106 a time-intensity curve is formed for each pixel in the plaque region. The contrast arrival time may be estimated based on a given increase intensity above the noise level. In step 108 the intensity values at each point where contrast is present is compared before and after contrast arrival and, if there is a significant difference, the pixel is identified as having perfusion. This identification of perfusion is done for every pixel or group of pixels (step 110). In step 112 the percentage of the total pixels in the plaque exhibiting perfusion is quantified. This is done by dividing the overall number of pixels that have perfusion by the total number of pixels in the image of the plaque. In step 114 a qualitative result is presented by forming an anatomical map of the percentage of the plaque that is perfused as shown in FIGURE 7.

WHAT IS CLAIMED IS:

1. An ultrasonic diagnostic imaging system for the evaluation of plaque by contrast enhanced ultrasound comprising:

an ultrasound imaging probe having an array transducer which acquires a sequence of ultrasound images of a plaque during contrast agent delivery;

a time intensity curve calculator which forms a time intensity curve for each point in a plaque image where contrast is present;

a comparator which identifies pixels in the plaque image where perfusion is present; and

a display which displays the degree of perfusion in the plaque.

2. The ultrasonic diagnostic imaging system of Claim 1, further comprising an image processor which produces an anatomical map of the plaque showing where perfusion is present.

3. The ultrasonic diagnostic imaging system of Claim 1, further comprising a perfusion quantifier which quantifies the percentage of pixels in the plaque image exhibiting perfusion.

4. The ultrasonic diagnostic imaging system of Claim 1, further comprising a frame memory which stores the acquired sequence of ultrasound images.

5. The ultrasonic diagnostic imaging system of Claim 4, further comprising an image stabilizer, responsive to images stored in the frame memory, which compensates for frame-to-frame motion.

6. The ultrasonic diagnostic imaging system of Claim 1, further comprising a plaque tracer which

outlines a plaque in a carotid image.

7. The ultrasonic diagnostic imaging system of Claim 6, wherein the plaque tracer further comprises a user control of an ultrasound system control panel.

8. The ultrasonic diagnostic imaging system of Claim , wherein the comparator is further operable to compare pixel intensity values before and after contrast arrival in the plaque.

9. A method of evaluating plaque with contrast enhanced ultrasound comprising:

acquiring a sequence of ultrasound images during contrast agent delivery of a carotid artery having plaque;

identifying a plaque in an ultrasound image;

comparing intensity values at locations in the plaque before and after the arrival of contrast;

identifying points in the image having perfusion; and

displaying the degree of perfusion in the plaque.

10. The method of Claim 9, wherein identifying a plaque further comprises outlining a plaque in one of the ultrasound images.

11. The method of Claim 10, further comprising forming a time intensity curve at each point in the plaque where contrast is present.

12. The method of Claim 9, further comprising forming an anatomical map of the plaque which shows points where perfusion has been identified.

13. The method of Claim 9, further comprising

quantifying the percentage of points in an image of the plaque which exhibit perfusion.

14. The method of Claim 9, further comprising compensating for frame-to-frame motion in the sequence of ultrasound images.

15. The method of Claim 9, further comprising correlating points in the image of the plaque where perfusion has been identified with points in the image of the plaque where motion is present.

EVALUATION OF CAROTID PLAQUE USING CONTRAST ENHANCED ULTRASONIC IMAGING

Abstract of the disclosure:

An ultrasound system and method are described for acquiring a sequence of ultrasound images of the carotid artery during the delivery of a contrast agent. Plaque in the images is identified and a time-intensity curve is calculated for pixels in the images. The intensity values before and after the arrival of contrast are compared to identify pixels or groups of pixels having perfusion. An anatomical image may be formed showing areas in an image of the plaque where perfusion is present, or the perfusion may be quantified by determining the percentage of pixels in the plaque image which exhibit perfusion. The degree of perfusion is an indicator of the risk of plaque particulates in the blood stream which may lead to stroke

2014 PF 01656

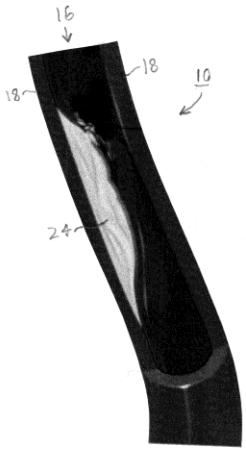

Fig. 1

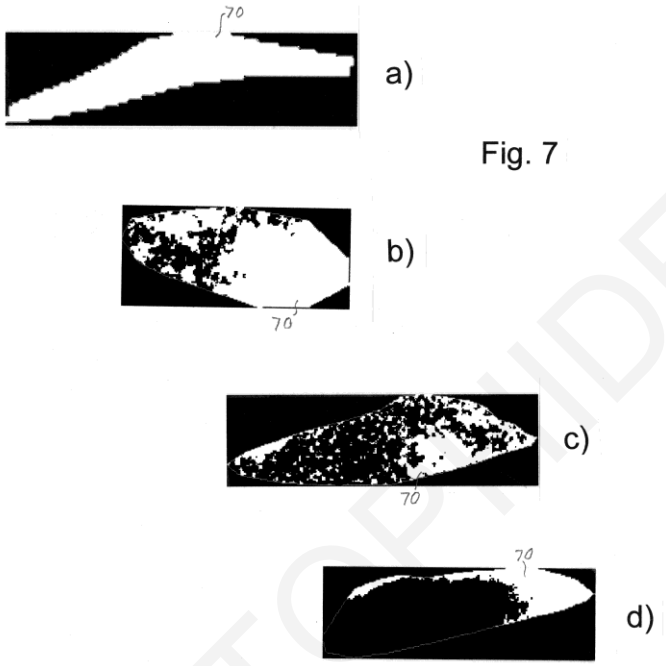

Fig. 7

2014 PF 01656

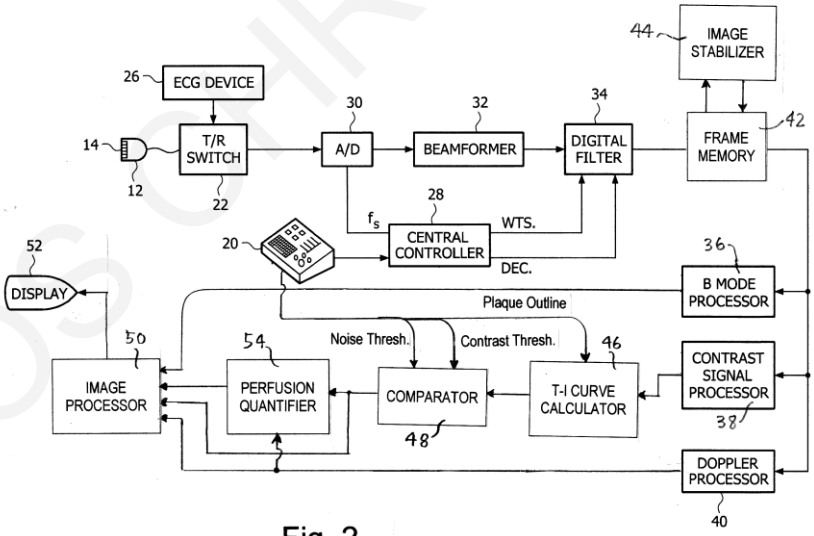

Fig. 2

2014 PF 01656

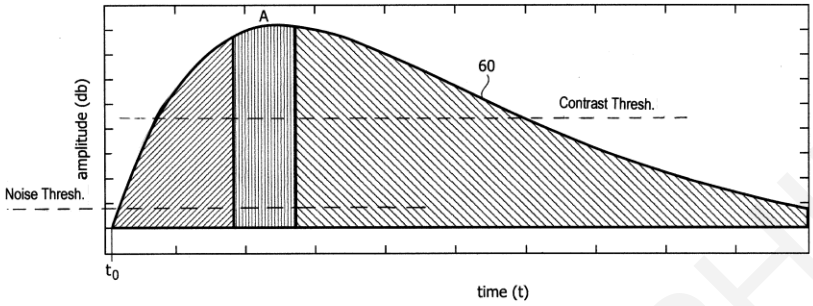

Fig. 3

2014 PF 01656

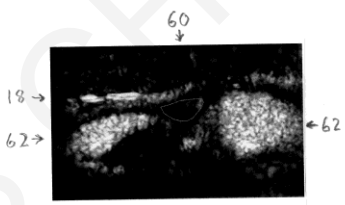

Fig. 4a

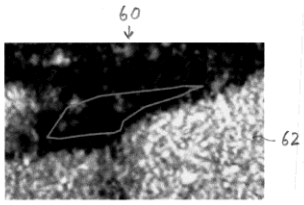

Fig. 5a

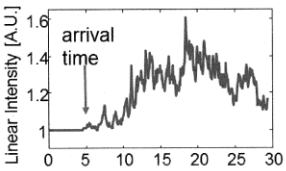

Fig. 4b

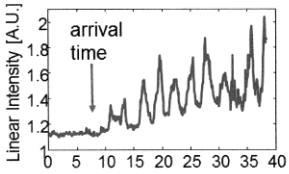

Fig. 5b

2014PF01656

Fig. 6